Magnet Architectures and Active Radiation Shielding Study (MAARSS)

Final Report for NASA Innovative Advanced Concepts Phase II

Shayne Westover – PI – NASA JSC, Houston, TX.
Rainer Meinke – Advanced Magnet Lab, Inc
Shaun Nerolich – Capstone Solutions Group LLC
Scott Washburn – University of Colorado, Boulder, CO.
Roberto Battiston – INFN, University of Trento, Italy
William Burger – INFN, University of Perugia, Italy
Dallas Kasaboski – International Space University, Illkirch-Graffenstaden, France
Francis Davies – NASA JSC, Houston, TX.

November 2014

NASA STI Program ... in Profile

Since its founding, NASA has been dedicated to the advancement of aeronautics and space science. The NASA scientific and technical information (STI) program plays a key part in helping NASA maintain this important role.

The NASA STI program operates under the auspices of the Agency Chief Information Officer. It collects, organizes, provides for archiving, and disseminates NASA's STI. The NASA STI program provides access to the NASA Aeronautics and Space Database and its public interface, the NASA Technical Report Server, thus providing one of the largest collections of aeronautical and space science STI in the world. Results are published in both non-NASA channels and by NASA in the NASA STI Report Series, which includes the following report types:

- TECHNICAL PUBLICATION. Reports of completed research or a major significant phase of research that present the results of NASA Programs and include extensive data or theoretical analysis. Includes compilations of significant scientific and technical data and information deemed to be of continuing reference value. NASA counterpart of peer-reviewed formal professional papers but has less stringent limitations on manuscript length and extent of graphic presentations.

- TECHNICAL MEMORANDUM. Scientific and technical findings that are preliminary or of specialized interest, e.g., quick release reports, working papers, and bibliographies that contain minimal annotation. Does not contain extensive analysis.

- CONTRACTOR REPORT. Scientific and technical findings by NASA-sponsored contractors and grantees.

- CONFERENCE PUBLICATION. Collected papers from scientific and technical conferences, symposia, seminars, or other meetings sponsored or co-sponsored by NASA.

- SPECIAL PUBLICATION. Scientific, technical, or historical information from NASA programs, projects, and missions, often concerned with subjects having substantial public interest.

- TECHNICAL TRANSLATION. English-language translations of foreign scientific and technical material pertinent to NASA's mission.

Specialized services also include creating custom thesauri, building customized databases, and organizing and publishing research results.

For more information about the NASA STI program, see the following:

- Access the NASA STI program home page at *http://www.sti.nasa.gov*

- E-mail your question via the Internet to help@sti.nasa.gov

- Fax your question to the NASA STI Help Desk at 443-757-5803

- Phone the NASA STI Help Desk at 443-757-5802

- Write to:
  NASA Center for AeroSpace Information
  7115 Standard Drive
  Hanover, MD 21076-1320

Preface

This report was built from multiple papers and documents. To keep the size of the main report at a manageable level, Francis Davies of the Johnson Space Center extrapolated detailed summaries of the larger documents, and included each complete larger document as an appendix. The table below lists the authors of each document that was used to create each section of this Phase II report.

This report is follow-on work to the Phase I report (NASA/TP-2014-217390). The Phase II report was performed under NASA Broad Agency Announcement NNH12ZUA004N.

List of Authors and Sections

Section	Title	Author/Source	Appendix
Preface	Preface	Francis Davies	
	Abstract	Francis Davies	
	Executive Summary	Rainer Meinke	
1	Introduction	Francis Davies	
2	Forces on the Solenoid Array – Analysis of Forces Using CoilCAD® Toolbox	AML	
3	Structural Design	Shayne Westover et al. (see Appendix A)	A
4	Compensator Coil Optimization	AML	
5	Forces on Incoming Space Capsules	AML	
6	Interplanetary Magnetic Field	AML	
7	Shielding Coil Gap Analysis	AML	
8	Increasing Radiation Shielding Efficiency – Scaling of Integrated Field Strength	AML	
9	Quench Detection and Protection	AML	B
10	Expandable Coil Testing at AML	AML	
11	HTS Coil Thermal Structural Analysis	AML & Shaun Nerolich	C
12	Spacecraft and Mission Architecture	Dallas Kasaboski	
13	Simulation Results for the Extendable Solenoid Shield (Solenoid Array) Configuration	William Burger	D
14	Thermal Design Concept	Dallas Kasaboski	
15	Trade Studies: System Analysis and Technology Work	Dallas Kasaboski	E
16	Conclusion	Francis Davies	

Table of Contents

FIGURES

Tables

Appendices

Acronyms, Abbreviations, & Nomenclature

1-T	one tesla
A	Ampere
AC	alternating current
AML	Advanced Magnet Lab, Inc.
atm	atmosphere
BdL	Magnetic field times the change in length
BFO	blood-forming organ
BL	bending power
BOL	beginning of life
cm	centimeter
cm_2	square centimeter
cm_3	cubic centimeter
cSv/rem	centisievert / roentgen equivalent man
ESOI	Earth-Sun Orbital Injection
EVA	extravehicular activity
FDM	Finite Difference Method
FEA	Finite Element Analysis
FEM	Finite Element Method
g/cm	grams per centimeter
GCR	galactic cosmic ray
GEANT	GEometry ANd Tracking
H_2	Diatomic Hydrogen
He	Helium
HEO	high-Earth orbit
hr	hour
HSF	high-strength fiber
HTS	high-temperature superconductor
HZETRN	High Charge and Energy Transport
IAASS	International Association for the Advancement of Space Safety
lbm/in^3.	pounds-mass per cubic inch
IMF	Interplanetary Magnetic Field
in.	inch
ISS	International Space Station
JWST	James Webb Space Telescope
K	Kelvin

kA	kilo ampere
kg	kilogram
kJ	kilojoule
km	kilometer
km/s	kilometer per second
kV	kiloVolt
kW	kiloWatt
I_{sp}	specific Impulse
lb	pound
lbm	pound mass
LEO	low-Earth orbit
LH2	Liquid Hydrogen
LN2	Liquid Nitrogen
LOX	Liquid Oxygen
LTS	low-temperature superconductor
m	meter
MAARSS	Magnet Architectures and Active Radiation Shielding Study
MATLAB	Software package for scientific calculations
MER	Mars Exploration Rover
MeV	Mega electron volt
MJ	megajoule
mm	millimeter
MN	meganewton
MPa	megapascal
MPFL	mechanically pumped fluid loop
MPZ	minimum propagation zone
MQE	minimum quench energy
MRI	Magnetic Resonance Imaging
m/s	meters per second
mSv	millisievert
mt	Metric Tonne
mT	millitesla
MW	megawatt
N	Newton
NASA	National Aeronautics and Space Administration
Nb_3Sn	niobium-tin
NbTi	niobium-titanium
NEA	near-Earth asteroid
NIAC	NASA Innovative Advanced Concepts
nT	nanotesla
NZPV	normal zone propagation velocity
O_2	Diatomic Oxygen
Ohm	a unit used for measuring electrical resistance

psia	pounds per square inch absolute
ReBCO	rare-earth barium copper oxide
SC	superconducting
SEP	solar energetic particle
SLS	Space Launch System
SPE	Solar Proton Event
T	tesla
T·m	tesla meter
TRL	Technology Readiness Level
UV	ultra-violet
W	Watt
W/m2	Watts per square meter
YBCO	yttrium-barium-copper-oxide

Abstract

This report describes the analysis of several magnetic radiation shield architectures and the spacecraft systems associated with them, such as quench detection, thermal management, and compensation coils. This work was performed as part of the NASA Institute of Advanced Concepts (NIAC) Grant Phase II effort.

Because radiation exposure during long duration space missions poses a significant risk for crewed space-flight, Advanced Magnetic Lab, Inc. **(AML) and NASA are studying magnetic radiation shielding, which may generate low-mass protection. Recent technological developments in high-temperature superconducting technology suggest the possibility of such shielding. This report analyzes some of the technical difficulties involved in such a system and identifies technology areas where further investment would be warranted.**

Most analysis was performed on a baseline configuration (8-meter diameter coils, with 1 tesla field). However, a baseline design with an expandable coil configuration (16 meter diameter coils, 1.5 tesla field) has a significant potential to increase shielding efficiency.

The magnetic forces on the magnetic shield's components are large enough to require detailed structural design. Analysis of the thermal structural response of a yttrium-barium-copper-oxide (YBCO) high-temperature, superconducting (HTS) tape in a large-scale solenoid magnet showed that structural and thermal performance improved by replacing Hastelloy® with graphene in the tape. Integrating graphene into the high-strength fiber (HSF) support structure brings even greater benefits.

The energy stored in a shield system's magnetic field must be safely dissipated if a quench-type failure occurs. Analysis of quench detection by fiber-optic thermal sensing and improvement of quench characteristics using graphene showed quench is manageable. Low-temperature superconductors can quench when subjected to movement, but lab tests of coil expansion testing showed that HTS materials do not quench when subject to the movement associated with coil expansion.

Compensation coils are necessary to reduce the magnetic field in the crew habitat. Analysis showed that subdividing the compensation coil into individually controlled sections allows for a robust, adjustable system.

AML analyzed the forces on an approaching capsule that were a result of eddy currents in its structure induced by its motion through the magnetic field from the coils. AML also analyzed coil-to-coil forces.

Thermal control to maintain the HTS material at a suitable temperature is challenging. The sunshield technology review revealed a greater possibility of thermal insulation of the coils and use of passive cooling. The availability of suitable cryocoolers was also reviewed.

A parametric graph estimating mass and shielding effectiveness for strength and thickness was developed, and allows spacecraft designers to assess the tradeoffs of using a magnetic radiation shield.

Executive Summary

The radiation level in space due to solar particle events (SPE) and galactic cosmic rays (GCR) constitutes a major hurdle for humans to explore the solar system. While human missions to the moon take a few days, missions to near-Earth asteroids or Mars will take many months to a year. To guarantee that astronauts consume no more than their maximum-allowed radiation-exposure dose per year, substantial radiation shielding surrounding the habitat of a spaceship is required. Over time, several techniques for radiation shielding have been proposed and investigated, which include passive shielding, active shielding based on electromagnetic fields, and extended plasma surrounding a spaceship. Detailed information on radiation-related issues are discussed in various publications and NASA reports.[1]

Because of the geomagnetic field, little or no radiation shielding is needed on Earth or in low-Earth orbit (LEO). Based on the same principle, in 1969, Wernher von Braun proposed active magnetic shielding to deflect incoming ionizing particles and protect astronauts during extended missions.[2] However, the difficulty of generating and maintaining large volumes of high-magnetic flux densities constituted an almost insurmountable technical hurdle. Large high-field, normal conducting magnets would be extremely heavy, and even more importantly, would require large amounts of electrical energy. Superconducting magnets can operate in a persistent mode, eliminating the need for vast amounts of continuous electrical power. Technical hurdles remain, because magnets based on low-temperature superconductors (LTS) (i.e., niobium-titanium (NbTi) and niobium-tin (Nb_3Sn)) require that the conductors be kept at low, near liquid helium (4.2 K) temperature in absolute rigid assemblies. Even superconductor movements on the order of microns under the effect of acting Lorentz forces generate enough energy to heat the conductor locally above its critical temperature, at which the state of superconductivity is "lost." As a result of this and the required mechanical support structures, existing large, high-field magnets for applications such as charged particle accelerators, magnetic resonance imaging, and fusion research are extremely heavy. Based on the design concept of such LTS magnets, it was again inconceivable that magnetic shielding could be used for radiation shielding in space.

However, the discovery of high-temperature superconductors (HTS) has led to a potential paradigm shift in magnet technology. HTSs enable magnet operation up to the temperature of liquid nitrogen (77 K), where the enthalpy of all materials is orders of magnitude larger than at the operational temperatures needed for LTS magnets. Because of the large increase in enthalpy at elevated operational temperatures, the HTS coils' minimum quench energy (MQE) is increased by orders of magnitude, and mechanical movements of the conductors do not generate enough heat to quench the coil (i.e., initiating an irreversible transition into the normal conducting state).

Because of the relatively large MQE of HTSs, the support structures needed to avoid any conductor movement in such coils can be significantly lighter than the structure needed for corresponding LTS magnets. The only requirement for needed support structures is containment of the magnetic pressure acting in the coils. Accordingly, with HTS, ultra-lightweight coils become feasible, and magnets with flux densities ranging from one to several tesla and volumes of hundreds to several thousand m^3 can be considered for space applications.

Based on the paradigm shift in magnet technology enabled by HTSs, the Advanced Magnet Lab, Inc. (AML) proposed the concept of expandable superconducting (SC) coils.[3,4] Similar in shape to airships, like the original Zeppelin or modern blimps, these superconducting coils would "expand" under the influence of the magnetic pressure in coils with high-flux density. When large transport currents in the order of tens of kiloamperes are flowing through these embedded coils, magnetic fields in the range of 1 to several tesla are generated and magnetic pressures in the range of multiple atmospheres result.[5] Unlike a gas-filled balloon, the blanket with the embedded superconductor does not need to be gas-tight, because it is magnetic pressure acting on the current-carrying conductors instead of gaseous pressure that expands the coil.

1 Introduction

Getting to interesting destinations in our solar system, such as Mars or the asteroids, means trip durations long enough that exposure of the crew to radiation is an issue.

One way to reduce radiation exposure is to shield the crew from the radiation. Conventional terrestrial radiation shields involve thick layers of material. This is too heavy to be practical in space. It is possible to take advantage of the charged nature of the radiation particles by using magnetic fields to bend the paths of the radiation particles away from the habitable volume of the space craft.

This report analyses the various technical issues associated with an example design of such a system.

2 Forces on the Solenoid Array – Analysis of Forces Using CoilCAD® Toolbox

The magnetic forces on the components of the magnetic shield are significant enough to require structure designed for such forces. The coil configuration considered here resulted from the Phase I study.

The CoilCAD® toolbox was used to design and optimize the solenoid array. The generated space curves of the solenoid array's winding configurations can be used to calculate magnetic field strengths, as well as inductances, mutual inductances, Lorentz forces, and torque. The CoilCAD® toolbox does not use Finite Element Analysis (FEA) to perform such calculations. The integral approach of the CoilCAD® toolbox is much faster than FEA calculations and complex optimizations of winding patterns become feasible on personal computers using this approach. For the study of forces on the space array, this is an essential feature, because this approach not only provides the overall forces on the array, it also allows local forces to be determined on individual segments of the conductor accurately, even in the presence of adjacent solenoids in contact. Conventional FEA techniques cannot address problems with such large variation in element sizes required to describe the winding configuration and the full problem domain. The existing CoilCAD® toolbox was improved and dedicated tools were written for speeding up and analyzing forces on the solenoid array. Some existing field and force calculations tools were modified to Monte-Carlo calculations to provide faster estimate of forces. The codes were successfully tested against commercially available FEA codes like COMSOL (a commercial multi-physics modelling application) for simplified problems.

2.1 Procedure to Analyze Forces on the Solenoid Array

As a first step, forces at the center of an isolated solenoid were calculated and compared with the analytically expected pressure of 4 atmosphere (atm) for an ideal infinitely long solenoid of 1 T field. Along with independent verification with COMSOL code, this step verifies the new CoilCAD® tools. Actual force calculations for the shielding array were then performed. But because of the close proximity of the solenoids, correct simulation near the contact region requires optimization of the coil element sizes. The element sizes were successively adjusted until the forces near the contact region no longer depended on the element size. The obtained total force on the array and individual solenoids were again verified against COMSOL simulation using a simplified model. Studies show using 5760 uniformly distributed points-per-turn were sufficient to achieve convergence in force computations. A data set with a complete list of forces on the array was provided to the team performing structural analysis of the solenoids. Forces on distorted coils were then calculated using the same CoilCAD® code. This procedure only

approximately simulates the real scenario where both the forces and the structure are undergoing changes simultaneously. Sections 2.2 and 2.3 summarize the results of the forces calculated for an individual solenoid and for a solenoid with distortions computed from the structural analysis.

2.2 Forces on Solenoid Array without Deformations

Figure 2.1 shows the forces acting on the solenoids on a plane passing through the center of the array. Figure 2.2 shows the force distribution on one of the solenoids. While the forces at the center are only radial, the forces at the ends of the solenoid are dominated by the axial forces. There is also a small azimuthal component of the force at the ends because of the finite pitch of the coil winding. Resulting radial force with compensation is ~10[MN] on each solenoid.

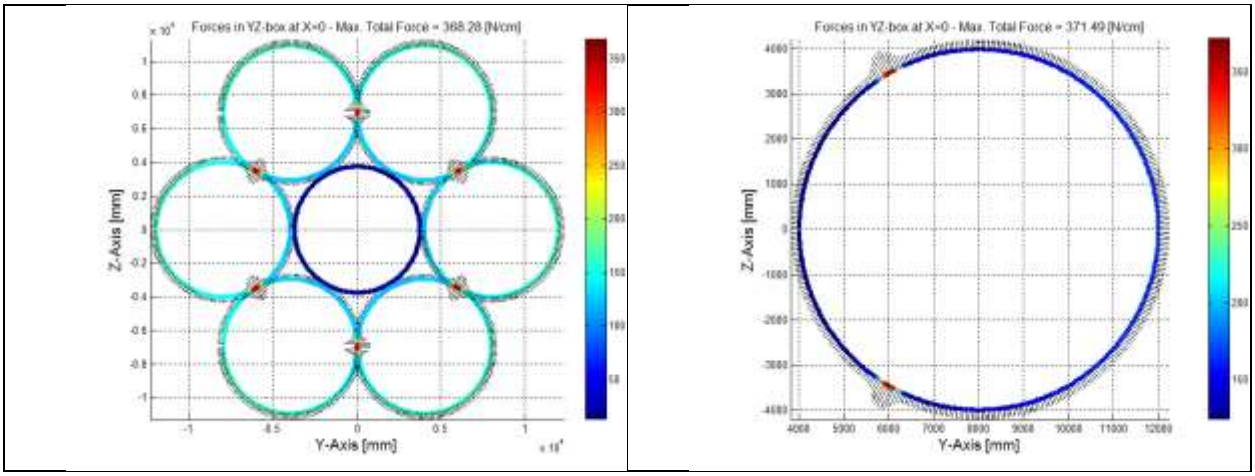

Figure 2.1. Forces at the center of solenoid array without deformations.
Left plot shows the full array. Right plot shows the zoomed view for one solenoid.

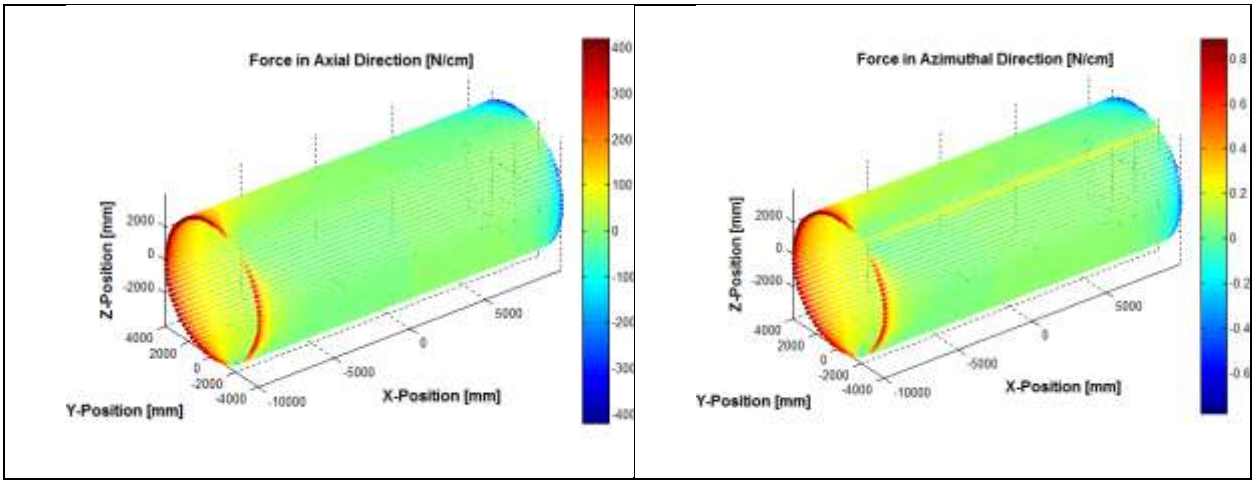

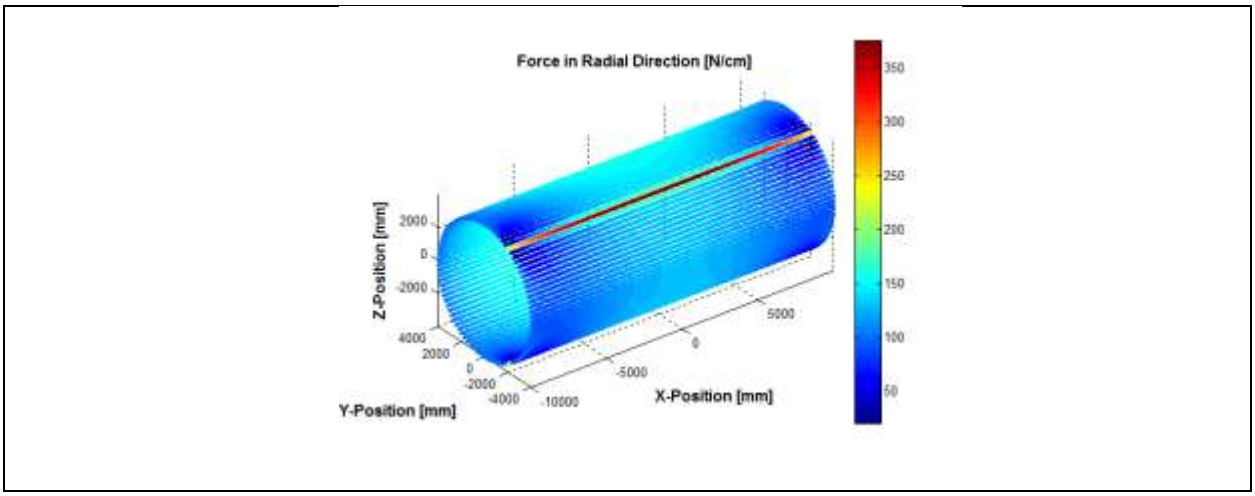

Figure 2.2. Force distribution on an individual solenoid.
Top left figure shows forces in axial direction, top right show forces in azimuthal direction, and bottom figure shows forces in radial direction.

2.3 Forces on an Individual Solenoid with Deformations

The cross sectional shape of the expandable solenoid coils has limited stiffness and will be distorted because of the Lorentz forces acting on the coil array configuration surrounding the spaceship habitat. The resulting shape changes will affect the field inside the coils, the field in the habitat, and the Lorentz forces acting between neighboring coils. The structural engineering team investigated how the magnitude of the shape change and displacement at individual segments on the coil affected the overall magnetic field (Figure 2.3). The displacements show no significant effect on the magnetic flux density inside the solenoids (Figure 2.4).

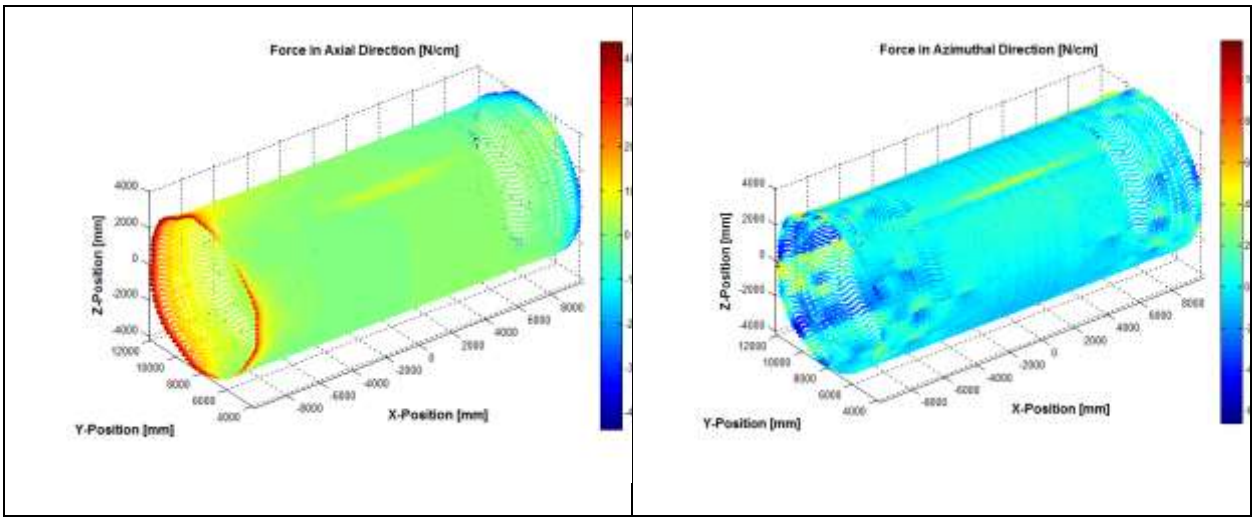

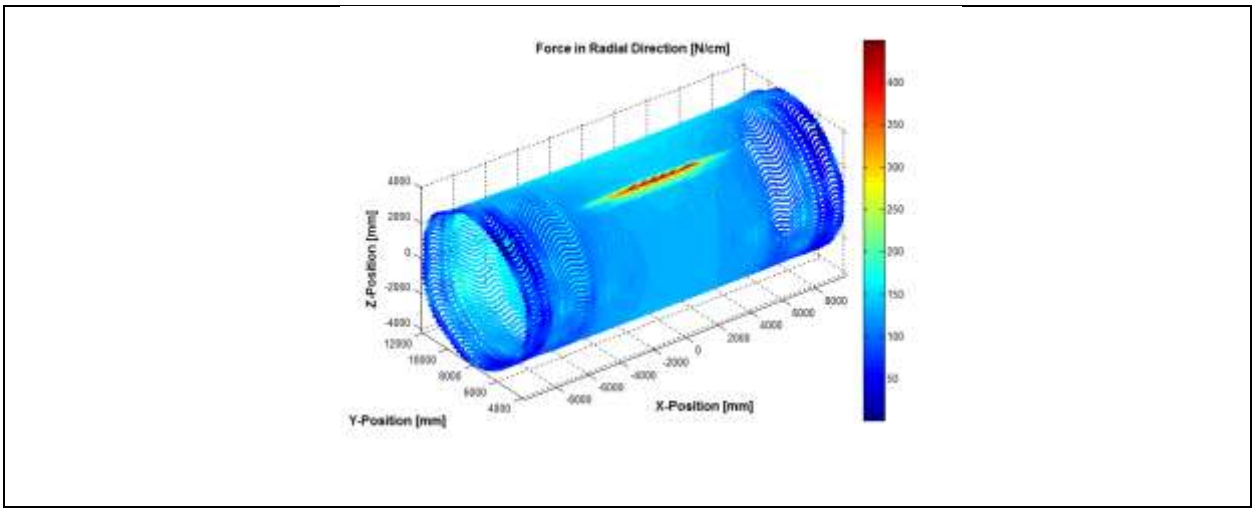

Figure 2.3. Force distribution on deformed solenoid.
Top left figure shows forces in axial direction, top right figure shows forces in azimuthal direction, and bottom figure shows forces in radial direction.

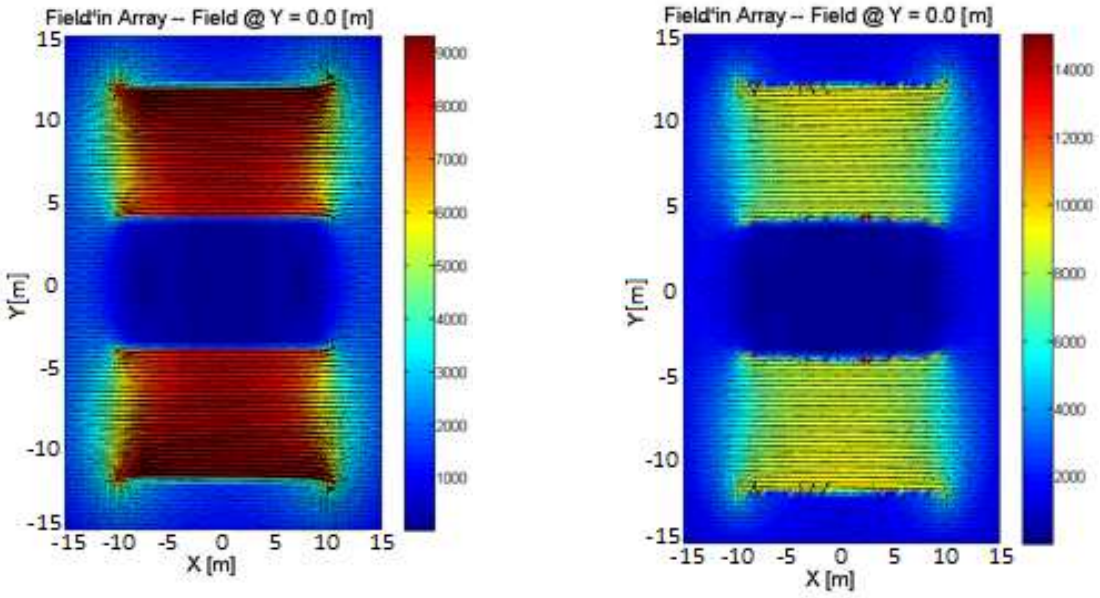

Figure 2.4. Comparison of magnetic field inside for the undistorted and distorted solenoids.
Left plot shows the field for the undistorted solenoid. Right plot shows the field for the distorted solenoid.

3 Structural Design

See Appendix A for the complete analysis.

3.1 Strongback

The strongback is the primary support member for the solenoid coil. Two models were constructed using composite (fiber, matrix) methods: one solid, and the other hollow with lightening holes and 2-in.-(50.8 mm) thick structure. Both models are comprised of carbon fiber and epoxy resin with a mass density of 0.059 lbm/in.^{3} (1.64 g/cm^3). The solid model was simulated first to demonstrate the validity of the single and multi-coil configurations regarding strength. The hollow model is an improvement based on the solid model to achieve weight reduction.

The governing geometric constraint to determine the profile of the strongback cross-section is sizing the splines and central support structure such that the circumference of the solenoid coil is equal to the perimeter of the strongback cross-section. The profile must enable the membrane/fabric cylinder that supports the conductor to drape between the splines, prevent kinking of the conductor, and enable interlocking of several strongbacks for packaging (Figure 3.1). This work shows that there is enough strength and flexibility to make the concept viable. Continued research is required in the enabling technologies for increased strength-to-weight ratio design, materials, and construction techniques.

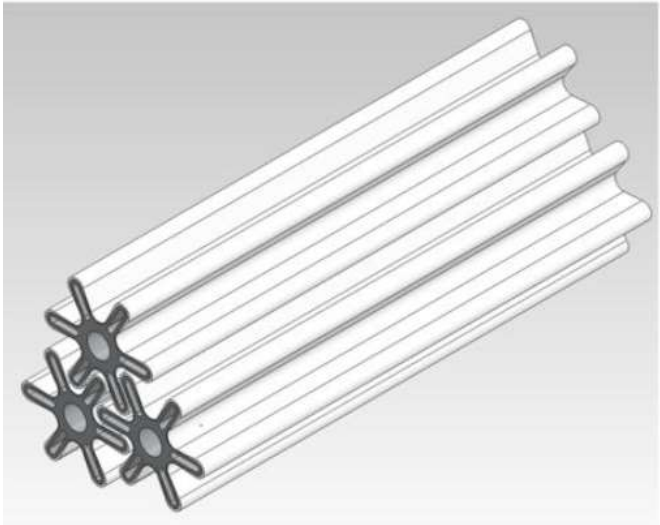

Figure 3.1. Illustration of interlocking concept.

Susceptibility to ultra-violet (UV) radiation was a dominant selection criterion for materials chosen for final design and analysis. High-strength organic fibers initially presented a preferred solution, but susceptibility to UV radiation prevented such fibers from being considered for design. The final design uses inorganic carbon fibers because of their UV resistance and high strength, but these fibers may not be sufficiently flexible. Continued research is needed to determine whether metalized coatings or other protection mechanisms could protect organic fibers sufficiently to allow their use.

As currently analyzed, the strongback weighs 64,000 lbs (29,000 kg); the solenoid and limiters, excluding the conductor, weigh 6,034 lbs (2,737 kg); and the spars, battens, and tow bolstering weigh 1,412 lbs (640 kg). The design is not optimized because mass dispersion (i.e., correlating material

thickness with level of stress or strain within the structure) has not been considered. Current results indicate high safety factors for the strongback as shown in Table 3.1. As such, it is not unreasonable to expect a weight reduction with the use of such optimization techniques as mass dispersion. Given the current calculated safety factors, coupled with design optimization, it is estimated that the weight could be reduced by ~10X. With this reduction, the total weight estimated for the strongback and solenoid coil structures is 7,145 lbm (3,240 kg).

Table 3.1. Coil-Alone Configuration

Coil-Alone Configuration						
Component	System	Manufacurer / Component / Name		Tensile Strength (ksi)	Maximum Principal Stress (ksi)	Safety Factor
*Cylinder / Limiter	Fiber Bolster	TorayCA / Fiber / T1000G	**TorayCA / Matrix / #2500	440	168	2.6
	Cylinder				120	3.7
	Cylinder Cuff				116	3.8
	Limiter				168	2.6
Hollow Strongback	Hub1	TorayCA / Fiber / M55J	HexPly 954-6	314	28	11.2
	Hub2				18	17.4
	Stiffener				26	12.1
	Spline Tip				22	14.3
	Spline Flank				23	13.7
	Spline Shallow Fillet				24	13.1
	Spline Deep Fillet				35	9.0

*FEM with the Limiter bolster

**Recommend HexPly 954-6 but no data available for this resin with T1000G fiber

3.2 Coil Assemblies

In the multi-coil configuration, there are six coil assemblies arranged in a circular array. In this configuration, each cylinder contacts two other cylinders and the six coil assemblies are yoked to the core. Such a large, interactive system is difficult to model completely, particularly under fluctuating Lorentz forces during deployment. Additionally, the cylinder and limiter are flexible structures that undergo large displacements, which introduce nonlinear effects. Because of these complications, a two-configuration design validation strategy was adopted: the coil-alone configuration and the multi-coil configuration. In the coil-alone configuration, the components that constitute the coil assembly were analyzed. In the multi-coil configuration, yoke assemblies were incorporated at fore and aft cylinder locations that bind the six coil assemblies together. Loads for all analyses are processed electromagnetic-field pressures resulting in appropriate loads corollaries within the structures domain.

Because of the complexity associated with analyzing the inflation event, it is recommended to develop a multi-physics solution architecture based on high-fidelity contact models incorporating all structures and governing system equations. Such an analysis would provide a clearer picture of how key components respond kinematically and structurally to the electromagnetic field pressures both in the time and frequency domains.

All the orthotropic shell laminates are predicated on average properties obtained via composite macroanalyses. This technique, once codified in Mathcad worksheets, permitted the rapid implementation of different layup combinations, thereby facilitating convergence to the present design. However, the resultant orthotropic properties do not include values for the transverse shear moduli. Because the FEA shell elements are a Mindlin shell formulation, which takes transverse shear into account, the transverse shear moduli must exist.[7] Therefore, they have been set as low as possible, yet still permit a solution. In the worst case, the largest transverse shear modulus is 1/10 of the in-plane shear modulus.

As with the high-fidelity contact model, a high-fidelity material model is required to obtain more accurate strains, stresses, and deformations. A solid model is especially essential to model the interface between the limiter and strongback. Currently, the limiters are attached to the row of nodes along the crown of each strongback spline. This places enormous transverse loads on these elements. In practice, the crown would be thickened and a mechanical means of fastening would be implemented to mitigate inter-laminar loads.

Cylinder and limiter recommendations are listed below:

1. Construction Methodology: 3DL technology, laminated tows
2. Materials:
    a. Fiber: TorayCA T1000G
    b. Matrix: HexPly 954-6 cyanate epoxy resin
    c. Film: 160 mils (4.064 mm) Dupont Kapton E film
3. Structural:
    a. Tows:
        i. Global: ¼ in. (6.35 mm) diameter @ ±45^{o}
        ii. Local Bolster: ½ in. (12.7 mm) diameter
    b. Spars:
        i. 2 in. x 1/2 in. (50.8 mm x 12.7 mm) tube
        ii. Mechanical joint to interface with the strongback
        iii. Inserted into pockets sewn into cylinder
    c. Battens:
        i. 1 in. (25.4 mm) diameter rod.
        ii. Inserted into pockets sewn in cylinder

Strongback recommendations:

1. Materials:
    a. Fiber: TorayCA M55J.
    b. Matrix: HexPly 954-6 cyanate epoxy resin
2. Structural:
    a. Fiber: 0^{o} / 90^{o}
    b. 2 in. (50.8 mm) thick.
    c. Mechanical joint to interface with limiter

Figures 3.2 and 3.3correlate with the table of safety factors.

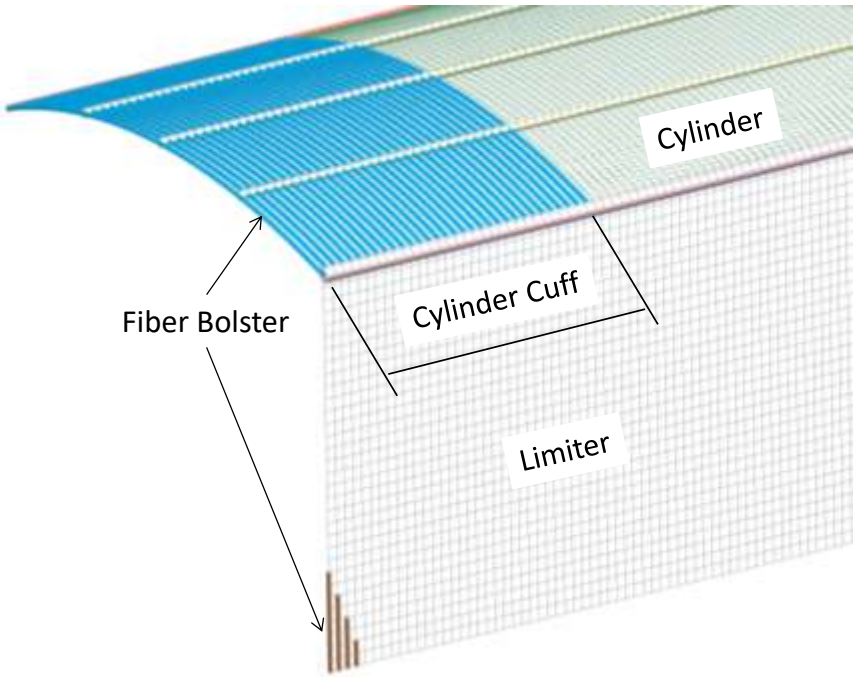

Figure 3.2. Cylinder/limiter components: safety factors table.

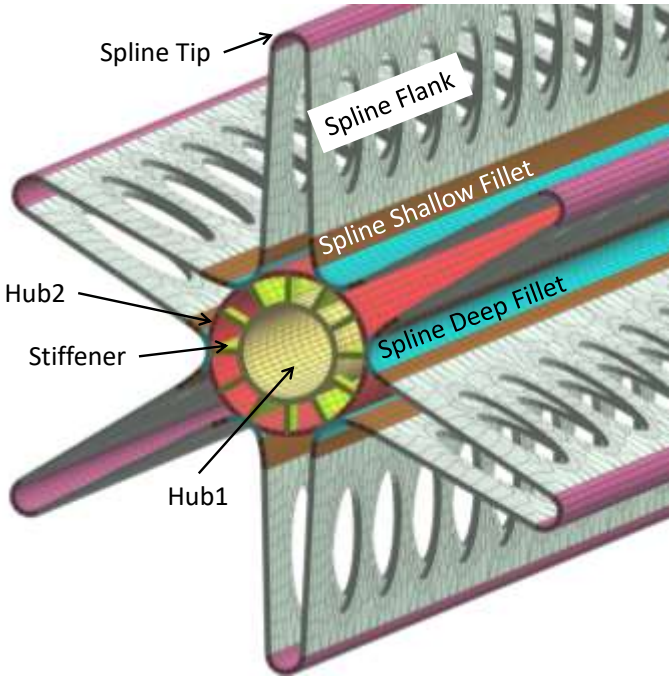

Figure 3.3. Hollow strongback components: safety factors' table.

4 Compensator Coil Optimization

There are currently no clear magnetic field safety requirements that impose limits on long-term exposure to static fields. Magnetic field safety requirements (1000 gauss) exist for controlled work environments (IEEE C95.6 Safety Standard, 2002 revisit 2007). A goal to keep habitat fields below 50 gauss is based on fields that can be tolerated by equipment such as computer hard drives.

The designed shielding array's compensation coil compensates for the return flux from the main shielding coils that penetrates the spaceship habitat, reducing the magnitude of the magnetic field in the habitat. The compensation coil also plays a role in thermal management of the solenoid coils as it intercepts thermal radiation from the habitat, which constitutes the largest heat source for the solenoid coils in deep space.

With a simple solenoid that has a constant current density distribution over the full length, the fringe field in the habitat still reaches a peak field of about 100 gauss, with an average value of about 65 gauss. Rest field for such a case is shown in Figure 4.1. Because this does not achieve the goal of 50 gauss, a more complicated configuration will be necessary.

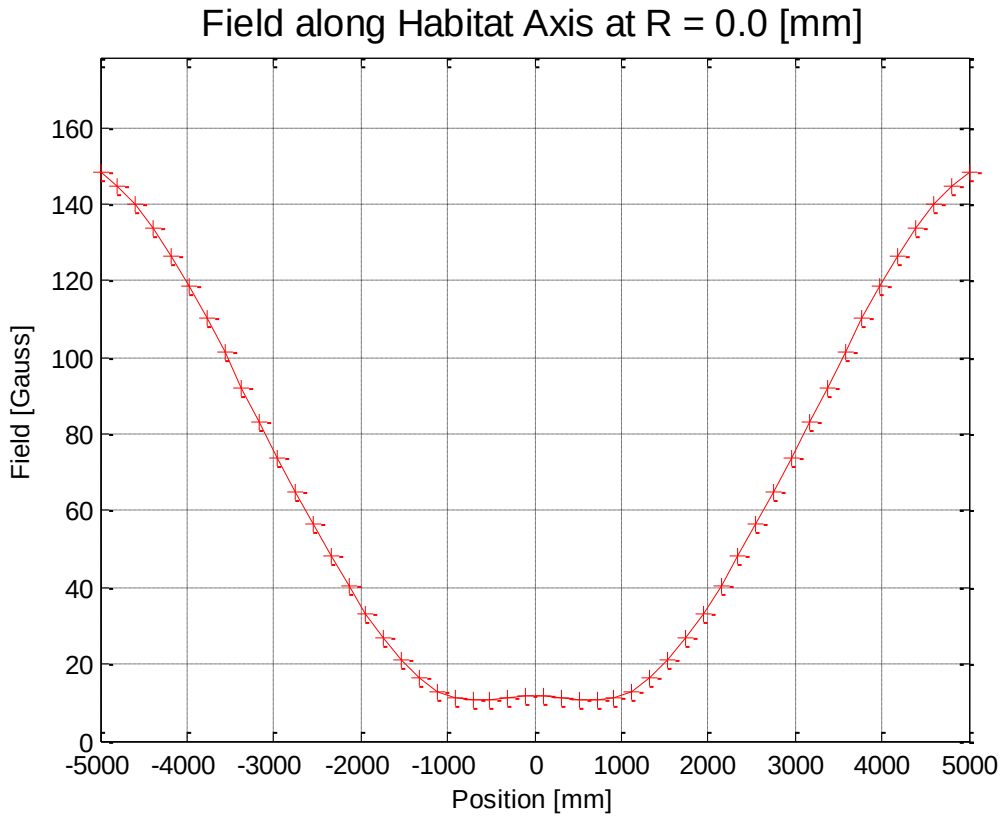

Figure 4.1. Rest field with unmodulated solenoid.
Coil has 7 m diameter and is 20 m long carrying 10.5 kA current. Mean field in habitat region ~66 gauss.

The fringe magnetic field in the habitat can be reduced significantly by adjusting the pitch length of the conductor (i.e., the distance between adjacent turns as a function of axial position along the solenoid coil). This approach is also used for the axial gradient coils on Magnetic Resonance Imaging (MRI) systems.

4.1 Gradient Coil Approach

With the gradient coil approach, the average field can be reduced by a factor of 10 to an average fringe field value of about 10 gauss. Field along axis for a possible solution is shown in Figure 4.2.

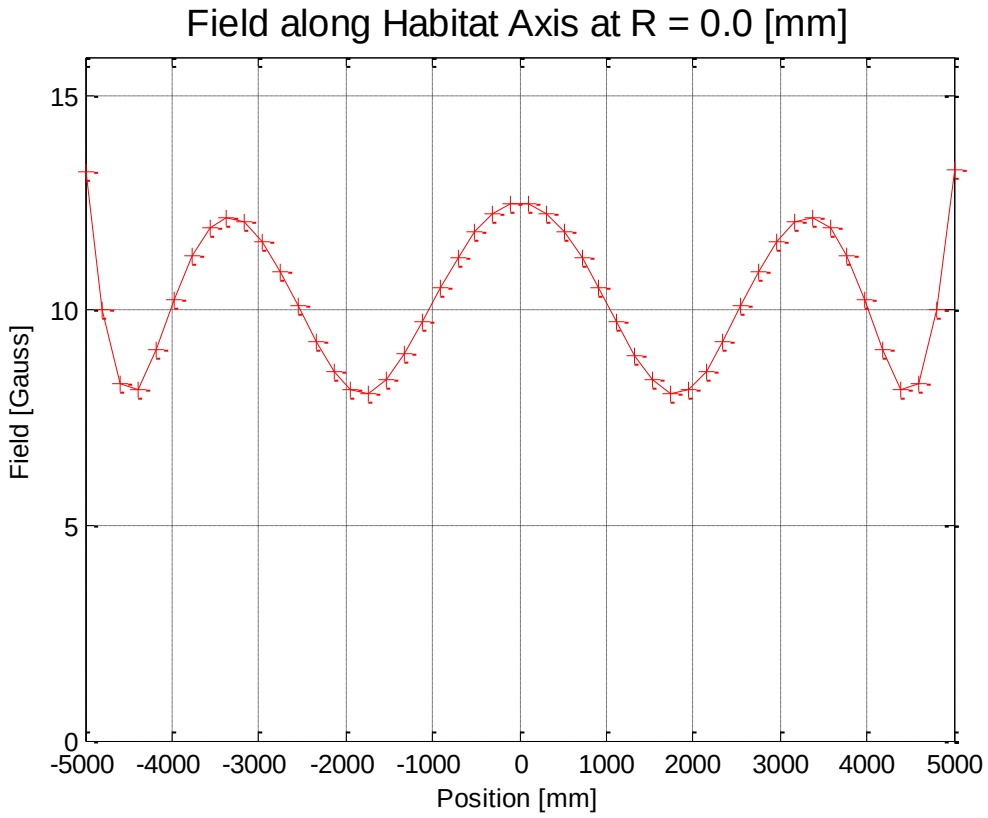

Figure 4.2. Rest field with modulated conductor spacing.
Coil has a 7.2-m diameter, and is 15.8 m long, carrying 10.22 kA current. Mean field in habitat region ~10.3 gauss.

This value could be reduced further by performing a numeric minimization. However, it would be difficult to build a coil system in which the pitch length of the solenoid coil is precisely controlled. In particular, distortions as a result of acting Lorentz forces would make this approach difficult to implement and does not seem to present a reliable and robust solution. To solve this problem, a different approach was pursued; the compensation coil was split into sections, which can be individually powered and controlled.

4.2 Split Solenoids Approach

MRI systems require utmost field uniformity, and correction schemes have been developed that allow field adjustments with high precision. The key technique being applied relies on multiple correction coils for the required precise field adjustments. Based on actual field measurements, the currents in specially designed correction coils are adjusted to yield the high degree of field uniformity needed for the MRI technique.

While MRI requires field adjustments in the mT range (i.e., $< 10^{-6}$ of the total field), the requirements for the compensation coils are much more relaxed, and a rest magnetic field in the range of a few tens of gauss should be sufficient. However, having a compensation scheme for the radiation shielding array that is adjustable is valuable. In particular, because the main solenoid coils of the shielding array will be distorted under the influence of acting Lorentz forces, it will be difficult to predict the resulting field in the habitat with high accuracy, and an adjustable compensation scheme is highly desirable.

The degree of adjustability needed for the compensation scheme is currently unknown, given the level of design maturity of the habitat. However, even a system consisting of only three solenoidal coils (Figure 4.3), which are distributed along the axis of the spaceship habitat, offer much flexibility, as shown by model calculations of the complete system. Without any numerical optimization, the rest magnetic field can be reduced to a few tens of gauss.

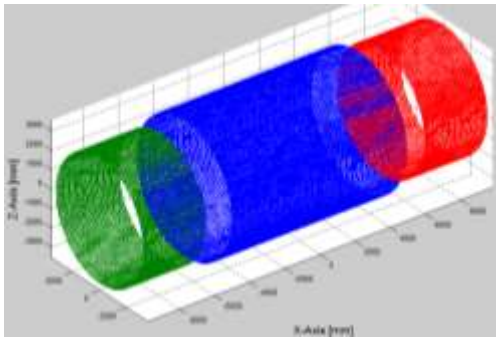

Figure 4.3. Split compensation coils.
Subdividing the compensation coil in individually controlled sections will allow for a robust, adjustable system.

A more complex system consisting of more coils can be designed, which could yield a high degree of compensation. It may be feasible to design a compensation scheme that could minimize rest magnetic fields in the habitat under extreme conditions where one of the outer large shielding coils is not functional at full field or even totally failed. The compensation procedure for such a scenario would require a field measurement at a few locations in the habitat, and a computer code would calculate the best operational currents for a set of compensation coils.

The complete design of such a compensation coil system is straightforward, based on similar approaches used for MRI magnets, and are therefore, not needed for a NIAC project. The AML team, therefore, has limited calculations to a compensation coil system consisting of three solenoidal coils. Figure 4.4 shows the results.

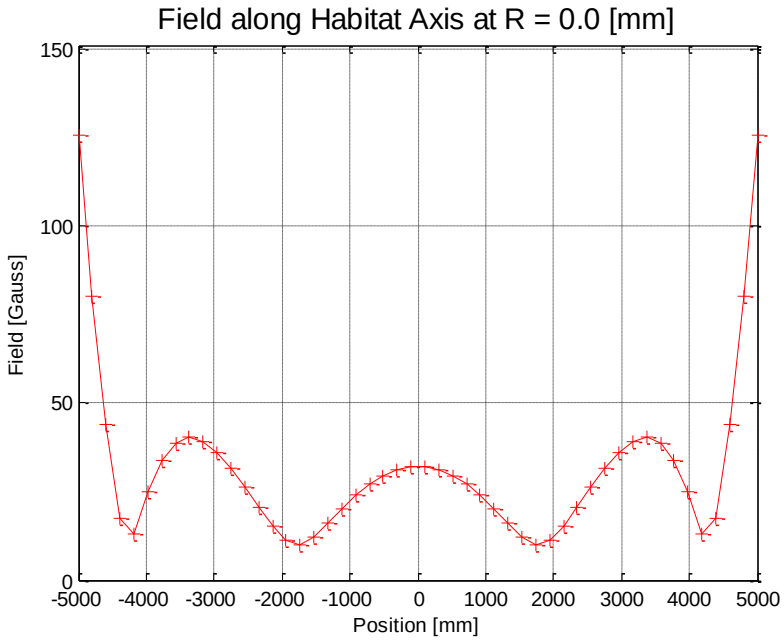

Figure 4.4. Rest field in an unoptimized 3 solenoid compensation system.

5 Forces on Incoming Space Capsules

The extended fringe magnetic field surrounding the solenoid system and its relatively strong field gradient will affect metallic and ferromagnetic components inside or entering this field volume. Any ferromagnetic material will be attracted in the direction of increasing flux density (i.e., in most cases, toward one of the six solenoids). Force on ferromagnetic object:

$$F_{mag} = \nabla * (U - U_o) * V$$

Where U is energy density with ferromagnetic material inserted, U_o is energy density without ferromagnetic material, and V is volume of ferromagnetic material. The ferromagnetic attraction will depend on the details of capsule construction and is difficult to model without such details. It is important to note that many satellites and space probes have been designed to minimize their magnetic signatures. This is a similar problem to that of designing for minimum magnetic force.

A metallic or conductive object, moving inside the fringe field volume, will have eddy currents induced. Because of induced eddy currents, Lorentz forces will result that are proportional to the velocity of the movement relative to the field. Induced eddy currents on large aluminum cylinders could be substantial since the temperature of the aluminum exposed to deep space can be in the range of 100 K, yielding high conductivity of the material. Docking maneuvers could be affected unless the relative velocities are small. The AML team has investigated this effect for an approaching space capsule with a crew and service module, dimension of which are shown in Figure 5.1.

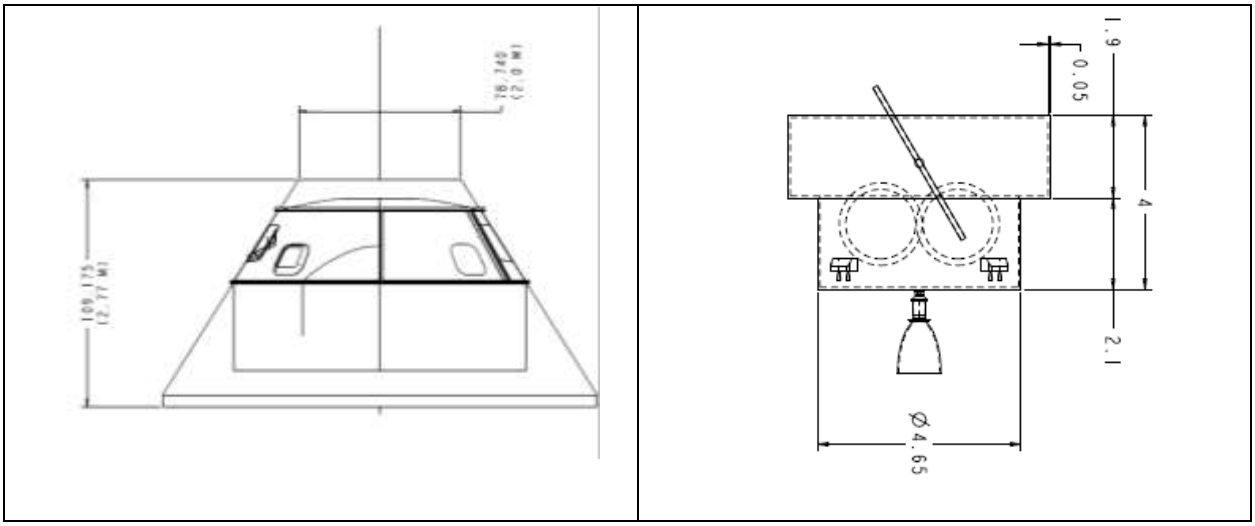

Figure 5.1. Figure showing the dimensions of the crew and service module of a space capsule.
Left figure shows the crew module, and the right figure shows the service module.

The crew module is simulated as a tapering cylindrical shell structure with the diameter varying from 2.0 meters (78.74 in.) to 5.11 meters (201.2 in.) with a length of 2.77 meters (109 in.). The thickness of the shell is 50 mm (2 in.). The service module is simulated as a cylindrical shell structure of a 6-m diameter and 5-m length. The material considered for the shell structure is Aluminum 2219. Aluminum 2219 has conductivity of 33.4×10^6 S/m at 50 K and 24.9×10^6 S/m at 150 K with relative permeability of 1.[8] The relative speed of the approaching space capsule is 0.1 m/s.

A model based on quasistatic approach was implemented in CoilCAD® to estimate forces on the capsule.[9] The quasistatic approach assumes that fields propagate instantaneously and that there is no impact on the field of solenoid array because of an approaching space capsule; both of these assumptions are valid for the present scenario. It is assumed that the space capsule will approach the solenoid array along the central axis. Figure 5.2 shows the net force on the space capsule as it approaches along the central axis. Figure 5.3 shows the force distribution on the crew and service module at a location close to the maximum net force. The net force on capsule scales linearly with the relative velocity of the approaching space capsule.

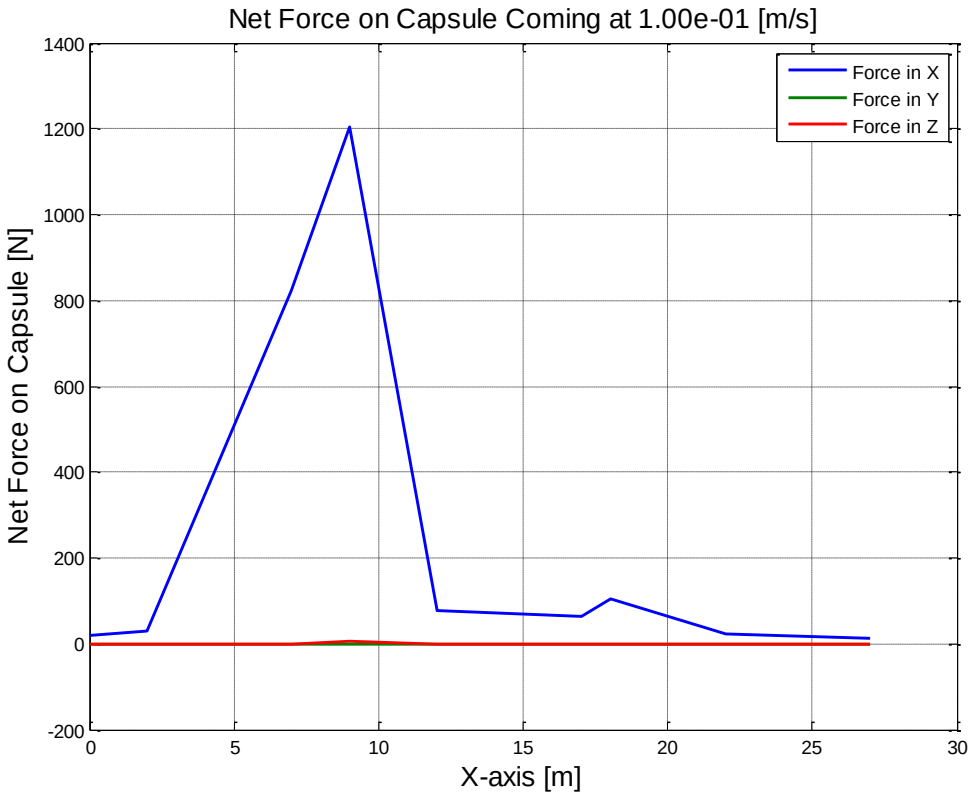

Figure 5.2. Force on space capsule as a function of approaching distance in axial direction.
The entrance of the solenoid array structure is at 10 m and the center of the structure is at 0 m.

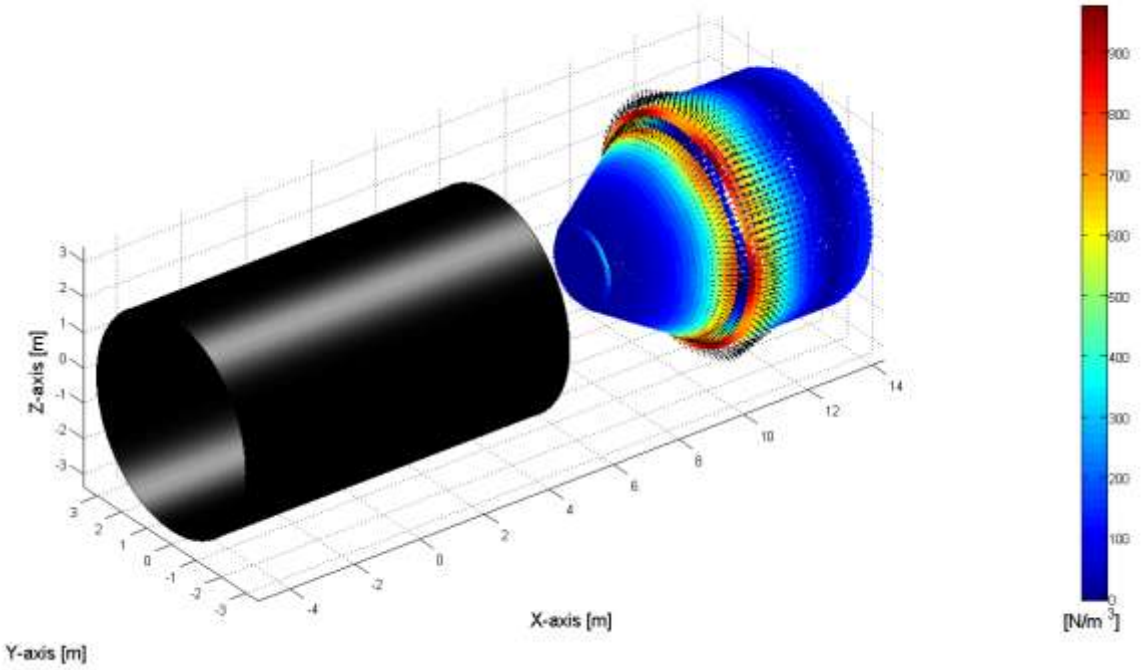

Figure 5.3. Forces on approaching space capsule close to the peak force location.

6 Interplanetary Magnetic Field

An Interplanetary Magnetic Field (IMF) with a flux density of a few nT (nano-tesla) is observed in the solar system. The field is caused by the Sun, which has a magnetic dipole field with a flux density of about 10^{-4} T near its surface. If space were a vacuum, the Sun's magnetic dipole field would be reduced with the inverse cube of distance. However, the solar wind, which behaves like plasma, carries the magnetic field into interplanetary space. The magnetic field, carried by the plasma orbiting Earth, is about 100 times greater than expected from the inverse cubic reduction, reaching a flux density in the order of a few nT. As a result of the Sun's rotation and the outward motion of the plasma, the magnetic field is pulled into a spiral pattern, resulting in a complex field distribution in interplanetary space.

During an interplanetary mission, the magnetic field of the superconducting shielding array coils interacts with the surrounding IMF. Like a compass needle in the Earth's magnetic field, coils will experience a torque, which acts in such a way as to line up their axis with the local IMF field direction.

For a better understanding of the acting forces and to develop the computational tools, a simple model was built, consisting of a single test coil embedded in a uniform magnetic background field. After the computational tools were developed, the test coil used in the model was replaced with the coils of the actual radiation shielding array. For a typical IMF flux density of 10 nT, the maximum torque acting on the whole radiation shielding array is about 40 N m (Newton meter).

If a rocket propulsion system is mounted 10 m from the center of gravity, a propulsion force of less than 5 N is sufficient to counteract the maximum torque acting on the shielding array. The linear force (as opposed to torque) on the coils is proportional to the gradient of the interplanetary magnetic field.

7 Shielding Coil Gap Analysis

Direct contact between the large shielding coils of the 6-around-1 array make the mechanical design of the coil structure difficult. However, spacing solenoid coils apart opens up gaps between the coils with low flux density, as seen in Figure 7.1. This is because long solenoid coils have small magnetic fields on the outside of the windings. Only the return flux is present in this area.

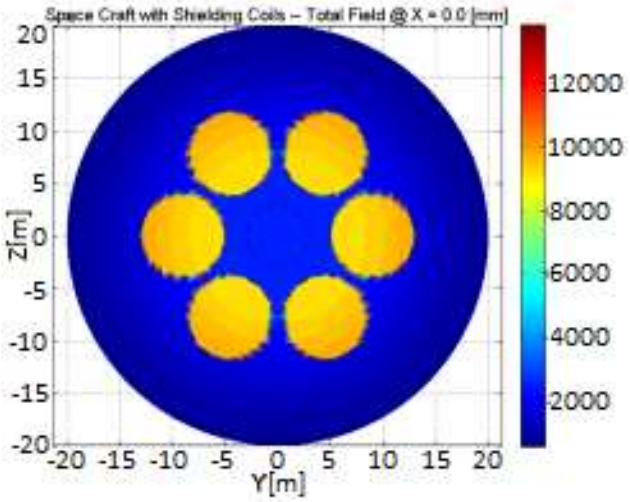

Figure 7.1. Field in a solenoid array with 1 m gap between coils.
The total field in the gap is significantly reduced and is 0.23T compared to 1T inside the coil.

By introducing a transverse magnetic field, component external magnetic fields are present on the outside of the winding along the cylinder. This is because the return flux for the transverse component is perpendicular to the coil axis and appears everywhere along the length of the coil.

A transverse field component can be introduced by tilting the windings of the solenoidal coils (Figure 7.2). In this case, for a single layer coil, the field on the inside of the coils is a superposition of axial and transverse magnetic field. The ratio of the two components depends on the tilt angle of the windings. With increasing tilt angle relative to the solenoid coil turns, the axial field component is reduced and the transverse component increases. And with an increasing transverse component, the external field increases.

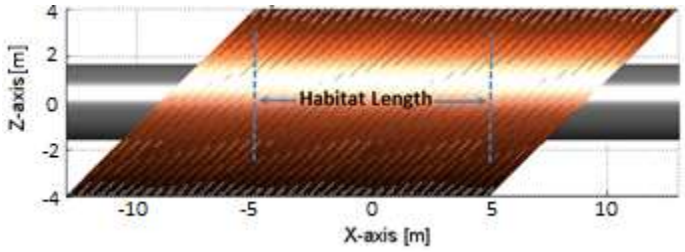

Figure 7.2. Base coil with 45-degree tilt.
It has tip-to-tip length of 25.97 m and 300 turns. The current of 55 kA is required to generate 1-T axial field.

When spacing the six shielding coils apart by moving their coil centers to a larger radius from the array center, the field strength in the resulting gap can be controlled with the tilt angle of the windings. The individual coils must be rotated relative to each other to have a continuous flux direction from coil to coil.

As a starting point, a 45-degree tilt angle has been chosen, which generates equal axial and transverse field components and creates a significant field strength in the gap between adjacent coils. For a base coil with a 45-degree tilt angle, the field and integrated field within an individual isolated coil are shown in Figure 7.3 and Figure 7.4. Also, the forces acting on such a winding were analyzed, presented in figures 7.7 through 7.10, and compared with the forces acting on a pure solenoidal coil configuration.

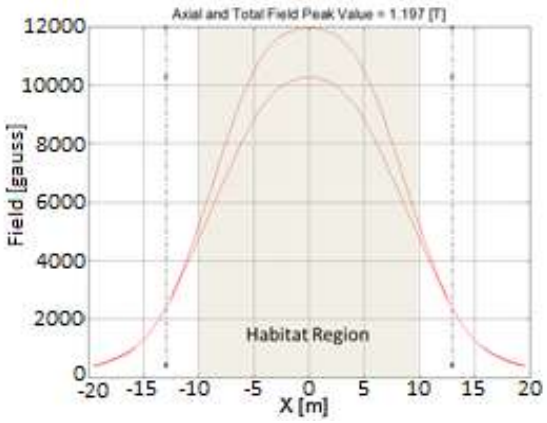

Figure 7.3. Axial and total field vs. axial position.

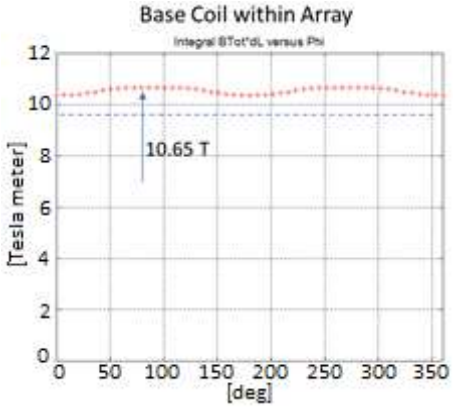

Figure 7.4. Integral BdL vs. azimuth angle.

Based on the 45-degree base coil 6-around-1 array configurations with gaps between adjacent coils of 0.5 m, 1.0 m and 1.5 m have been modeled and the fields in the gaps have been determined. All three configurations show significant field strengths in the gaps, which are close to the fields inside of the coils.

The fringe magnetic field in the habitat has been determined. This field consists of a superposition of a strong axial field, which is similar to the case of pure solenoid base coils. However, because of the transverse magnetic fields, a 12-pole transverse field component is also present. Both the solenoid field and the 12-pole field can be easily canceled with a compensation coil surrounding the habitat. Generating the required 12-pole component can be done easily by modifying the compensation coil.

Figures 7.5 and 7.6 give details of the field.

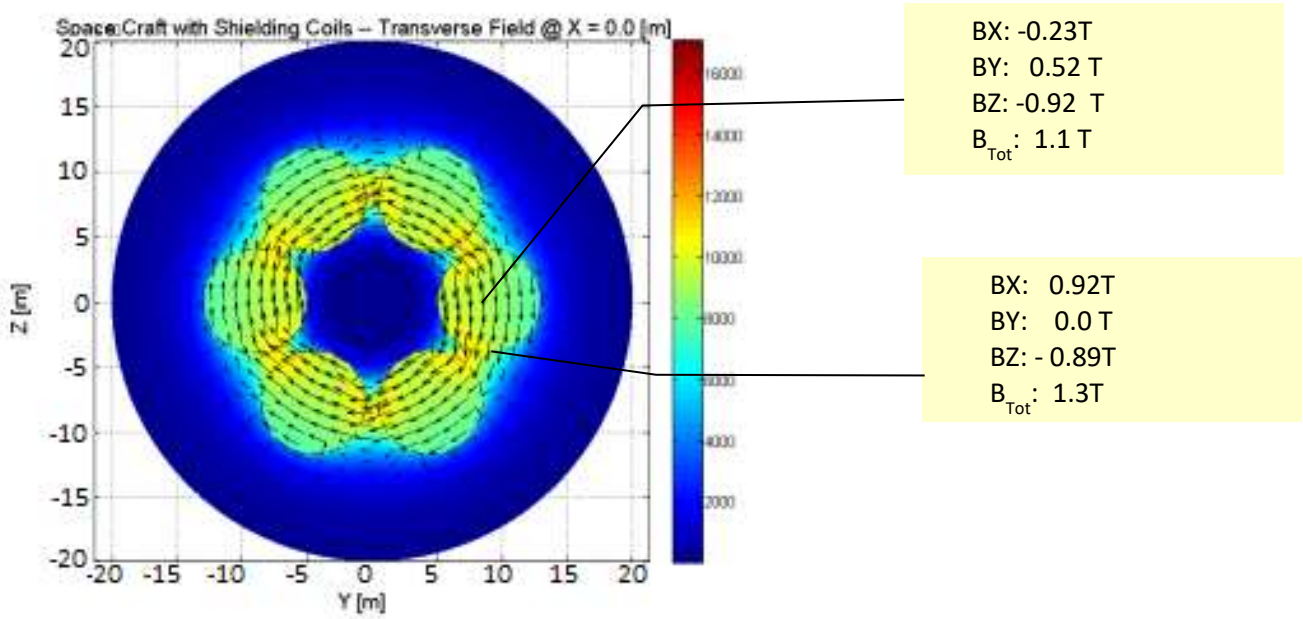

Figure 7.5. 1-m gap at closest distance – Transverse Field.

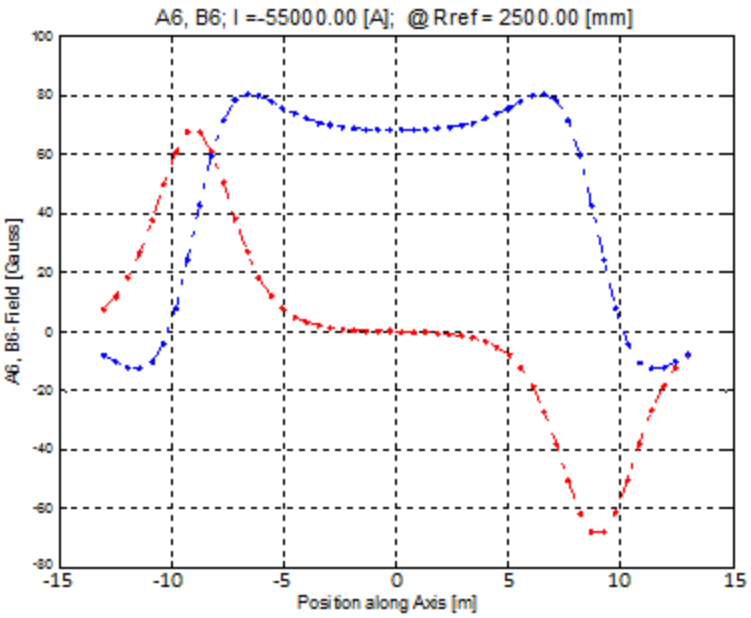

Figure 7.6. Field inside the habitat.

Finally, the forces acting on the coils within the array configuration with tilted turns have been determined. For pure solenoid coils, it was previously shown that strong repulsive forces act on the individual coils. Figures 7.7 through 7.11 show the forces on the coils. The studied baseline configuration with 8 T·m showed a repulsive force of about 10 MN acts on each coil.

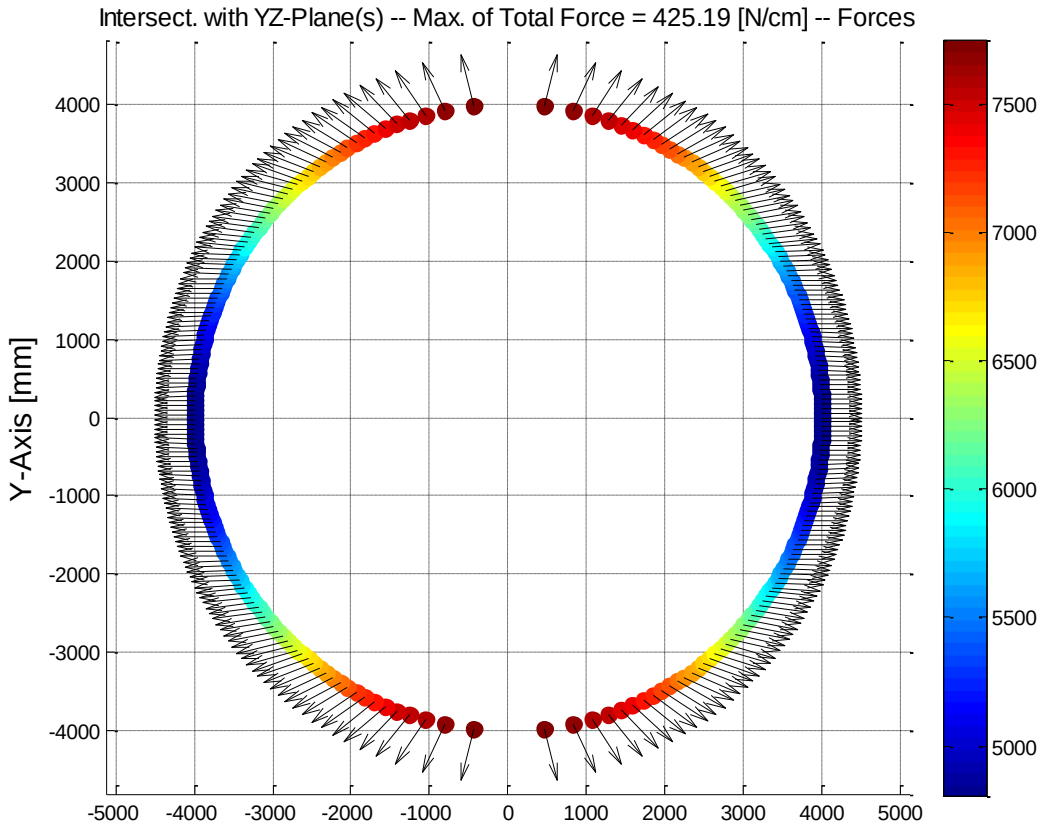

Figure 7.7. Force vectors acting on cylinder.

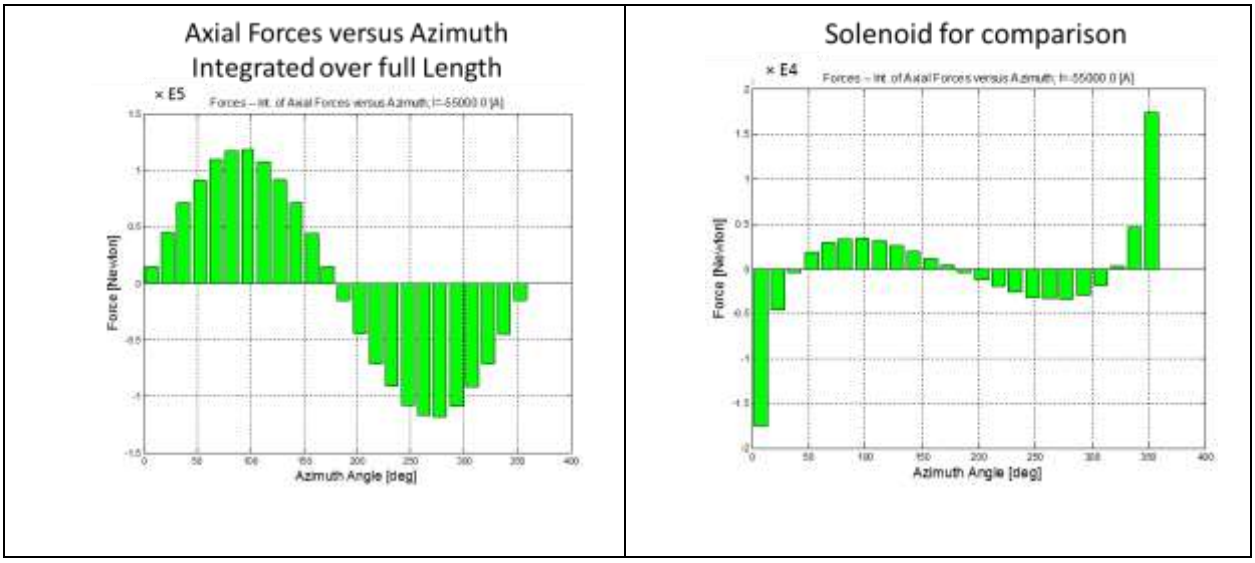

Figure 7.8. Axial forces.

Axial forces at the closest distance for 1 m gap case (left). Axial forces in a solenoid for comparison (right).

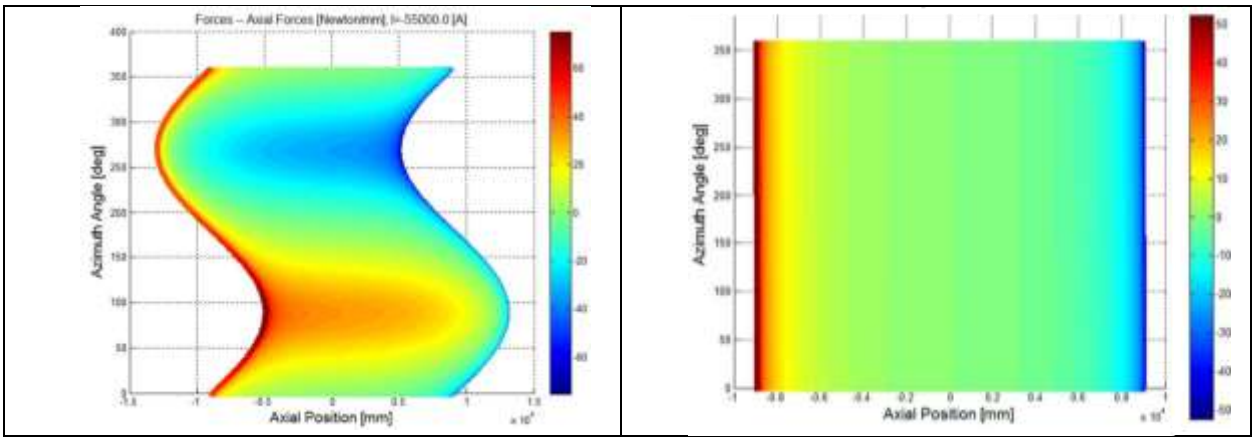

Figure 7.9. Axial forces over surface.

Axial forces at the closest distance for 1 m gap case (left). Axial forces in a solenoid for comparison (right).

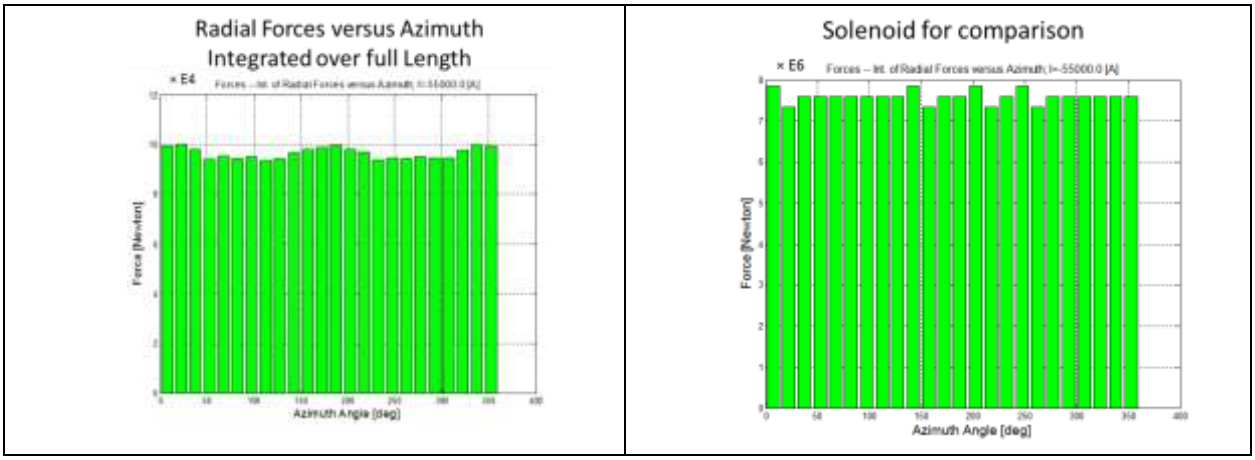

Figure 7.10. Radial forces.

Radial forces at the closest distance for 1 m gap case (left). Radial forces in solenoid for comparison (right).

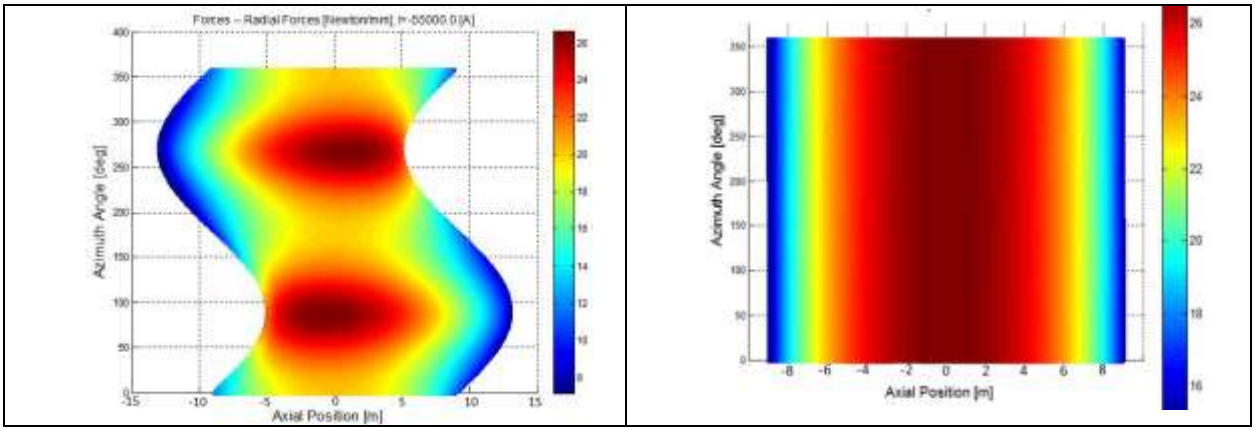

Figure 7.11. Radial forces over surface.

Radial forces at the closest distance for 1 m gap case (left). Radial forces in solenoid for comparison (right).

In contrast to the baseline configuration with solenoid coils, it has been shown during Phase I that for an array with pure transverse magnetic fields, the individual coils attract each other, putting substantial pressure onto the habitat.

Because both configurations (i.e., the axial fields (solenoids) and the transverse fields (double-helix)) generate forces in an opposing direction, a configuration with vanishing forces should exist. A scan has been performed by varying the tilt angle of the windings between zero degrees and 45 degrees, as shown in Figure 7.12. For a tilt angle of about 26 degrees, the forces between coils are close to zero. This configuration could have important consequences on the strongback of the individual coils and reduce its required bending strength and weight.

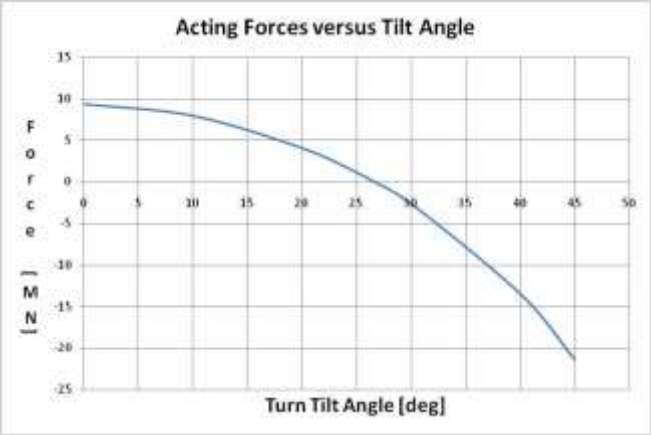

Figure 7.12. Force on coil for tilt angle of the windings between zero degrees and 45 degrees.
For tilt angles between 25 degrees and 30 degrees, the forces between coils cancel.

The performed analysis concluded that the six coils of the 6-around-1 array can be spaced apart without introducing gaps with vanishing magnetic flux, which would reduce shielding efficiency. By introducing a transverse field component, a sufficient flux can be maintained in gaps of about 1 m. An additional, significant advantage of such field configurations is that forces acting on the individual coils within the array can be significantly reduced. The required coils still consist of single layers. The field in the habitat can be compensated for pure solenoids.

8 Increasing Radiation Shielding Efficiency – Scaling of Integrated Field Strength

The baseline configuration developed during Phase I of this NIAC project for an active radiation shield consists of six solenoid coils; each has an 8-m diameter and a 20-m W length. Burger used Monte-Carlo calculations to estimate the resulting shielding efficiency of this configuration, without accounting for the extended fringe magnetic field. Table 8.1 shows the results.

Table 8.1. Annual Dose Equivalents in cSv/rem

Z	8 Tm - 36 t			20 Tm - 72 t		
1	7.9	7.6	7.4	6.4	5.8	5.9
2	3.8	3.4	3.4	2.9	2.7	2.6
3-10	15.4	10.8	5.2	9.6	7.0	2.8
11-20	12.6	6.9	5.2	7.0	4.3	2.9
21-28	5.6	2.1	2.0	3.6	1.6	1.3
Total	45.3	30.8	23.2	29.5	21.4	15.5
fraction of 8 Tm dose :				0.65	0.69	0.67

Skin (blue), Blood-Forming-Organs (red), and Body (green) for a 6-around-1 solenoid configuration with 8 and 20 tesla meter in the habitat region of the spaceship for a solar minimum. The last line below the tables shows the dose reduction for the 20 tesla meter configuration compared to the 8 tesla meter configuration.

As Table 8.1 shows, for an extended human exploration of deep space, a further increase in shielding efficiency over the baseline shield configuration with 8 tesla meters desirable. Such an increase can be achieved with either stronger, larger, or stronger as well as larger shielding magnets.

Since the bending radii of charged particles in magnetic fields are inversely proportional to the flux density seen by the traversing particles, it might seem advantageous to use magnets with high-field strength (in the range of many tesla). However, the analysis performed during Phase I showed a clear advantage for a solution with large magnets of modest field strength. Conventional magnets with dimensions of many meters are too massive for space applications. However, using the expandable magnet concept, proposed by AML, ultra-lightweight magnets (lighter than equivalent conventional magnets by orders of magnitude) with 8-m diameter and a nominal field strength of 1 tesla become feasible.

The developed baseline shield configuration suggests ways in which the shielding efficiency can be increased. To improve shielding efficiency, the value of integral B × dL (i.e., field strength integrated

over the path length in the field) must be increased. Any increase in the value of field strength of the magnets or dimensions of the magnets has advantages and disadvantages as discussed in Section 8.1.

The Monte-Carlo calculations presented in Table 8.1 indicate that an increase by a factor of 2.5 from the baseline value of 8 tesla meter to 20 tesla meter would yield a substantial improvement in shielding efficiency. An integral B × dL value of 20 tesla meter or even larger has therefore been chosen as a goal for the analysis presented here.

Table 8.1. Comparison of Key Parameters for the Radiation Shield Solenoid Array with Integrated Fields in the Range of 8 Tesla Meter (Baseline Design) to 25 Tesla Meter

Parameter	8 T m	20 T m	20 T m	25 T m
Flux Density	1.0 T	2.5 T	1.0 T	1.5 T
Diameter	8.0 m	8.0 m	20 m	16.7 m
Length	20 m	20 m	30 m	25 m
Volume	1,053 m^3	1,053 m^3	9,425 m^3	5,475 m^3
Current	43.5 kA	108.8 kA	50.0 kA	72 kA
Stored Energy	410 MJoule	2,520 MJoule	4580 MJoule	5440 MJoule
Inductance	0.43 Henry	1.1 Henry	3.7 Henry	2.1 Henry
Number of Turns	400	400/1000	600	500
Magnetic Pressure	4 atm	25 atm	4 atm	9 atm

8.1 Advantages and Disadvantages of a Sole Increase in Field Strength of the Solenoids

There are several qualitative advantages and disadvantages of a sole increase in field strength of the solenoids, while keeping their dimensions unchanged.

The field strength in the coil must be raised to 2.5 tesla to reach the target of 20 tesla meter. An advantage of this approach is that the unchanged size of the coil does not require more space for the launch vehicle, although a weight increase of the solenoids is unavoidable. Disadvantages of this approach rise from the required increase in ampere-turns of the solenoids. Calculations of the field strength in the solenoids show that the operational current must be increased to 100 kA, which requires a significant increase in current-carrying capacity of the superconductor, given the preferred single-layer solenoid configuration. In particular, this larger current now needs to be accommodated at the increased field of 2.5 tesla, instead of 1 tesla. The required large-current-carrying capacity could be achieved with a superconducting cable instead of the single-layer tape assumed for the baseline configuration. However, this approach would affect the flexibility of the conductor and, therefore, the assumed expandability of the solenoids. A more detailed structural analysis is required to determine how a stiffer conductor would impact expandability. An alternative approach to reduce the

requirements on current-carrying capacity would be to use the same tape conductor in multi-layer solenoid. As described during Phase I, multi-layer solenoids are more difficult to cool, are more complex in manufacturing, and also increase the peak field in the solenoid winding to values significantly higher than the nominal target field of 2.5 tesla. This again would increase the conductor requirements. Another disadvantage of a multi-layer solenoid operating with a lower current is the increased inductance of the coils. Since peak temperature and peak voltage are proportional to the coil inductance if a quench occurs, quench protection of such coils would become more difficult. An increase in field strength also affects the forces acting on the solenoids. In particular, the increase in axial forces would require much stronger support structures of the coils, and much larger repulsive forces acting between the six solenoids need to be accommodated.

An alternative approach for reaching an integrated field of 20 tesla meter is to keep the field strength at 1 tesla, but increase the coil dimensions to a diameter of 20 m instead of 8 m. A clear advantage to this approach is the unchanged requirements of the conductor performance. The current-carrying capacity of the conductor remains unchanged compared to the baseline design. Because of the much larger coils, the extension of the fringe magnetic field increases significantly, which should have an additional positive effect on the shielding efficiency. The larger diameter of the solenoids surrounding the spaceship habitat also introduces a drift space between the solenoids and the habitat, which would increase the shielding efficiency of the system. Because of this additional space, the energy for cosmic ray particles that can still reach the habitat after being bent in the solenoids is increased, and accordingly, the shielding efficiency of the radiation shield is significantly improved over the values for radiation doses as shown in Table 8.1.

The disadvantages of the increased coil dimensions include the increased length of conductor. More conductor splices are needed and the coil inductance is increased, which makes quench protection more difficult. The significantly larger dimensions will also increase the requirements on the stiffness of the solenoid strongbacks and the required stiffeners that counteract the axial Lorentz forces. Finally, the increased dimensions place additional requirements on the launch vehicle or require more launches because it may not be possible to send a full set of coils in one launch.

The approach that will be selected to constitute the optimum solution will depend on the difficult-to-predict technical advances that can be achieved in the coming years in various fields. Given this lack of knowledge, it is prudent to also consider a combined increase in field strength and coil dimensions. For this reason, the team has analyzed, in more detail, a configuration in which the field strength of the solenoids is raised to 1.5 tesla, and the coil diameter is enlarged to 16.6 meter. The resulting increase in the integrated field would be even larger than the target value of 20 tesla meter, reaching about 25 tesla meter. Figure 8.1 shows the coil configuration of this scenario. An advantageous feature of this design is again the large drift space between the habitat and the surrounding six solenoids.

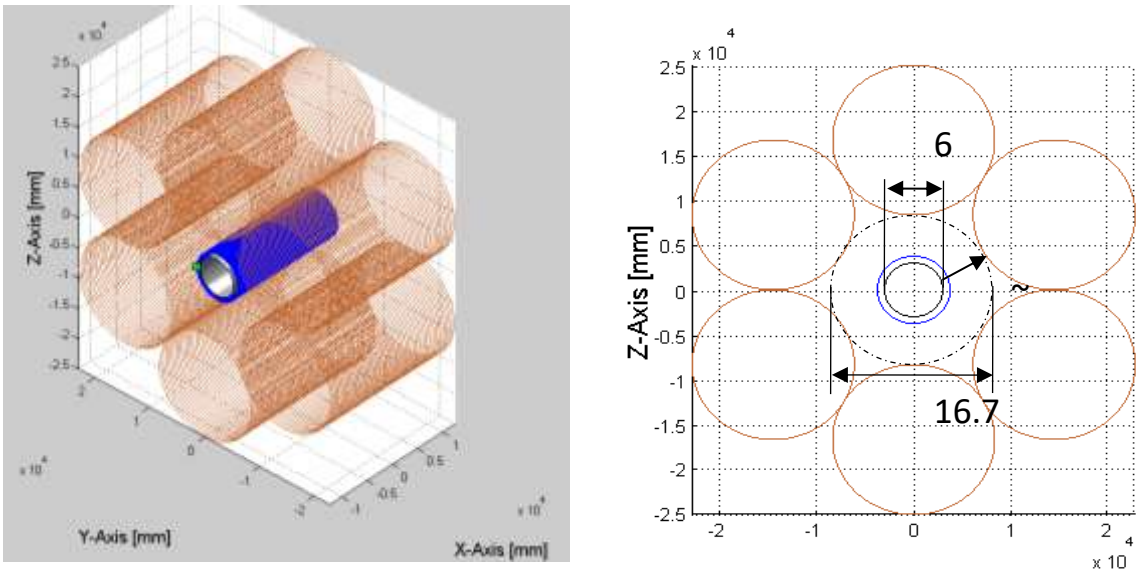

Figure 8.1. Isometric view and cross-section of increased shield array.
The blue cylinder in the center is the compensation coil that surrounds the spaceship habitat (shiny gray cylinder). The solenoid coils are shown in brown.

The operational current needed to reach a field strength of 1.5 tesla for these coils is about 70 kA, constituting a significant increase over the baseline design, and an increase in current-carrying capacity of the superconductor over the baseline design is needed to reach the field strength with a single-layer coil. The overall inductance of this configuration is larger than for the baseline design, which is a result of the increased field volume and the increased field strength. If the diameter of the solenoid is increased, the length should also be increased to maintain a constant aspect ratio. This is necessary to avoid a significant reduction of field strength at the ends of the solenoids, which is determined by the aspect ratio of coil diameter to coil length.

Figure 8.2 shows the field distribution along the solenoid axis for a coil length of 25 m, instead of 20 m for the baseline design, which shows that the field strength over the 10 m length of the habitat is greater than 1.4 tesla for a current of 72 kA. The larger coil dimensions require the need for more superconductor and, therefore, more conductor splices, since it is unlikely that YBCO tape with sufficient length for a complete coil can be produced. However, recently it has been shown[5] that superconducting splices for YBCO tape conductor are feasible, a development that supports the presented radiation shield approach.[10] Another important parameter for the design of the considered radiation shields is the repulsive force acting between the six solenoid coils. The acting force for the 25 tesla meter configuration is presented in Figure 8.3, which shows that the total repulsive force increases by a factor of about 6.

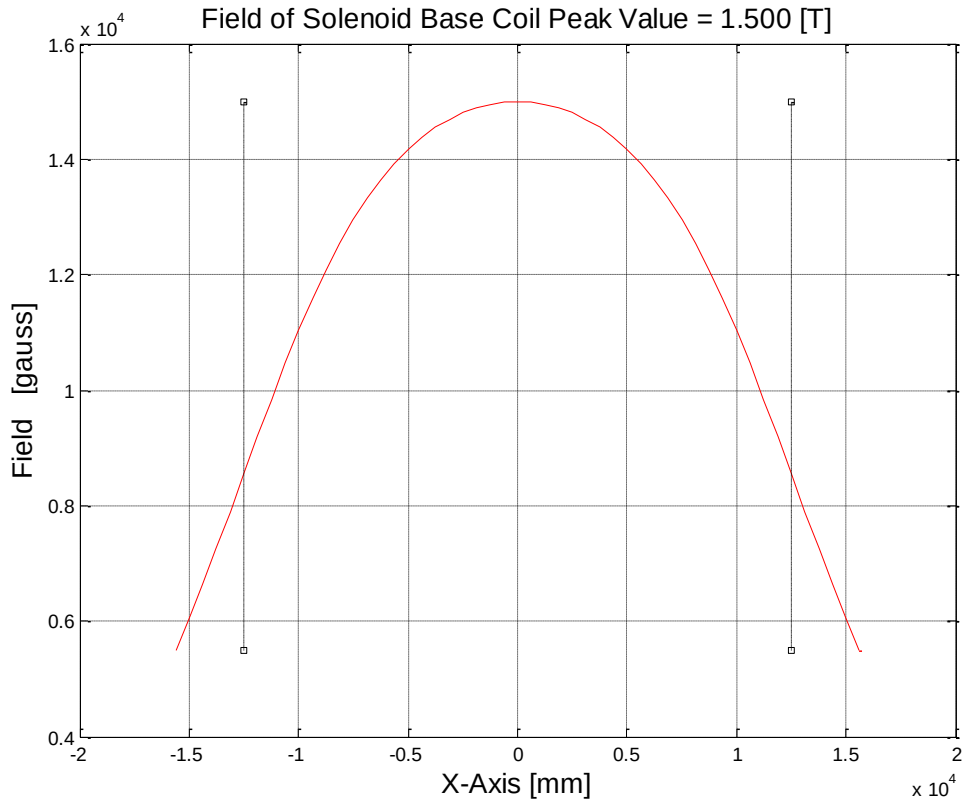

Figure 8.2. Axial field distribution for the solenoid with increased field strength and length.
The dashed lines indicate the physical ends of the coil.

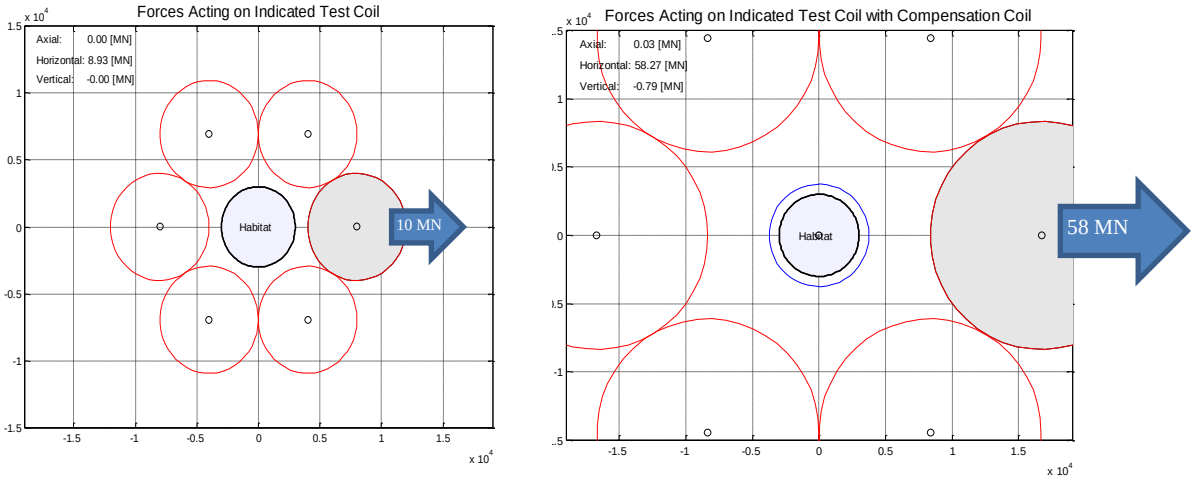

Figure 8.3. Complete repulsive force.
Left: Complete repulsive force acting on individual solenoid coil (~10 MN). Right: Complete repulsive force for a solenoid of the enlarged 25 tesla meter system (~58 MN).

A comparison of key parameters for the three enlarged shielding solenoids and the baseline design are presented in Table 8.1 (the indicated pressure is estimated from the simple analytic formula P_m =

$B^2/(2m_o)$, which describes the magnetic pressure). It is clear that a detailed analysis of the competing designs is needed to find the optimum solution. However, there is significant potential for an increase in shielding efficiency over the baseline design, given the unique, expandable coil configuration. The presented configuration of 25 tesla meter would have a significantly better shielding efficiency than the estimates presented in Table 8.1. However, to determine the actual improvement in shielding efficiency, a Monte-Carlo calculation is needed, in which the full array is represented, and the large fringe field surrounding the whole configuration is considered.

8.2 Strongback Mass Estimate

For the baseline design, 8 T·m rigidity, the design team estimates the strongback and solenoid coil structures weight at 7,145 lbm (3,240 kg). While detailed study on strongback design and mass optimization was done only for the baseline design, it is possible to estimate strongback mass for the other variants based on the identified scaling relationship between the acting loads and the strongback mass. In particular, the radial repulsion forces are the governing design load for the strongback. When estimating masses for coil variants, it is important to understand the effects of composite layup definitions on load reactions. For the proposed 25 T·m case, the radial repulsive forces are six times that of the baseline case, resulting in an estimated strongback mass of 37,120 lbm (16,837 kg).

9 Quench Detection and Protection

See Appendix B for complete analysis.

Various fault scenarios could trigger quench in the superconducting coils of the array. It is critical to study quench propagation and provide enough safety margin in the design of superconducting coils and also to provide a mechanism to safely discharge the stored magnetic energy and recover quickly when quench happens. The AML team has investigated the safety margin in the present coil design and offers solutions for the quench detection and quench protection detailed in Appendix B.

New software to simulate the quench propagation process in rare-earth barium copper oxide (ReBCO)/YBCO tapes combining thermal model, electric model, and superconductor properties was implemented in CoilCAD® and verified against ANSIS®. This code simulates a 2-D propagation of heat on the surface of a cylinder and uses a lumped model to describe the thermal and electric properties of the tape. A new 2-D Finite Difference Method (FDM) for heat equation optimized specifically for the coil geometry and boundary conditions has been implemented.

Quench propagation studies show that the minimum quench energy at operating temperature is ~4 Joules. This large value of the minimum quench energy allows the system to recover and survive many fault scenarios. A peak temperature of 108 K, significantly lower than 300 K maximum limit, is predicated from simulations. The peak voltage across the coils during the quench process is limited to 10 kV. External dump resistors of 0.25 Ohms will keep the voltage within this requirement. An external dump resistor made of SS-304 cylindrical shell has been proposed and can be an integral part of the support structure.

Quench propagation studies predict a small Normal Zone Propagation Velocity (NZPV) of ~5.5 cm/s. The small NPZV eliminates the conventional voltage-based quench detection technique in solenoids. A new method based on optical fibers is proposed for quench detection. Optical fibers will be placed in the close proximity or integrated into the design of YBCO tape to respond quickly to temperature changes. A quench detection based on interferometry measurement can then be used to detect quench within 1 millisecond.

For the quench study, YBCO tape with a 100-mm width and 40 kA at 27 K current-carrying capacity was assumed. The ReBCO/YBCO tapes currently available do not have such current-carrying capacity, the width or the single piece length required for such a solenoid coil. But all the developments indicate that such a tape can be available in the next few years. The analysis also provided a clear direction on defining the properties of an ideal YBCO tape for the solenoid coils. The copper stabilizer layer in the YBCO tape could be replaced by a higher thermal conductivity material like graphene, which also has higher yield strength, to further increase the minimum quench energy. Section 11.0 describes this idea in detail. More analysis is needed to arrive at an optimized YBCO tape configuration suited for the solenoids.

10 Expandable Coil Testing at AML

In superconducting magnets with a field strength of 1 tesla or above, strong Lorentz forces act on the conductors. The vast amount of existing experience with such magnets showed that the conductors in these coils must be mechanically well stabilized to avoid premature transitions from the superconducting to the normal conducting state. In most of such high-field magnets, even the conductor's microscopic movements of a few microns under the effect of the Lorentz forces are sufficient to cause a quench (i.e., a transition from the superconducting to the normal conducting state), preventing these magnets from being functional. However, this experience is based on magnets that are made with low-temperature superconductors (LTS), mainly NbTi, which has to operate near the temperature of liquid helium (~4.2 K). The sensitivity of LTS conductors to any movements is mainly caused by the vanishing specific heat of materials near absolute zero and the release of frictional energy, when conductors move inside of coils.

High-temperature superconductors (HTS), like ReBCO, offer the potential to overcome the problem of premature quenching under the effect of acting Lorentz forces. These conductors remain superconducting at much higher temperatures, even above LN2 (77 K), where the specific heat is much larger, and under these conditions, the operational margin of the conductor becomes much larger. Movements of conductors do not necessarily generate enough heat to cause a quench of the conductor. If, in addition, coils are built to allow conductors to move under the effect of Lorentz forces, without generating significant amounts of heat, such coils should not show premature quenching.

Based on these factors, AML suggested that large high-field magnets should become feasible, and these magnets would be able to change their shape over large fractions of their coil cross-section and expand under their own Lorentz forces. Such "foldable" magnets, which are similar to balloons, would offer unique applications. Particularly, large magnets similar to the size of blimps are conceivable and would offer unprecedented opportunities for space applications, since magnetic fields with large volumes surrounding a spaceship could be used for radiation protection.

With small funding from NASA and the Space Florida agency, AML developed a small superconducting YBCO coil to prove the concept of expandability without quenching of the conductor (Figure 10.1).

A small coil was built and tested recently at the National High Magnetic Field Laboratory. The coil constitutes a solenoid, which is supported by a silk cylinder and a strong back in the center of the coil. The tests were performed in liquid helium and the coil was ramped up and down in 1 sec to 110% of the limit allowed by the current leads of the setup. When the full field was reached, the shape of the coil was mechanically varied over the full range allowed by the coil construction.

The resulting flux change caused by the shape change of the coil was observed with voltage taps connected to the YBCO coil, and by similar voltage taps of a surrounding field coil. No quench was initiated in repeated tests, not even by complete shape changes with a duration of about 1 sec or less, which was the fasted possible.

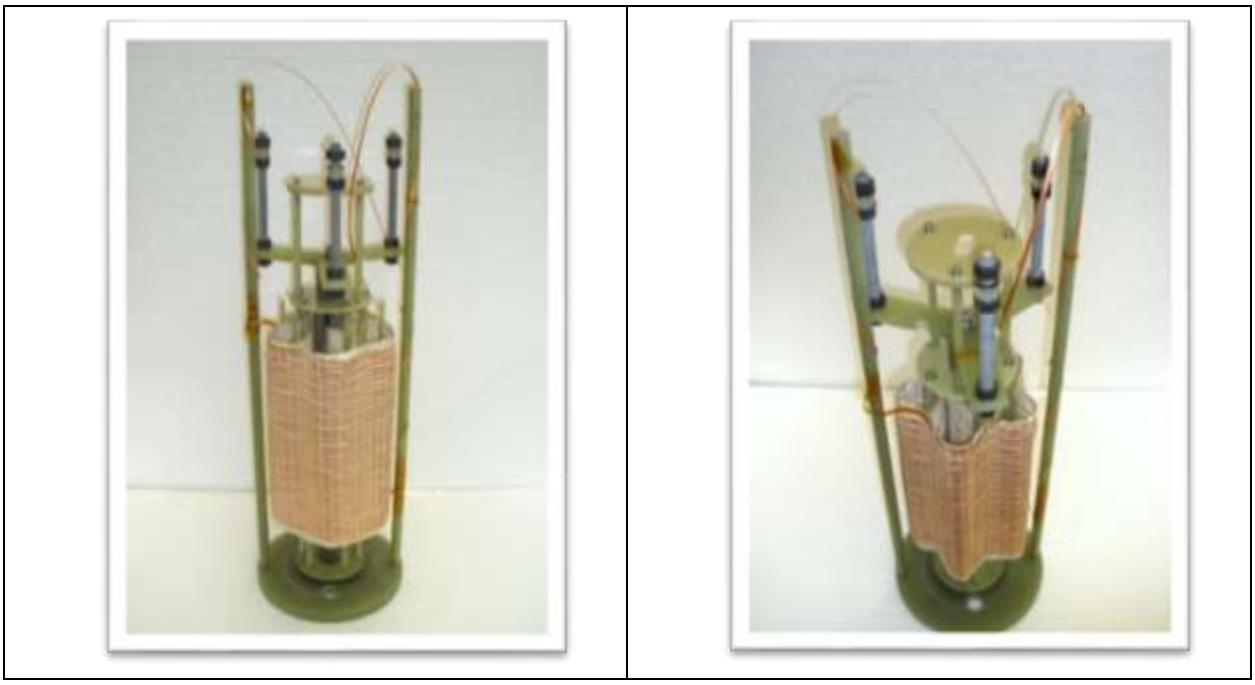

Figure 10.1. Test coil with support structure.
Uncollapsed coil (left) and fully collapsed coil (right).

Main achievements of expandable coil testing:

1. Flexible support structure and related manufacturing process for YBCO coils were developed.
2. Expandable YBCO coil with flexible support structure is being built.
3. YBCO coil ramped to 110% of nominal current rating of current leads.
4. Coil successfully operated at current ramp rates of more than 100 A/sec, which is beyond the requirements for expandable coils.
5. Coil shape manually varied between fully collapsed and fully expanded at 110% nominal current without quench.
6. No quench initiated at fastest possible shape change over full range.
7. Flux change caused by shape change of expandable coil measured with voltage taps on expandable coil.
8. Flux change caused by shape change of expandable coil measured with voltage taps on surrounding background field magnet.

Based on the obtained results, there is no doubt that the developed YBCO coil will expand without quench, given sufficient Lorentz forces. These forces are the product of transport current in the conductor

and the surrounding magnetic field. There is no difference in Lorentz forces, if the field is generated by the coil or by an external source.

The AML team anticipated that an external superconducting high-field magnet could cause the shape change of the expandable coil. However, the following issues with this magnet's operation prevented the external field from being used:

1. A technical difficulty prevented the team from optically observing the shape change of the magnet.
2. The camera, housed in a vacuum-jacketed tube inserted into the test cryostat, became too cold for operation.

To solve both of these problems would have required warming up the test cryostat, doing repair work, cooling down the test cryostat again with liquid helium, and repeating the test. The high cost of liquid helium and operation at NHMFL prevented the team from doing this work, given the limited funding available for the experiment.

11 HTS Coil Thermal Structural Analysis

See Appendix C for the complete analysis.

A YBCO HTS tape in a large-scale solenoid magnet is analyzed to compare and contrast the thermal structural response of the tape when using graphene instead of Hastelloy® for the tape substrate. By embedding the tape in a high-strength fiber (HSF) construct, the necessary thermal management to avoid conductor quench may be possible. In these analyses, the HTS tape is considered to be a single construct and an embedded construct in a high-strength fiber solenoid. The modeling and simulations are based on YBCO tape used in the following configurations:

1. YBCO tape constructed with a Hastelloy® substrate
2. YBCO tape constructed with a graphene substrate
3. YBCO tape constructed with a Hastelloy® substrate and embedded in HSF solenoid
4. YBCO tape constructed with a graphene substrate and embedded in HSF solenoid

NASA is considering using HTS technology to develop magnets to protect against galactic cosmic radiation (GCR), a protection that is essential for human deep-space exploration. These high-field magnets are subject to large Lorentz forces requiring a complete understanding of the thermal structural response of the superconductor and a complete understanding of the structural assembly.

Current HTSs are based on construction using Bi2212 or YBCO. Strain strongly influences the structural performance of HTS magnets. Phase I analysis suggests that conductors based on Bi2212 demonstrate poor mechanical properties and that most of the strain margin for these conductors is wasted on bending strain associated with fabrication. As such, this analysis is based on the construction of a 3-D YBCO HTS (tape) model consisting of all conductor components embedded in a 3-D support structure developed during Phase I.

In the Phase I analysis, the YBCO HTS was one of several components making up a large diameter high-field solenoid manufactured at room temperature and deployed in deep space. A key requirement for solenoid construction is that the supporting structure for the conductor must be flexible and support folding when the coil is not energized. This requirement is rooted in constraints associated with packaging for launch and subsequent coil deployment in a deep-space environment.

The notional model for the coil support structure is developed from high-strength fiber (HSF) technology. An inner HSF cylinder acts as the base for winding the conductor. The conductor is 50 mm wide and the spacing between windings is 1 mm. An outer HSF cylinder is formed and molecularly bonded to the inner HSF cylinder by applying temperature and pressure. The conductor is interposed between the two HSF cylinders and the 1 mm spacing becomes an area of high molecular bonding between the inner and outer HSF cylinders. The resulting solenoid construct consisting of the YBCO conductor embedded between the inner and outer HSF cylinders is modeled and analyzed for thermal and structural response.

For this analysis, the operational temperature is 50 K, and the critical temperature for the onset of quench is assumed to be 92 K. Coil quench can destroy the conductor and supporting structure because of the amount of energy that is stored in an operational coil before quench. A quench protection system that initiates protection upon the detection of an associated coil response, such as a sudden rise in temperature, is described in Appendix C.

The thermal profile associated with a sudden rise in temperature is characterized by the normal zone propagation velocity (NZPV) and the minimum propagation zone (MPZ). These two quantities (NZPV and MPZ) are evaluated for their sensitivity to changes in substrate and HSF material and the resulting effects on the thermal profile in the YBCO tape. The default material for the tape substrate is Hastelloy®. The substituted substrate material considered for both thermal and structural effects is graphene.

The analytical models use a baseline YBCO conductor model for both the thermal and structural simulations. Figure 11.1 shows this baseline off-the-shelf tape construction. Figure 11.2 shows the corresponding numerical model.

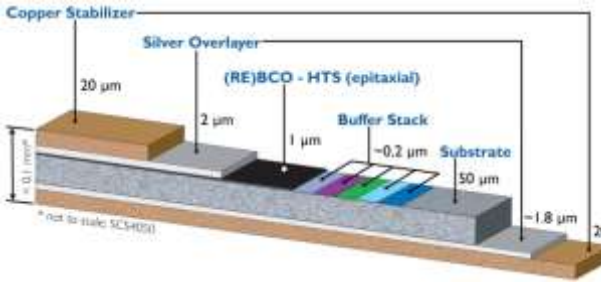

Figure 11.1. Baseline off-the-shelf tape.

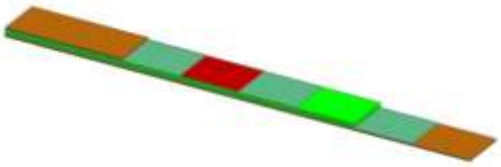

Figure 11.2. Baseline tape numerical model.

The tape-alone model (without HSF support structure) is analyzed for differential thermal stress. Differential thermal stresses are a result of the different coefficient of thermal expansion (CTE) for the tape component materials. The tape-alone model is also analyzed for the stress as a result of structural load.

The structural load for the tape model is developed from the Lorentz force associated with a one tesla (1-T) field. This force is represented as a 4-atmosphere pressure acting in the positive radial direction of the solenoid. The radius of the solenoid is 4 m. Von Mises and shear stress results are developed for the tape cross-section. Comparison analyses are ran for models using graphene as the component material for the overlayer, stabilizer, substrate, and HSF support structure. Contrasting analyses are performed to evaluate the effect of graphene-coupled tape components regarding thermal structural response. Results show the tape-alone stress levels exceed yield levels for all cases where the radial pressure load of 4 atmospheres is applied. Here, the yield stress level and bond strength are developed by tensile tests[11] on total component tape test specimens and are 850 MPa and 160 MPa, respectively. Similar analyses are performed for the tape model embedded in an HSF support structure.

The embedded model is shown in Figure 11.3. The YBCO tape is embedded between HSF cylinders (layers), each 3.175 mm thick.

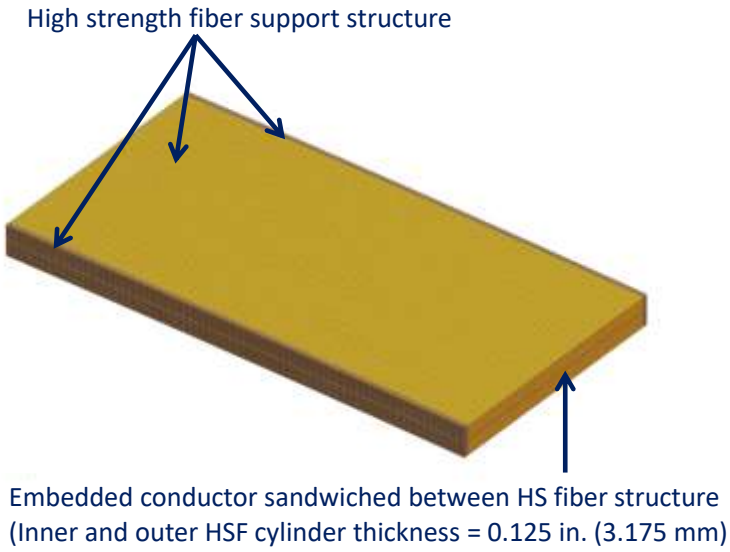

Figure 11.3. Embedded YBCO tape model.

Planar boundary conditions are used at the ends of the 100-mm-long x 52-mm-wide model, which includes 1-mm spacing between windings. Results show that for the all load cases, the stress levels in the tape are below yield. These results indicate the effectiveness of the support structure developed in previous work. The results for the embedded tape model also indicate a stress stability effect associated with using graphene as the material for the substrate. Graphene also exhibits high in-plane thermal conductivity values compared to Hastelloy®.

Analyses are also performed using the embedded model to determine the effect graphene has on the thermal response profiles associated with the NZPV and MPZ. Comparison runs were made between substrates constructed from Hastelloy®, graphene, graphene with a magnitude increase in thermal conductivity (K), and graphene with two orders of magnitude increase in 'K.' Analyses show that a substrate constructed of a material with 'K' of sufficient magnitude can result in steady-state thermal response below quench T-critical, and thereby, offer opportunity by design to enhance quench detection and coil survivability.

Table 11.1 illustrates the effect of graphene on resultant stress levels for the tape in a freely supported condition (free-free) with no load, and for a constrained configuration with a pressure load of 4 atmospheres. In a thermal environment with no pressure, only the stress levels in the tape are below yield. The introduction of graphene for the substrate highlights that graphene has a negative coefficient of thermal expansion, and thus higher resulting stress levels.

Table 11.1. Stress Margin of Safety for YBCO Tape

YBCO TAPE						
Stress Margin of Safety and Associated Structure						
Thermal Only and Thermal with Pressure						
Structure	Material	Loading	Tensile	Shear	Tensile	Shear
Substrate	Hastelloy	Thermal Only	7.5	9.2	Buffer Stack	Buffer / Substrate
Substrate	Graphene	Thermal Only	1.13	1.45	Stabilizer	Substrate / Overlayer
Substrate	Hastelloy	Thermal and Pressure	-0.94	-0.93	Substrate	Substrate / Overlayer
Substrate	Graphene	Thermal and Pressure	-0.94	-0.93	Substrate	Substrate / Overlayer

Table 11.2 illustrates the stress stabilization as a result of two factors. The first factor is the load sharing and tape stabilization as a result of the HSF support structure. The second factor is the use of graphene for a tape stabilizer. Both Tables 11.1 and 11.2 summarize the structural margins of safety using a factor safety of 1. The only viable structural configuration that adequately reacts to the Lorentz forces is the one that embeds the conductor into the HSF support structure.

Table 11.2. Stress Margin of Safety for YBCO Tape Embedded in High-Strength Fiber

YBCO TAPE EMBEDDED IN HIGH STRENGTH FIBER						
Stress Margin of Safety and Associated Structure						
Thermal with Pressure						
Structure	Material	Loading	Tensile	Shear	Tensile	Shear
Substrate	Hastelloy	Thermal and Pressure	2.24	2.36	Substrate	Substrate / Overlayer
Substrate	Graphene	Thermal and Pressure	2.85	2.89	Substrate	Substrate / Overlayer

Table 11.3 summarizes the effect graphene has on the thermal profile associated with rapid local heating simulating a 1.25-mm defect in the YBCO layer. Results show the peak temperature to be reduced by approximately 25% and the propagation zone increased by 220% when parametric design is constrained to the substrate structure alone. When considering constraining parametric design to the HSF support structure for the conductor, the peak temperature is reduced by approximately 72% and the propagation zone is increased by 300%.

Table 11.3. Transient Thermal Response

Transient Thermal Response to 4 ms			
Configuration	$T_{initial}$ (K)	T_{final} (K)	Propagation Zone (mm)
Hastelloy Substrate	50.00	237.00	2.9
Graphene Substrate	50.00	177.00	6.4
Hastelloy Substrate G-Fiber HSF Conductor Support	50.00	65.00	8.7

These analyses indicate both thermal and structural benefits associated with a conductor that integrates graphene into its architecture. While improved structural and thermal performance was achieved by graphene integration with the YBCO tape components, even greater benefit is achieved by similar integration of graphene into the HSF support structure. The results suggest that a design for the YBCO tape and conductor HSF support structure may yield even more performance improvement opportunities. The context of the utility for the conductor, as analyzed here, is that of a 20-m-long solenoid construct with an 8-m diameter. Figure 11.4 shows and end view of such a construct. The concept of operations associated with manufacturing and deployment of such magnet architectures highlights areas needing research:

1. Researching and developing materials at temperatures associated with deep space
2. Using multi-physics analytics
3. Analyzing large-scale structures requiring micro-meter discretization
4. Manufacturing flexible high-strength fiber constructs
5. Coating HSF for enhanced absorptivity, emissivity, and reflectivity
6. Doping HSF for enhanced thermal conductivity
7. Testing methods for verification of analytical models

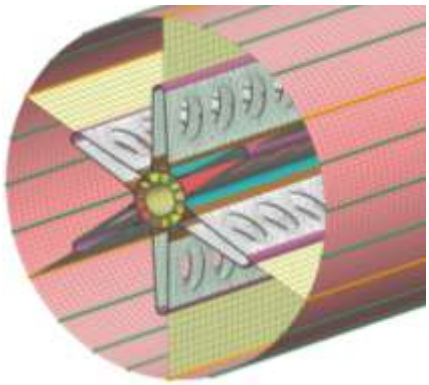

Figure 11.4. Solenoid flexible cylinder, limiter components, a strongback.

12 Spacecraft and Mission Architecture

To design a vehicle durable enough to support a year-long deep-space human mission, the architects must consider certain factors and variables and weigh them against possible risks. This section analyzes three of these factors (mass, trajectory, and propulsion), and discusses trade-offs to be made between different implementations of the Magnet Architectures and Active Radiation Shielding Study (MAARSS) spacecraft.

The MAARSS spacecraft is intended for long-duration, deep-space human missions. As such, an increased food and water supply, propulsion mass vs. mission duration, trajectory analysis, and integrated system sizing need to be examined and defined before a final design team can select the best elements and finalize the MAARSS design.

The Phase II study focused mostly on increasing the capability of the active radiation shielding coil system. To increase the shielding effectiveness, one must increase either the magnetic flux density, or the solenoid dimensions, to increase the path length of the magnetic fields.

12.1 Habitat Mass

The configuration outlined in Table 12.1 replaces the logistics module included in Phase I with a docking/extravehicular activity (EVA) port, which allows the habitat volume to increase, adding 7 metric tons to the Phase I mass.

Table 12.1. Propulsion Study for 6 + 1 Architecture

1 Year Mission	Mass (metric tons)	Purpose and Components
Habitat, 6x10 m cylinder	32	Crew volume, integrated systems, consumables
Compensator coil	3	Compensated for protective magnetic field
8 T·m, 6 coil system	50	Coils, structure, blanket, 35% contingency
Docking/EVA port	5	Tunnel with CM, SM docking port
Multi-Purpose Crew Vehicle	10	Crew module for crew transport to spacecraft and return home
Service Module	6	For crew delivery and de-orbit burn, dry mass
Total	**106**	**metric tonnes**

12.2 Trajectory Analysis – Cycler Orbit

Considering the conceptual use of the MAARSS spacecraft, it is logical that a deep-space cycler orbit would be a useful approach for an active shield architecture. Such an approach would be useable for multiple missions, which would reduce architecture cost.

A single-target destination was selected for study based on low delta V, as opposed to shortest flight duration. Because radiation protection is available, shortest flight duration is no longer the driving factor. The objective is to select a mission that approaches a 1-year round trip including an 8-day stay. With these criteria, the destination considered is the near-Earth asteroid (NEA): 2000 SG344, with a conceived mission duration shorter than 1 year.

In the Phase I effort, chemical and electric propulsion systems were compared, focusing on propellant mass, flight duration, passive radiation protection, and delta V output. For the present study, a liquid oxygen/hydrogen (LOX/H2) chemical propulsion with an I_{sp} of 400 seconds is assumed and compared to an electric propulsion system, with an I_{sp} between 2000 and 5000 seconds, power of 0.4-1 MW, and an efficiency of 60%.

In the following scenario, depicted in Figure 12.1, the chemical propulsion system is used to travel between the NEA and back to Earth. The blue orbit represents the spacecraft in an orbit around the Earth as it orbits the Sun, and the green represents the NEA orbit. The flight duration of the entire mission using this propulsion system is approximately 365 days.

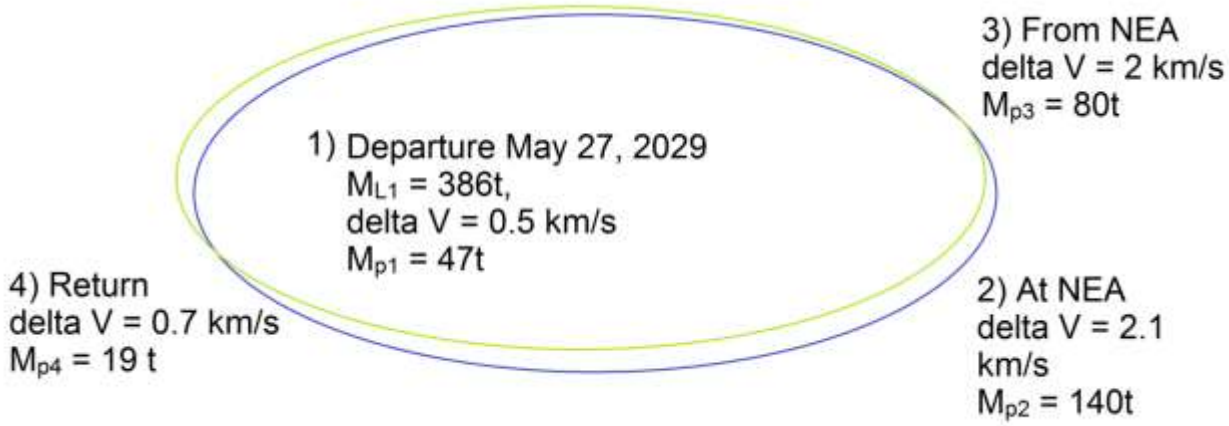

Figure 12.1. Cycler trajectory analysis using chemical propulsion.

Figure 12.2 shows the trajectory using an electrical propulsion system described above. Thirty-five days after departure from Earth orbit, the spacecraft will perform Earth-Sun Orbital Injection (ESOI), requiring a propellant mass of 1 tonne. The spacecraft will arrive at the NEA after 127 days, leaving 8 days later. The trajectory requires more orbital maneuvers, but the flight time is 340 days, which is shorter than using chemical propulsion (365 days).

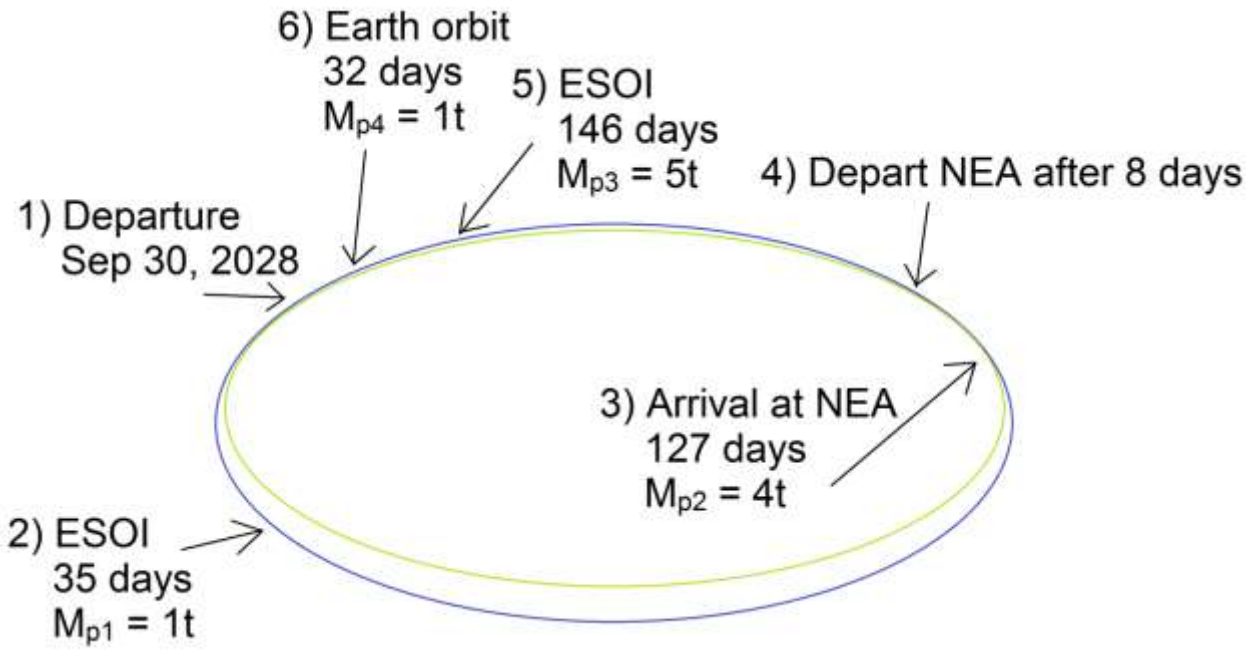

Figure 12.2. Cycler trajectory analysis using electric propulsion.

12.3 Propulsion Mass Considerations

. An electric propulsion system, with an assumed specific impulse, I_{sp}, of 5000 seconds using argon is assumed and compared with an LH2/LOX chemical propulsion system, with an I_{sp} of 400 seconds.

The electric propulsion system was studied because of an assumed decrease in required propellant mass, and because this system would provide minimum passive shielding contribution on the endcap of the MAARSS spacecraft. Similarly, the chemical propulsion system, while representing a significant mass, also presents a significant passive shielding contribution using hydrogen, which is a sufficient radiation shield, in the propellant.

Considering the trajectory analysis presented in Section 12.2, the parametric analysis (Figure 12.3) was made. The mission duration, specific impulse, initial mass, and power of the electric propulsion system are compared with the chemical propulsion approach.

The findings indicate that a baseline electric propulsion mission takes 22 times less propellant than a chemical mission. Using a propellant with an I_{sp} of 2000 seconds reduces mission travel time by 2 to 3 months; however, this system requires 4 times as much propellant as the 5000 seconds I_{sp} option. Additionally, each increase of power by 200 kW reduces the flight duration by 1 month, while increasing the spacecraft mass by ~23 tonnes.

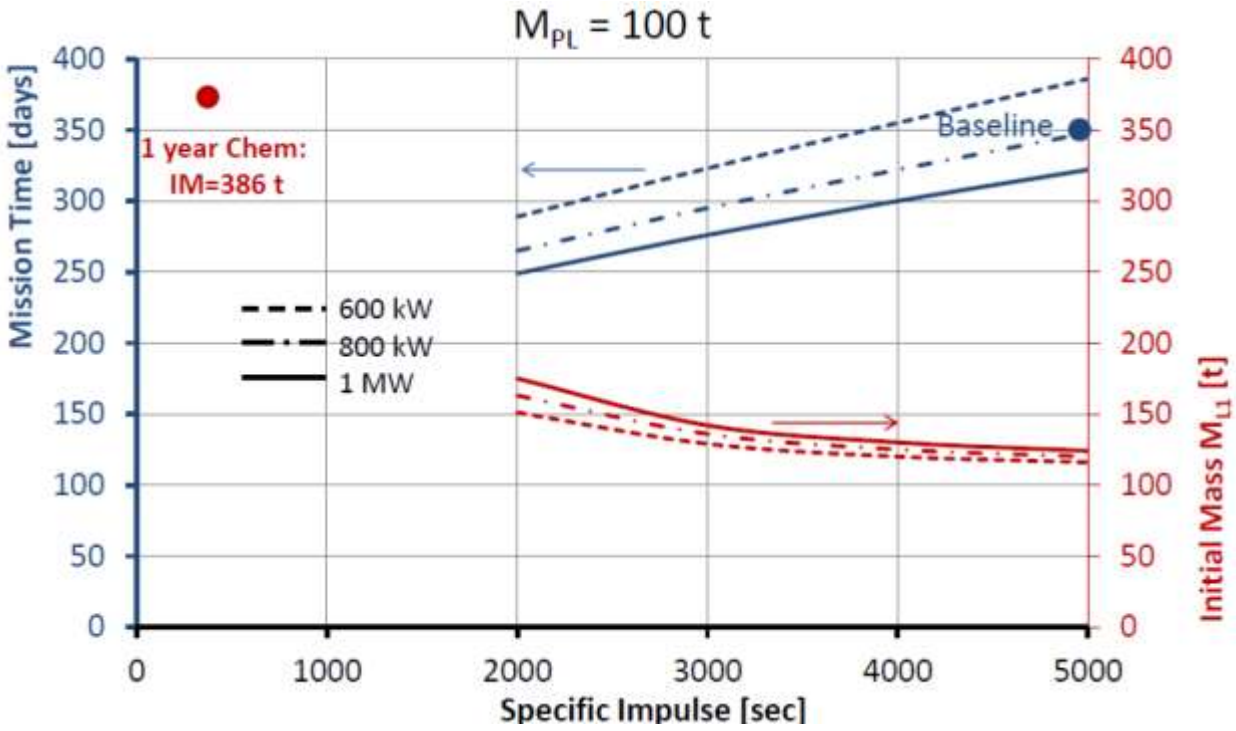

Figure 12.3. Parametric analysis for NEA roundtrip.

The electric propulsion system has great potential for reducing propellant mass requirements, and the input power to the system can design and control the flight duration.

12.4 Integrated System Sizing

After considering the trade-offs and parametric analyses discussed in Sections 12.2 and 12.3, two options are presented for an integrated spacecraft. The spacecraft illustrated in Figure 12.4 uses chemical propulsion and features two main propellant tanks for H_2 and O_2. The mass of the propellant for the NEA mission is estimated to be 286 tonnes, with an initial spacecraft mass of 386 tonnes, requiring a total delta V of 5.3 km/s.

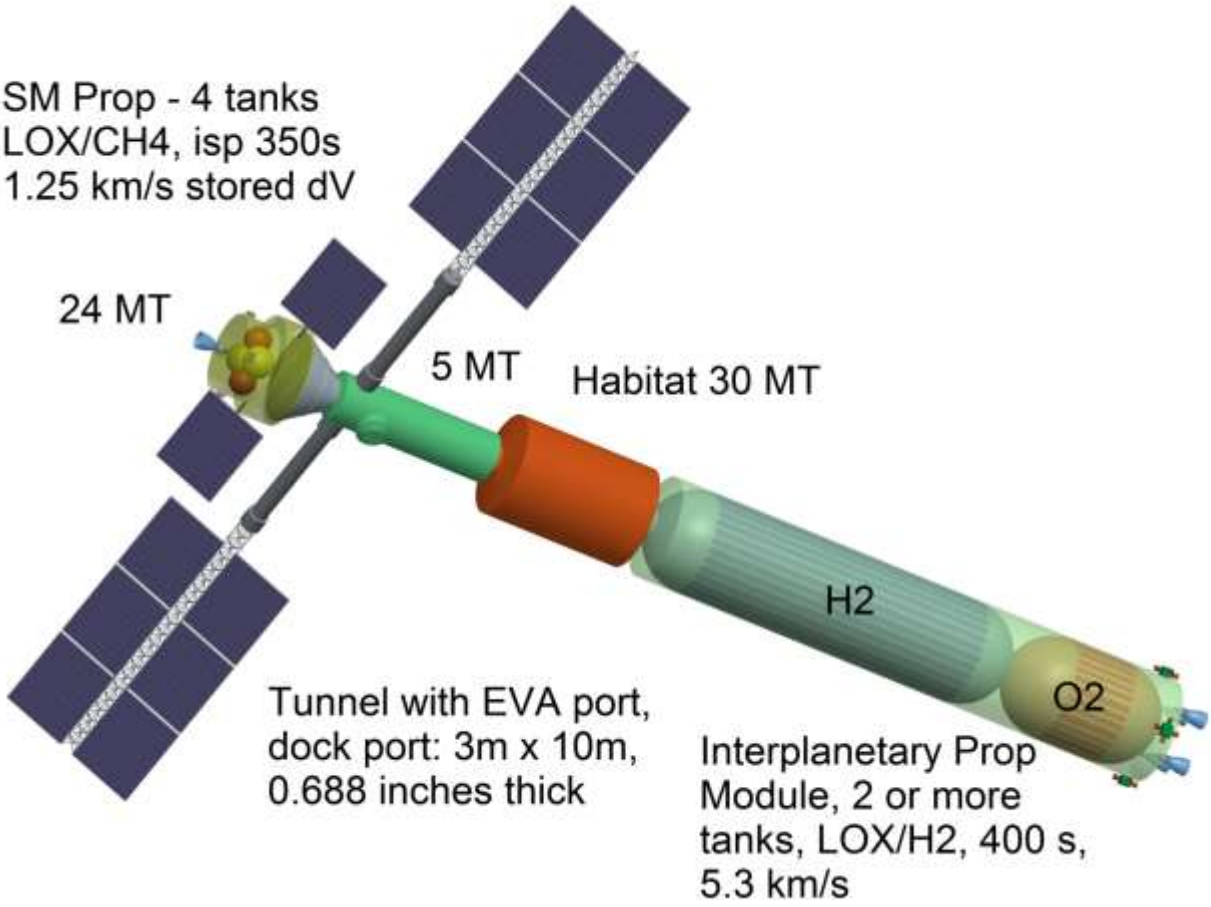

Figure 12.4. Integrated system sizing using chemical propulsion.

The spacecraft illustrated in Figure 12.5 uses an electric propulsion system with 12 megatonnes of Argon propellant. The initial spacecraft mass is 120 tonnes, with a total delta V of 5.2 km/s. Neither the compensation coils nor the six superconducting coils are shown for either configuration. The 6 + 1 coil configuration has a mass approximating 53 tonnes, independent of the choice of propulsion system.

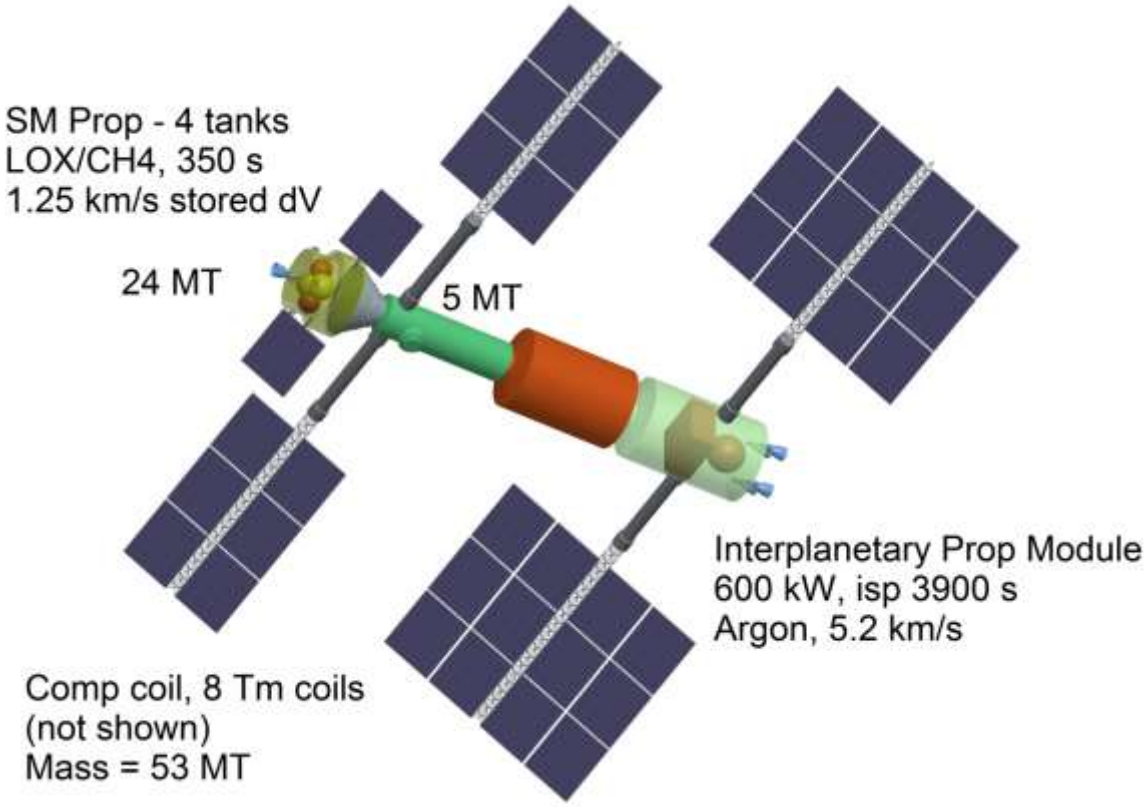

Figure 12.5. Integrated system sizing using electric propulsion.

From these analyses, an electric propulsion system is favored because it reduces the propellant and initial spacecraft mass and flight duration. However, an electric propulsion system requires a great deal of power (> 600 kW), which may be constrained on such a mission. The high-temperature superconducting coils will require much energy to ramp to charge, but once magnetized, their power requirement will be decreased. This suggests that one approach would be to ramp the coils to charge, and then use the remaining power for the propulsion and other systems.

Launch and orbital insertion of the spacecraft deserve more detailed consideration. The implementation of the MAARSS spacecraft currently consists of lifting the shielding coils, compensation coil, and habitat to high-Earth orbit (HEO) before docking and deployment. The propulsion system chosen will greatly affect the orbital trajectory and may have one other significant consequence. While an electric propulsion system can deliver the spacecraft components to HEO, it does so slowly, with an increased exposure to the trapped particles of the Van Allen radiation belts. Such exposure may have detrimental effects on the spacecraft and its systems. Therefore, while an electric propulsion system seems more efficient for the transit to and from a NEA, it poses challenges in HEO orbital insertion. These issues must be investigated in radiation particle analyses, and the risk to the spacecraft must be defined and mitigated before the final spacecraft design is selected.

13 Simulation Results for the Extendable Solenoid Shield (Solenoid Array) Configuration

See Appendix D for the complete report.

The solenoid array by itself does not protect the habitat inside it from particles coming from directions close to the axis of the array, since the field is low there and particles from those directions will not have their paths bent much. It is possible that structural, fuel, or cargo modules placed along the axis could improve radiation shielding by intercepting these particles. Figure 13.1 below shows a spacecraft geometry that was examined.

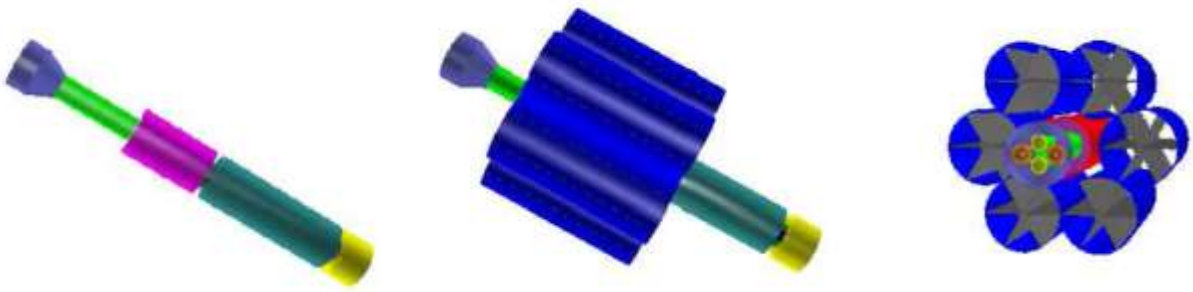

Figure 13.1. NEA spacecraft geometry (configuration).

The spacecraft geometry studied in the extendable solenoid shield configuration simulation does not significantly affect the dose levels when considering radiation from all possible directions including the barrel and end-cap regions (full acceptance). The dose reduction produced by the modules aligned along the axis of the habitat, for example, at the position of cylinder 6 on right in Figure 13.3, is compensated by a dose increase as a result of secondaries created in the spacecraft structure, which enter the field region and are deflected back toward the habitat (Figure 13.3). Figure 13.3 shows that the deflection of primary and secondary particles in the direction of the habitat is visible in the xy (left) and xz (right) projections. The generation of secondaries in the liquid-hydrogen container of the propulsion system is visible in the xz projection. To reduce the contribution of particles reflected into the habitat, the distribution of mass in the endcap regions should be extended to close the magnetic field region.

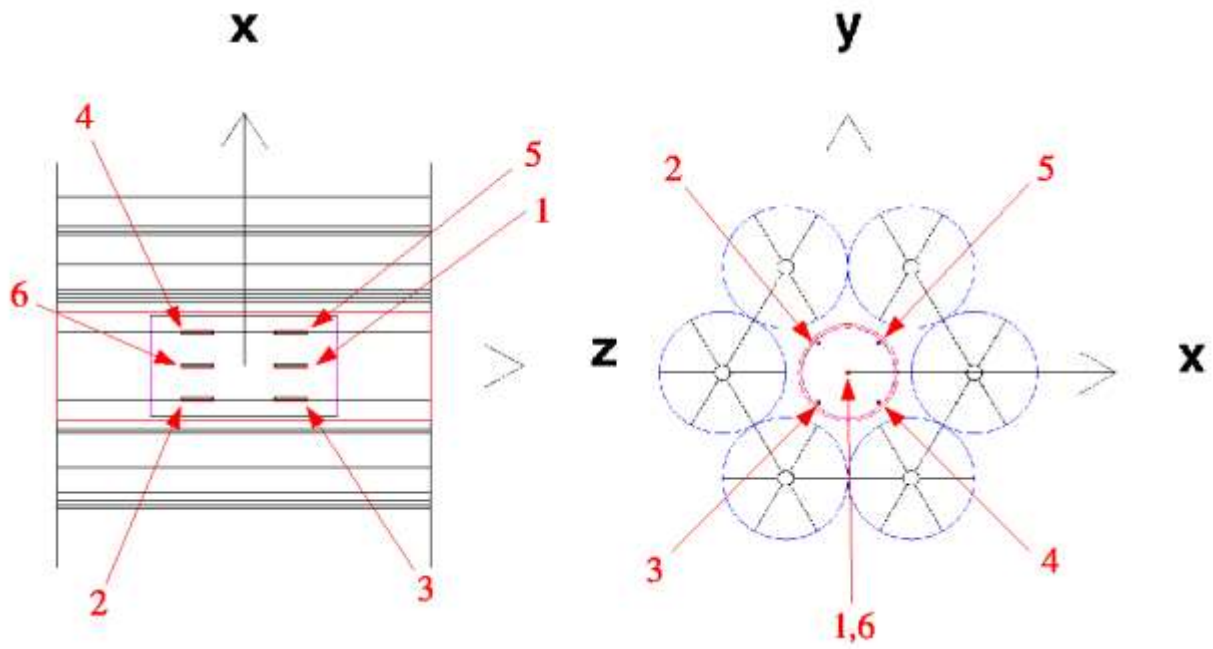

Figure 13.2. The location of the six water cylinders in the habitat.

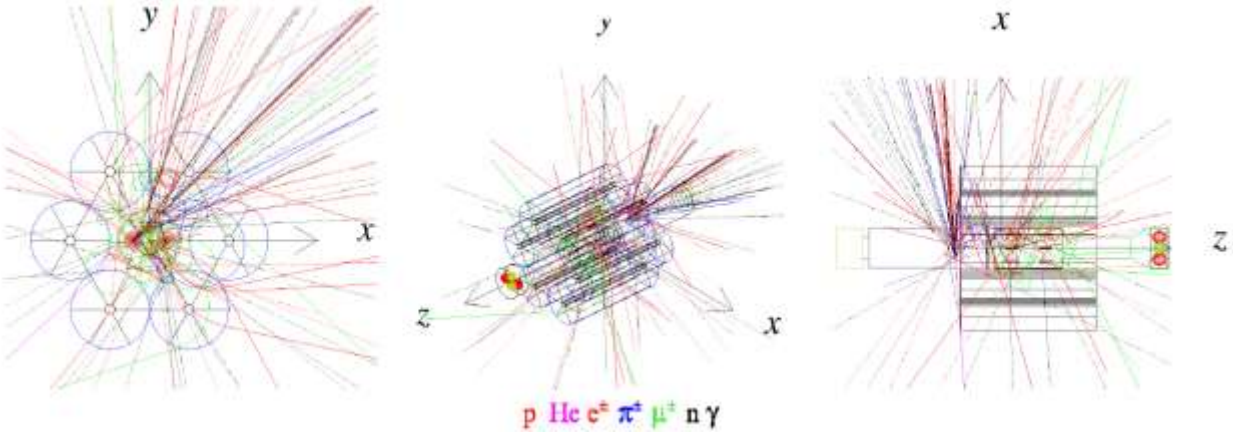

Figure 13.3. Simulated events in which a GCR proton or He nuclei generated in the barrel region resulted in an ionization energy loss in the water cylinders.

The fringe field of the 6 + 1 shield solenoid (Figure 13.4) does not increase the shielding efficiency in the endcap regions. Where lower energy solar energetic particle (SEP) protons exist, the shielding efficiency increased 15 to 20% in the blood-forming organ (BFO) and body dose equivalents with the presence of the fringe field. No significant effect is expected for the higher energy GCR.

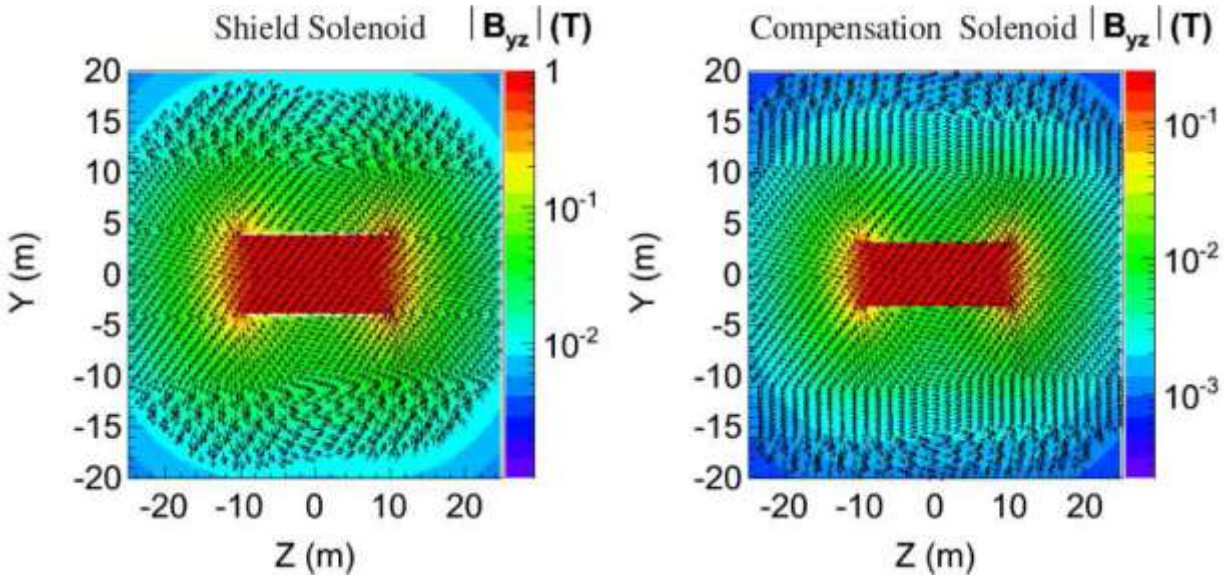

Figure 13.4. Field maps.

The increase of the habitat wall thickness from 18 to 40 mm results in a decrease of the GCR free-space dose levels by 20% (Table 13.1). The mass of the Phase II habitat in the simulation, including the provisions for food and water, is a factor of 3.5 larger than the Phase I habitat.

Table 13.1. Annual GCR Dose Equivalents (cSv/rem) at Solar Minimum, for the Phase I and II Habitats

	Phase I Habitat			Phase II Habitat		
Z	skin	BFO	body	skin	BFO	body
1	13.1±0.4	12.3±0.2	12.3±0.2	15.2±0.5	14.0±0.4	13.8±0.3
2	6.3±0.3	5.5±0.3	5.4±0.1	6.9±0.7	5.7±0.2	5.8±0.2
3-10	25.7±1.3	16.5±1.1	8.4±0.4	16.8±2.1	11.3±1.0	5.8±0.6
11-20	22.1±1.3	10.6±0.6	8.9±0.5	12.9±1.8	6.8±1.0	5.2±0.7
21-28	11.0±1.6	3.6±0.8	3.8±0.6	5.1±1.1	1.8±0.4	1.7±0.3
total	78.2±2.1	48.5±1.5	38.8±0.9	56.9±3.1	39.6±1.5	32.3±1.0
fraction of Phase I Habitat dose				0.73±0.04	0.82±0.04	0.83±0.03

The dose equivalent levels of the 6 + 1 solenoid shield configuration were compared with and without the 8 T·m field. The presence of the field results in a » 5% reduction of the doses provided by the habitat's passive shielding, and the solenoids' coils and support structures. To reduce the inter-coil forces, a 50-cm gap between adjacent shield solenoids would reduce the shielding efficiency by about 5%.

A plane geometry was used to determine the flux reduction over a limited acceptance (particles coming in from a limited range of angles). The approach allows a straightforward evaluation of the roles played by the active and passive elements of the shield configuration. The method reveals the contribution to the dose of low-energy primary protons, which scatter in the coils and are deflected into the habitat

(Figures 13.5 and 13.6). The protons pass by the inter-coil regions, lose energy in the material of the coils and support structure, and are deflected by the field toward the habitat.

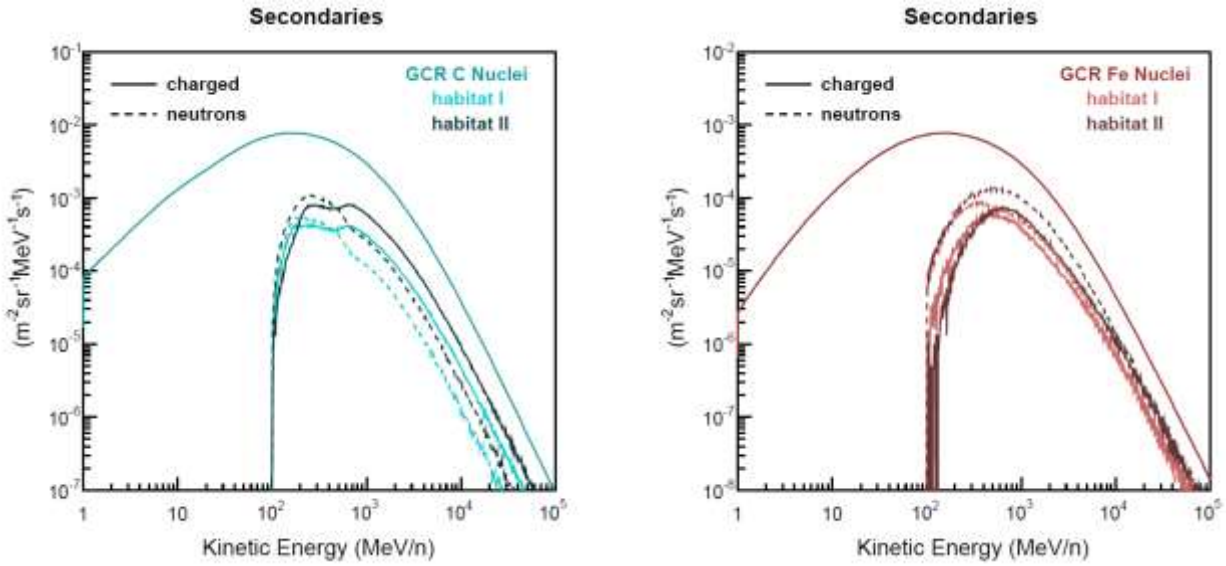

Figure 13.5. The fluxes of the GCR carbon and iron nuclei, which create secondary charged particles and neutrons that enter the Phase I and II habitats.

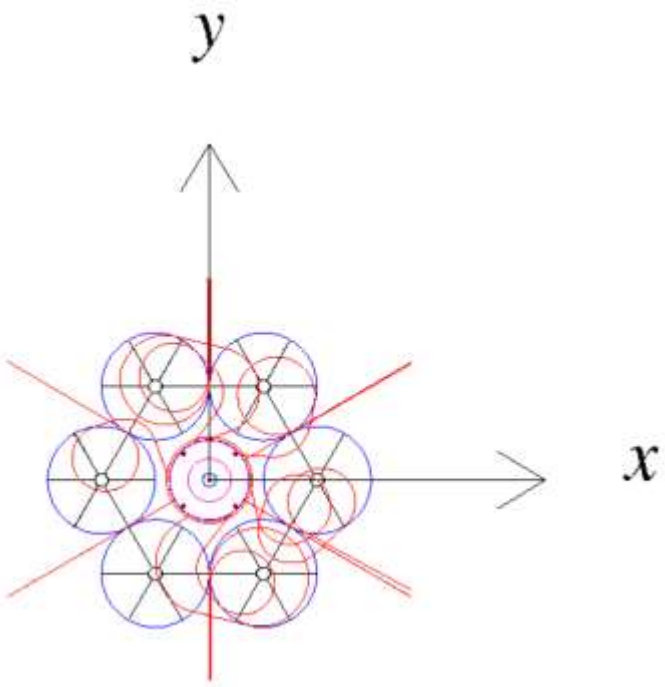

Figure 13.6. Plane geometry simulation showing the GCR protons with kinetic energies below 800 MeV, which enter the habitat.

Note that the particles are tracked until they enter the habitat.

The example illustrates how the material of the magnetic shield modifies the relation between the bending power (BL) of the magnetic field and dose reduction.

The free-space dose equivalents and absorbed doses were presented to argue in favor of the dose equivalent, or other dose definitions that consider the biological damage. It is misleading to present the performance of a shielding configuration for crewed spacecraft in terms of absorbed dose.

Geant3 is the name of a set of software developed at CERN for calculating the path of elementary particles through matter. When Geant3 was rewritten in C++, it was renamed Geant4.

The Geant3 and Geant4 free-space doses were compared. The Geant4 simulation uses the same generation and dose sampling techniques employed in the Geant3 program. The most significant difference was observed for the GCR $Z > 2$ nuclei. The contribution of secondaries is significantly more important in Geant4 (30-40%) than in Geant3 (10%), where the ionization of the primary nuclei dominates.

The larger contributions of secondaries may be expected, since recent advances in the modeling of the interactions of the high charge nuclei are incorporated in the Geant4 framework. The modeling of proton and He nuclei hadronic interactions was well developed at the time of Geant3.

The most significant result of the simulation comparison, for the conclusions drawn in the NIAC studies based on Geant3, is the smaller contribution of the Z > 2 nuclei to the BFO dose equivalent, 60% compared to the Geant3 value of 73%. The body dose equivalents are compatible, and the difference observed in skin dose equivalents is not critical since this dose is easily reduced by the passive shielding of the spacecraft.

The 13% difference associated with the BFO dose estimation is not likely to change drastically the conclusions of the present study. The 6 + 1 solenoid shield configuration has been implemented in the Geant4 simulation; the field-on, field-off comparison should be redone to confirm the previous statement.

The Geant4 results indicate that the free-space BFO dose equivalent is 25% lower than the value cited in Reference 12.

The Monte Carlo statistics are summarized in Table 13.2. The GCR nuclei were generated according to their relative abundance (e.g., the ratio proton-to-helium is 10:1 in the quoted event statistics). A sample of 50 M GCR protons and He nuclei generated with the 6 + 1 solenoid shield configuration require » 24 hours, while 50 M GCR Z > 2 nuclei require 5 to 7 days.

Table 13.2. Monte Carlo Statistics of Phase II Study

configuration	type	particle	events (M)
NEA chemical prop.	GCR	p, He	700
NEA chemical prop.	GCR	3 · Z · 28	365
Phase I habitat	GCR	p, He	500
Phase I habitat	GCR	3 · Z · 28	150
Phase II habitat	GCR	p, He	300
Phase II habitat	GCR	3 · Z · 28	275
6 + 1 shield no field	GCR	p, He	500
6 + 1 shield no field	GCR	3 · Z · 28	205
6 + 1 shield field	GCR	p, He	500
6 + 1 shield field	GCR	3 · Z · 28	330
6 + 1 shield 50 cm gap	GCR	p, He	300
6 + 1 shield 50 cm gap	GCR	3 · Z · 28	100
6 + 1 shield field SEP p 200	SEP	p	200
6 + 1 shield fringe field SEP p 200	SEP	p	200
free space	GCR	p, He	50
free space	GCR	3 · Z · 28	50
Geant4 free space	GCR	p, He	50
Geant4 free space	GCR	3 · Z · 28	10

14 Thermal Design Concept

This section outlines the thermal requirements of the superconducting magnets for the NIAC study of a spacecraft's active magnetic shielding system. This document builds on the Phase I study, focusing on the environmental thermal loads and developing the passive and active thermal control systems.

The spacecraft's active shielding system consists of a 6 + 1 design with six identically sized coils surrounding one compensation coil and habitat. The superconducting coils must be cooled to a low temperature before magnetizing the system and during operation.

The conceptual design of the magnetic shielding system has several predetermined assumptions that have not changed since the Phase I study:[13]

1. The superconducting magnets are to be made with HTS material and operate below 40 K.
2. The coils will not be contained within their own vacuum chamber, but will rely on ambient space vacuum and radiation shielding for thermal insulation. Any coil vacuum chamber suitable for atmospheric pressure on Earth is deemed too heavy to be launched.
3. The coils must be launched warm (T ~ 300 K), since they will not be thermally insulated in space and in their final configuration, This establishes magnet cool-down requirements on the cryogenic system, which could easily determine the size of the system. This cool-down requirement also precludes the use of storable cryogens as a primary cooling source.
4. The coils will need to be actively powered to maintain a constant magnetic field. Any coil-powering system will have an associated thermal load.
5. The thermal control system must be capable of cooling down the coil assembly and removing the following stead-state heat loads:
    a. Thermal radiation from other sources (Sun, Earth, and crew module).
    b. Resistive loads in the coils as a result of joints of index losses in the superconductor.
    c. Alternating current (AC) losses as a result of charging the magnets.

This study assumed that the active radiation shielding system will be launched from Earth, assembled in LEO, transferred to HEO (altitude > 65,000 km), where the coils will be cooled, magnetized, and deployed.

Figure 14.1 shows the reference dimensions for the 6 + 1 coil system.[13] The Phase I study defined these dimensions. Because further work has been done in Phase II that suggests the benefits of other dimensions, the thermal design concept presented here is scalable to any predefined dimensions.

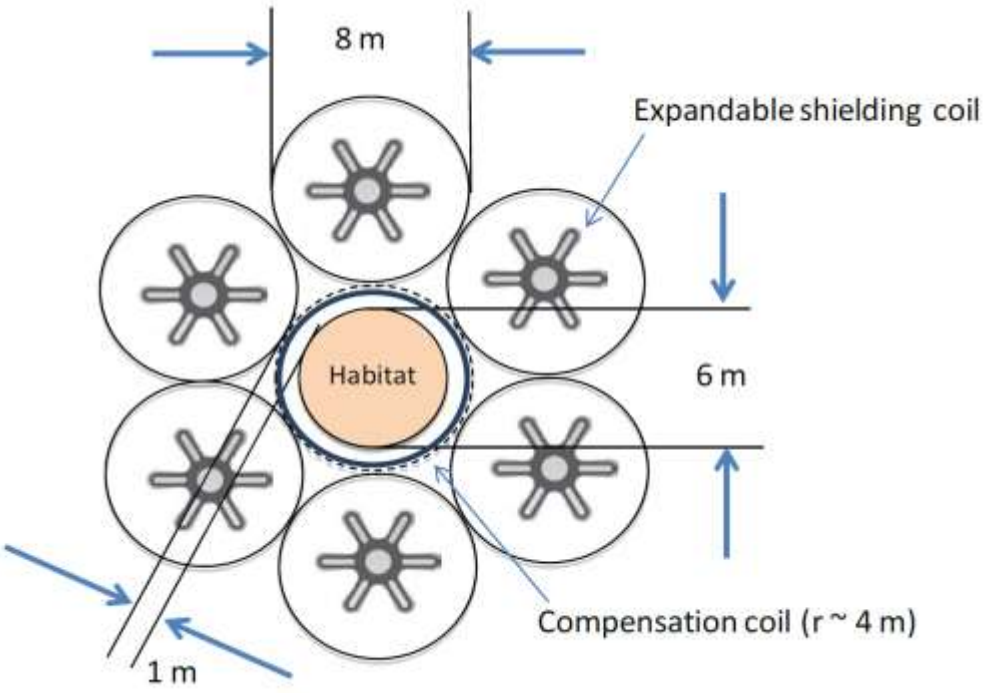

Figure 14.1. Shielding Coil Configuration.

While the Phase I study recommended cryocoolers as the main source of cooling, this section's analysis of the environmental thermal loads and the current capability of cryocoolers suggests that cryocoolers alone will not be sufficient to meet the system's cooling requirements. Therefore, much of this section has been dedicated to developing passive thermal control systems to support or even replace the active thermal control.

14.1 Cool-down Requirements

The superconducting coils must be cooled to a temperature below 40 K before operation. The cool-down requirement is driven by the cold mass of the superconducting coil system, which is estimated to be 7.5 tons/coil of the six shielding coils. This is based on the total mass of the superconductor, the backbone that supports the flexible coils, and the structural mat that is planned to support the electromagnetic loads. The analysis in this section is based on the assumption that the compensation coils do not contribute significantly to the total mass. This mass does not include that of the cooling system.

As reviewed in the Phase I study, the cool-down enthalpy of each 7500 kg coil from 300 K to 40 K is estimated to be 1275 MJ, assuming the thermal properties of the coils are similar to that of aluminum. In the Phase I study, it was assumed that this cool-down can be facilitated by a combination of radiation heat exchange to deep-space and active-cooling cryocoolers.

For the radiation cooling to deep space to be effective, to bring the coils to operating temperature, the coil system should be thermally shielded from other sources. If the coils were radiating only to deep space, the cooling from 300 K to 40 K should take ~75 days assuming an emissivity of 0.5. However, upon further consideration, the operating temperature of the coils is required to be between 25 and 30 K. This was driven by the need to protect the system from quenching. Such an event would not only render the system inoperable, but could result in disaster for the spacecraft and crew. Therefore, the cool-down temperature required is 30 K, which necessitates more time and cool-down enthalpy than described above.

The Phase I study investigated the use of a sunshield to thermally protect the coils. That study assumed that if the coils were located behind a sunshield at a nominal 170 K with a low emissivity back surface, the coils could achieve a minimum temperature of 70 to 100 K. This led to the assumption that radiation cooling would not supply enough cooling to achieve the required operating temperature or to remove the steady heat load during operating. Additionally, the habitat heat load cannot be easily radiated to deep space because it is surrounded by the compensation coil.

Further review of sunshield technology revealed a greater possibility of thermally insulating the coils. The James Webb Space Telescope (JWST), currently under development, will use a sunshield to cool its instrumentation to 40 K. While the solar thermal load (the driving external heat source) differs greatly between the JWST's orbit of the Earth-Sun L2 Lagrange point and the HEO where the solenoid array will cool down, the technology is being developed and will provide more cooling than originally assumed.

14.2 Thermal Loads

14.2.1 Solar

The solar heat flux is the largest external source of thermal loading on the system. The flux, which is proportional to the distance from the Sun, has an average value of 1367 W/m^2, ranging between 1322 and 1371 W/m^2. This section assumes that the spacecraft will travel farther from the Sun than Earth orbit, toward an NEA or possibly Mars, and that the greatest solar thermal load will occur in Earth orbit after launch, and upon return. Therefore, the solar flux is assumed to have a maximum constant value of 1371 W/m^2.[14]

Considering the dimensions of the coils from the Phase I study, there are two extreme cases of spacecraft configuration. The first involves a leading or trailing face pointed at the Sun, representing a projected hexagonal area as seen in Figure 14.2. The second case features a side-facing view that projects a rectangular area as seen in Figure 14.3.

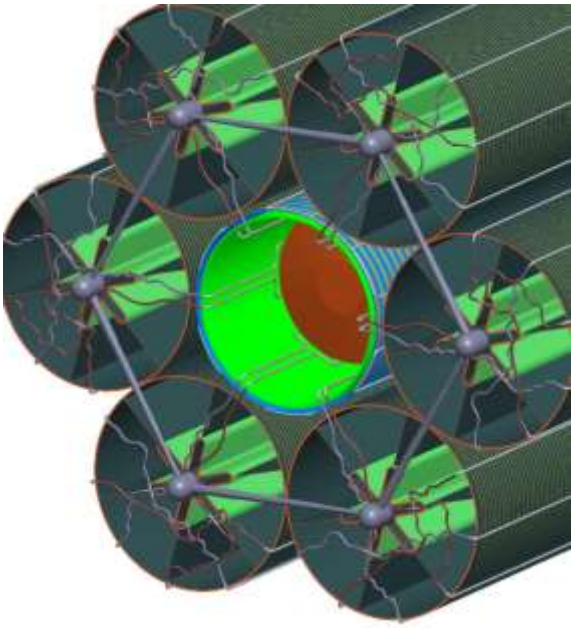

Figure 14.2. Hexagonal front/tail face of the 6 + 1 coil system.

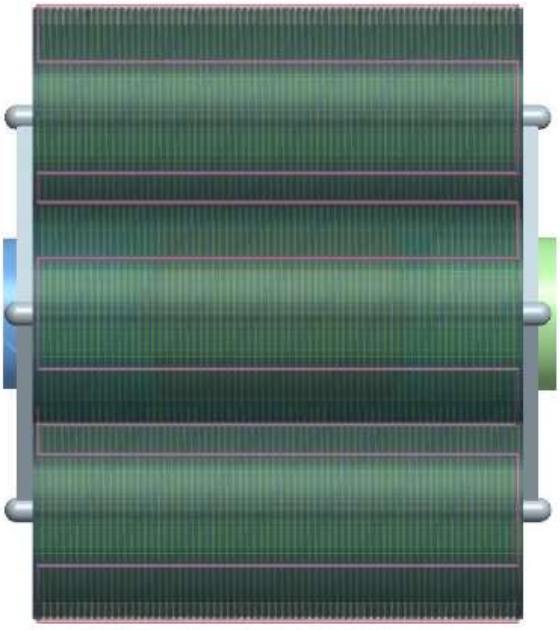

Figure 14.3. Rectangular side face of the 6 + 1 coil system.

In the first case, the hexagonal area is 665.11 m^2, which would therefore be subject to a maximum of 912 kW, assuming an absorptivity of 1 on the surface. In the second case, the rectangular area is 480 m^2,

subject to a maximum of 658 kW. A third case exists where the spacecraft is angled between the first and second cases, but this would result in a larger solar thermal load than either of the aforementioned cases and should be avoided to minimize the solar thermal load.

14.2.2 Earth and Moon

The Earth and Moon radiate heat into space via reflecting incoming solar flux (albedo), and the retransmission of heat via infrared radiation. However, the contribution of each of these sources decreases as the altitude above the source increases. As the spacecraft will begin cooling in HEO, the contributions of Earth and Moon infrared and albedo are deemed to be so small as to be incorporated into any uncertainty of the solar flux.[15]

14.2.3 Habitat

The heat load from the habitat was a major focus of study in Phase I. While the coils must be kept extremely cool, the habitat must be heated to an approximate value of 300 K to support the crew. The space between the habitat and the compensation coil (40 K) is to be shielded with multilayer insulation with an average heat flux of 1 W/m^2. This results in a total thermal load of 380 W on the compensation coil, which should not be exposed to the coils.

14.2.4 AC Losses as a Result of Charging the Coils

The Phase I study estimated that the ramping hysteresis losses for YCBO tape (multiple 50 mm wide and ~0.2 mm thick tapes in parallel), based on the operating current of 40 kA, to be approximately 60 kJ. If the coils were ramped to field in 24 hours, this corresponds to an added heat load of 0.7 W/coil.

14.2.5 Resistive Loads in the Coils

Although the resistive load in the coils because of joints of index losses in the superconductor was an issue in the Phase I study, it has not been investigated at this time, and should be the focus of future study.

14.3 Passive Thermal Control

14.3.1 Surface Treatment

The first passive thermal technique investigated is the surface treatment of the structural mat that houses and protects the coils.

The following two equations are essential to understanding the equilibrium temperature and resultant external thermal load of the system.[16]

$$T_{eq} = \left(\frac{\frac{a}{e} * S * \frac{A_p}{A}}{\sigma} \right)^{1/4}$$

$$Q_{ext} = A * a * S$$

With T_{eq} = the equilibrium temperature

a = absorptivity

e = emissivity

S = solar flux, ~1371 W/m^2

A_p/A = projected area/area, 0.25 for a sphere

σ is the Stefan-Boltzmann constant (5.67 x 108 W/m^2K^4)

Q_{ext} = external thermal load

A = area of exposed surface, assumed to be 480 m^2

As shown in Table 14.1,[16] none of the surface treatments have an equilibrium temperature below 180 K. Therefore, surface treatment alone cannot satisfy the cooling requirements of this system.

Table 14.1. Surface Treatment Properties and Considerations

Surface Treatment	Absorptivity	Emissivity	Equilibrium Temperature (K)	External Thermal Load (kW)
MAARSS Phase I Assumptions	0.5	0.5	283	329
Aluminized Kapton (1/2 mm)	0.34	0.55	251	224
Aluminized Kapton (1 mm)	0.38	0.67	246	250
Aluminized Kapton (2 mm)	0.41	0.75	243	270
Aluminized Kapton (5 mm)	0.46	0.86	242	303
Vapour Deposited Aluminum	0.13	0.04	380	85
Anodised Aluminum	0.25	0.88	207	165
Z93 White Paint	0.17	0.92	186	112

14.3.2 Heat Shield

The JWST is required to be cooled below 40 K to block the thermal noise from the Sun, allowing the instrumentation to investigate deep-space, infrared phenomena. This requirement, and the development of the telescope's heat shield, may be usable with the 6 + 1 coil system. This technology is investigated here, comparing the cooling potential and the issues of configuration and interaction with other spacecraft systems.[17]

The first consideration is the photovoltaic solar array system. The heat shield is intended to block the thermal load, mostly dominated by the Sun, but not to obstruct power generation via the solar arrays. The obvious solution is to place the solar panels between the Sun and the heat shield, allowing the solar panels to work normally, and also to block some of the incoming heat load.

While the back-emissive temperature of the solar panels is subject to the insulation used, and said insulation is subject to its effect on the panel performance, the temperature is assumed to be 300 K. This value has been verified on various designs and is considered to be a reasonable value.

Because the size and location of the solar arrays were not set in the Phase I study, the panels designed here were to be placed at the tail end of the spacecraft, and sized to block much of the hexagonal area of the 6 + 1 coil system **(**Figure 14.4**)**.

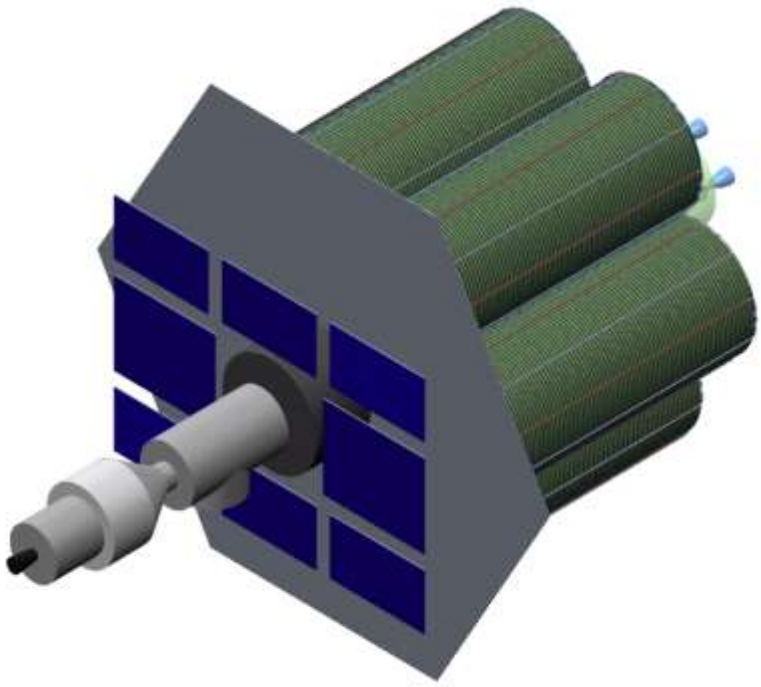

Figure 14.4. Heat shield and solar panel placement.

The heat shield was then sized to shade the coils. This configuration features the solar panels and heat shield to be deployed from the logistics module, thereby driving the pointing requirement of the spacecraft.

For the heat shield to work most effectively, it must stand between the Sun and the coils. Since deployment seems best suited to be based from the logistics module, and not from the coils, the spacecraft will then be required to point the tail end, the hexagonal area, toward the Sun.

Assuming a pointing accuracy of 5°, the minimum width of the heat shield necessary to overcome any possible solar exposure can be determined (Figure 14.5).

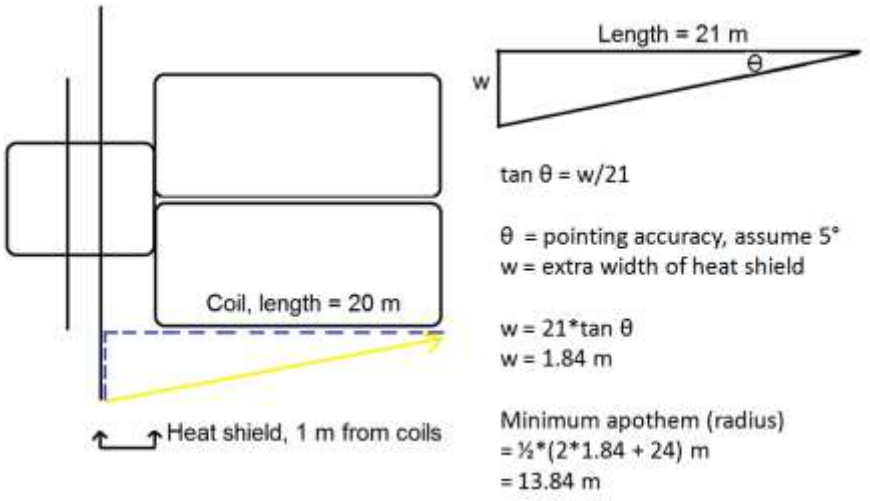

Figure 14.5. Sizing the minimum width of the heat shield.

This sizing consideration is dependent on the pointing accuracy and the dimensions of the 6 + 1 coil system. As such, it is subject to those dimensions and is scalable.

The thermal insulating performance of a heat shield, or any spacecraft thermal insulation material, is determined by the emissivity, e*. This parameter is determined by the quality and number of layers of the heat shield design. To facilitate a parametric analysis, the values of 0.01 is assumed for a single insulation layer, 0.002 for multiplayer insulation, and 0.000001 for a heat shield of JWST quality.

Considering the configuration seen in Figure 14.5, the thermal load on the coils can be calculated:

$$Q = F_{12} * A_1 * e^* * \sigma * (T_1^4 - T_2^4)$$

Where F_{12} = the view factor between the solar array and heat shield, assumed to be 1 here

A_1 = the area of the entire solar array system

e* = 0.01, 0.002, or 0.000001

T_1 = 300 K, the back-surface temperature of the solar arrays

T_2 = 30 K, the desired temperature on the surface of the coils.

The thermal load on the coils is then calculated to be 2836.08 W, 567.22 W, or 0.28 W, depending on the heat shield emissivity.

Considering the radiating power of the coils, at 30 K, as seen in Table 14.1, the remaining thermal load to be removed is seen in Table 14.2.

Table 14.2. Thermal Loads on the 6 + 1 Coil System

Surface Treatment	Thermal Load (W) with Different Heat Shields		
	Single Layer	Multilayer Insulation	JWST Quality
MAARSS Phase I Assumptions	2794.54	525.67	-41.26
Aluminized Kapton (1/2 mm)	2790.38	521.52	-45.41
Aluminized Kapton (1 mm)	2780.41	511.55	-55.38
Aluminized Kapton (2 mm)	2773.77	504.90	-62.03
Aluminized Kapton (5 mm)	2764.63	495.77	-71.17
Vapour Deposited Aluminum	2832.76	563.89	-3.04
Anodised Aluminum	2762.67	494.10	-72.83
Z93 White Paint	2759.64	490.78	-76.15

The negative values seen in the last column of Table 14.2 result from the surface treatment of the coils radiating more heat than they are absorbing from the environment. Note that these values represent the external thermal load on the coils, not considering the habitat heat leak, 380 W.

The Phase I study concluded that cryocoolers, with flexible, low-pressure helium gas circulation loops driven by low-pressure head helium fans, would be used to actively cool the coils. However, considering heat shield technology, Table 14.2 shows that it is possible to cool the coils from the external heat sources, and it is even possible to provide a margin of cooling as seen with the JWST heat shield design.

Further work must be done to consider the mass and cost of heat shield deployment to compare it to the use and development of active systems. Currently, the deployment of flexible helium gas lines on the expanding superconducting wire system seems far less developed and reliable than heat shield technology. Therefore, it is recommended to completely cool the coils from the external environment using a JWST-type heat shield.

14.3.3 Passive Thermal Design Recommendations

After considering the passive thermal control needs and options, the following recommendations are made to thermally insulate and cool the six coils of the spacecraft:

1. Point the hexagonal end of the spacecraft at the Sun
2. Position the solar arrays in front of the heat shield
3. Size the heat shield to account for 5° pointing accuracy:
    a. Distance from center of hexagon to outside edge = 13.84 m
4. Use a JWST quality heat shield:
    a. Only 0.28 radiates on coils
    b. Surface treatments provide margin, accounting for coil-charging/operating loads
    c. Internal habitat heat must be moved and radiated

Figure 14.6 depicts the block diagram of the passive thermal control process.

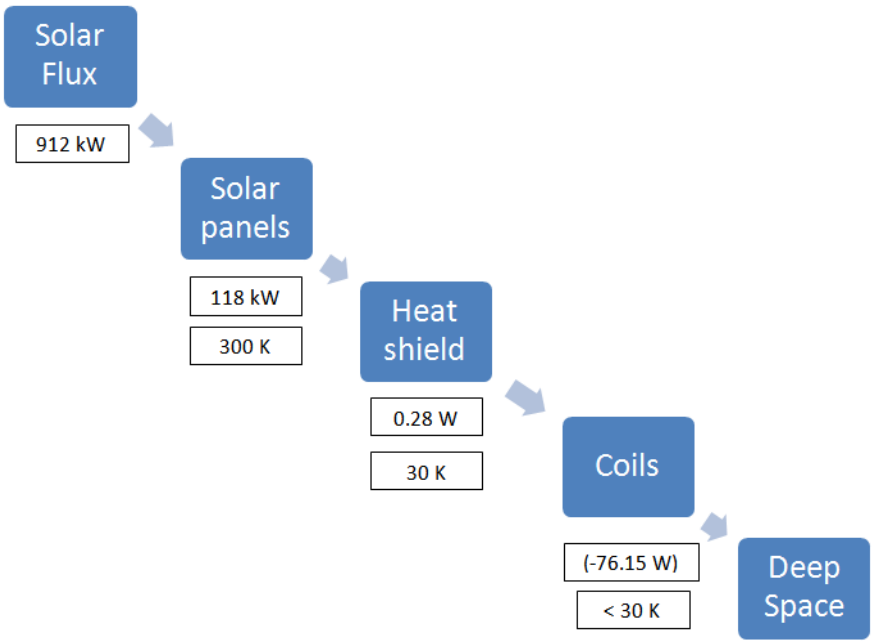

Figure 14.6. Passive thermal control block diagram.

14.4 Active Thermal Control

14.4.1 Cryocoolers

The Phase I study suggested extensive use of cryocoolers to cool the coils. While heat shields are recommended as the primary method for cooling the coils from the external environment, cryocoolers may be used to remove the habitat heat (heat transferred from the habitat to the coils). Additionally, the study deemed it prudent to review the current state of cryocooler technology to provide a comparison and to identify possible future developments necessary for this system.

Cryocoolers are a well-established space technology used on several satellites with various cooling powers that operate temperatures and developed to perform continuously for over 10,000 hours without maintenance.[18] However, despite their extensive use, space-worthy cryocoolers have not been designed with thermal loads or operating temperatures nearing the requirements of the solenoid array. There are several terrestrial and space-based options to use around 70 K, and many below 20 K, but the options are limited for the 20- to 40-K temperature range, as seen in Figure 14.7 and Figure 14.8.[19,20,21]

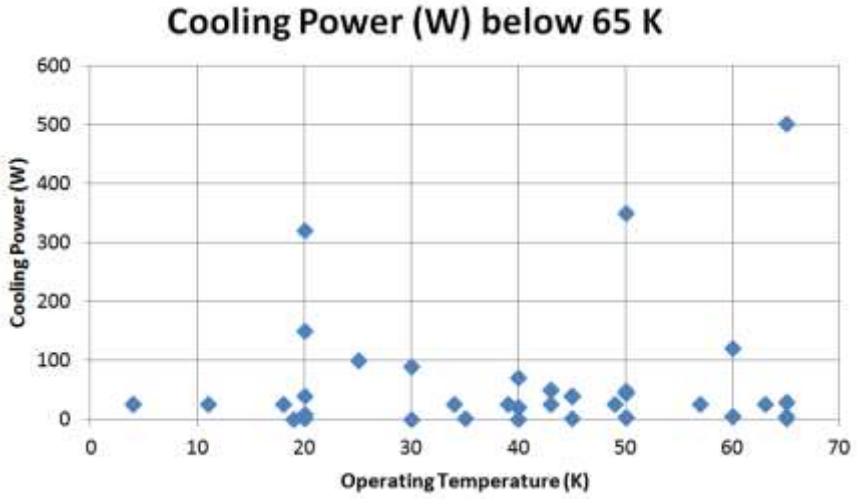

Figure 14.7. Cryocooler power vs. operating temperature below 65 K.

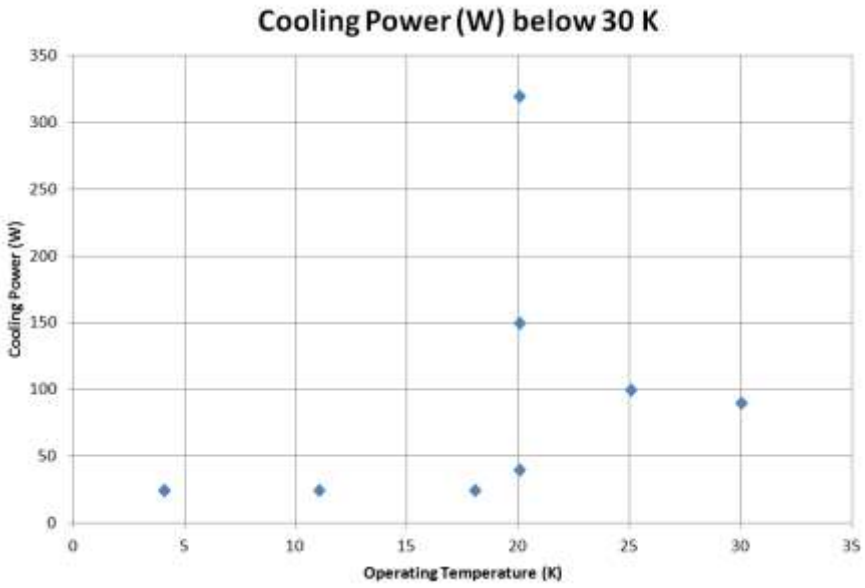

Figure 14.8. Cryocooling power vs. operating temperature below 30 K.

The specifics of the cryocoolers operating below 30 K are reviewed in Table 14.3, and are used to present options for removing the habitat heat.

Table 14.3. Available Cryocoolers and Their Specifications Below 30 K

Product	Operating Temperature (K)	Cooling Power (W)	Input Power (kW)	Mass (kg)
SRDK-305D	40	20	N/A	16
RDK-305D	40	20	N/A	16
RDK-400B	40	70	7.2	16
Stirling SPC-4T	20	320	40	1000
Cryomech AL325	25	100	11.2	470
Stirling GPC-1	30	90	11	600
Stirling GPC-2	20	150	22	600

Table 14.4 shows the available cryocooling options that provide a 20 to 25% cooling power margin. Option 4 appears to be a better choice if mass and power cooling capability are the leading design drivers and constraints. However, all four options require at least 56 kW of input power, and considering the power requirements of the six superconducting coils, it is recommended to not use cryocoolers for this system. The NASA team is currently researching cryocooling technology to increase the cooling load at the 20 to 40 K temperature range, while decreasing the input power requirement. The NASA team recommends updating these findings as this research develops.

Table 14.4. Cryocooler Options to Remove the Habitat Thermal Load of the 6 + 1 Coil Spacecraft

	Option 1	Option 2	Option 3	Option 4
Product	Cryomech AL325	Stirling GPC-1	Stirling GPC-2	Stirling SPC-4T
Working Coolers	5	6	4	2
Redundant Coolers	2	2	1	1
Capability of Design (W)	500	540	600	640
Mass (kg)	3290	4800	3000	3000
Power Input (kW)	56	66	88	80

14.4.2 Heat Pipes

Heat pipes were considered to transfer the habitat heat to deep space. However, upon reviewing the MAARSS requirements and innovative technology, heat pipes were ultimately discarded because of a limited capacity of the technology.

Heat pipes work using a 2-phase fluid, evaporating at the hot end and condensing at the cold end. In theory, it is simple enough to imagine such a system working to move the habitat heat out to a radiator; however, the 20 to 30 K requirement of the system constrains the options. The HTS coils are to be kept cooler than 30 K to avoid quenching.

When choosing a heat-pipe coolant, the temperature of the system must be between the triple point and critical temperature of the fluid. After reviewing the available coolants for spacecraft heat pipes, the only appropriate fluid would be neon, which has triple-point and critical-point temperatures of 24.6 K and 44.5 K, respectively.[18]

NASA is developing neon heat-pipe loops. Currently, the system seems robust in the transient and steady states, operating at temperatures between 28 and 43 K; however, the cooling power proved only to be a maximum 1.5 W for the entire system.[22]

The MAARSS Phase I study deemed that the thermal load imposed on the coils, as a result of the habitat, is 380 W. Therefore, while the neon heat-pipe loop would have several advantages (no moving parts, self-regulating, no external pumping power), the technology has not yet been developed to fulfil the requirements of the MAARSS spacecraft system.

14.4.3 Mechanically Pumped Fluid Loops

Similar to cryocoolers, mechanically pumped fluid loops (MPFL) work by moving cooling fluid throughout a system, distributing the thermal load. Unlike a cryocooler, which cools the fluid through a refrigerating thermodynamic system, an MPFL cools the fluid by radiating the heat into space, as seen in the simplified concept of Figure 14.9.[18]

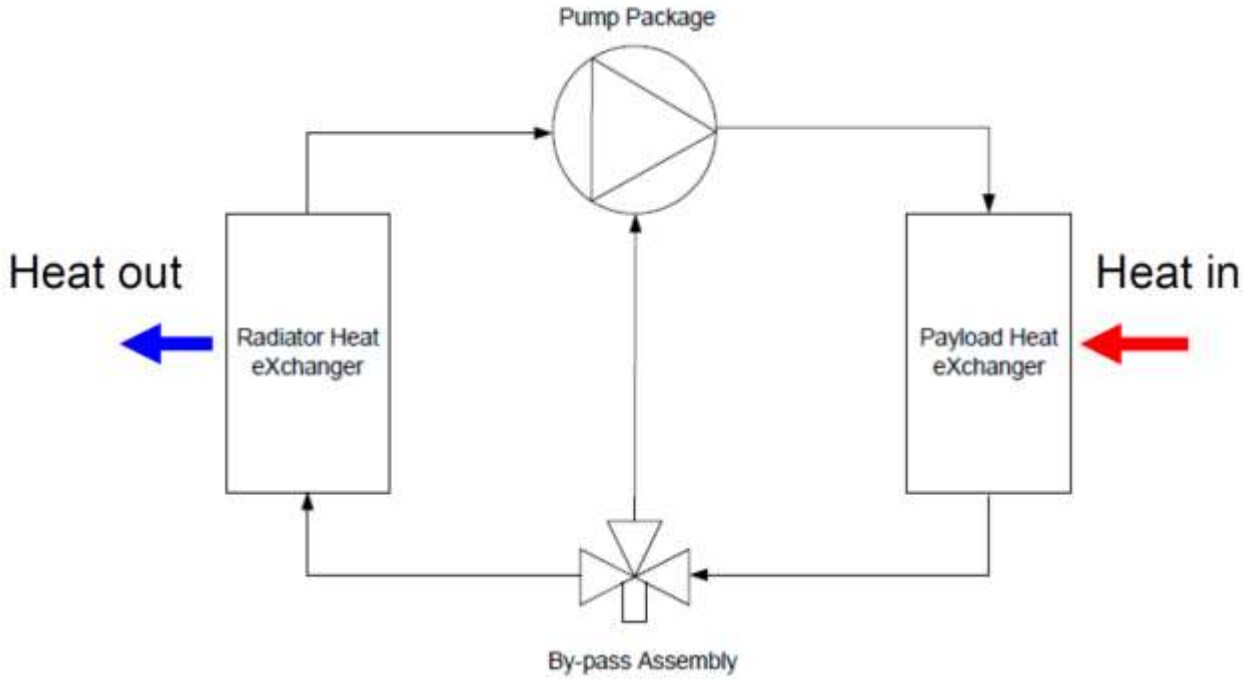

Figure 14.9. Mechanically pumped fluid loop concept.

These fluid loops have extensive spaceflight experience, and have proven capable of great cooling-power capacity. Considering the mission and spacecraft architectures of this experience, the most relevant analog is the Skylab; however, the Mars Exploration Rover (MER) and International Space Station (ISS) systems are also relevant.

The technology behind MPFL is robust and well-proven[23,24]; however, there is little information on the range of design. While this study was able to provide a review of the cryocoolers' market, MPFLs are designed independently for each mission. Therefore, the recommendations are made based on a comparison of the technology used in Table 14.5.

Table 14.5. Mechanically Pumped Fluid Loop Spaceflight Heritage

Space Application	Working Fluid	Fluid Temp. Range, °C	Capacity
Skylab ATM	Methanol/ Water	2 to 8	500 W
NSTS Shuttle	CFC-21	0 to 80	14 kW
NSTS Shuttle	Water	0 to 80	14 kW
ISS	Water	5 to 55	14 kW
ISS	Ammonia	- 70 to 50	14 kW
Mars Pathfinder	CFC-11	-80 to 50	150 W
Mars Exploration Rover	CFC-11	-80 to 50	160 W

The specifications of an MPFL suitable for the missions referenced in Section 12 of this study are as follows:

1. Cooling fluid: ammonia
2. Pumping assembly:
    a. Size: 175 x 127 x 91 cm
    b. Mass: 354 kg, including a 4 kg accumulator
3. Main bus switch unit cold plates:
    a. Size: 94 x 84 x 51 cm
    b. Mass: 50 kg
    c. Cooling power: 495 W
    d. Fluid flow: 80 lbs/hr (0.010 kg/sec)
4. By-pass valve = 10 kg
5. Tubing = 30 k
6. Pressure 300 to 500 psia

Figure 14.10 depicts the block diagram of the active thermal control for the MAARSS spacecraft. The specifications were based primarily on the ISS active thermal control loop, scaled back to accommodate the ~500 W thermal load of the MAARSS system. This design is preliminary, considering that the MPFL design is scalable and well-established. Further work should be done to optimize the design considering such factors as power input, tube diameter, and interfacing with the other habitat systems.

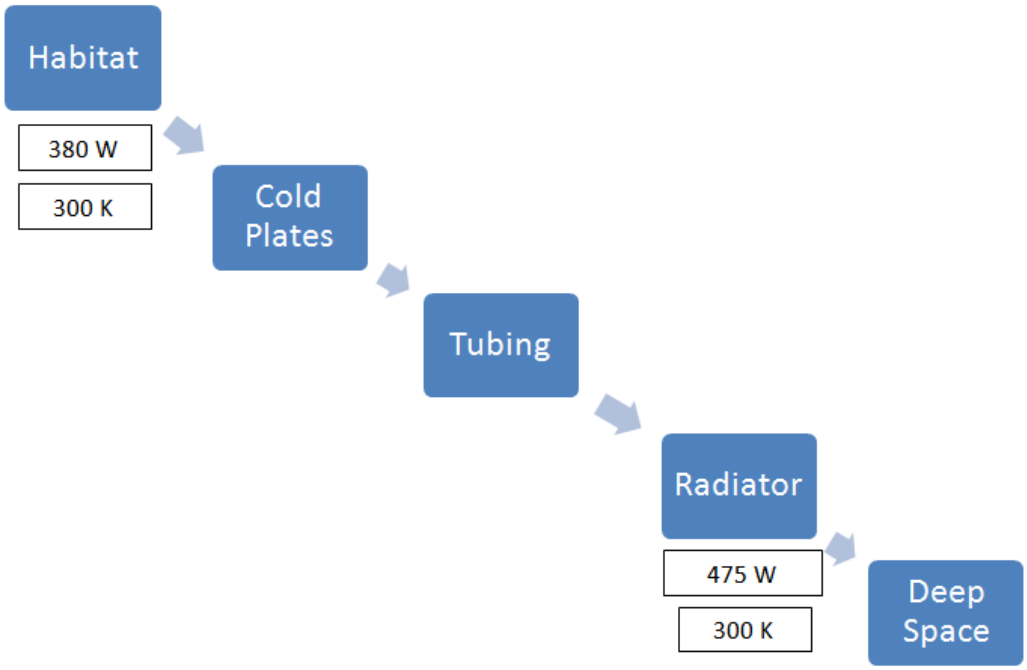

Figure 14.10. Active thermal control block diagram.

14.4.4 Radiator

Spacecraft radiators are also well-established, with an assumed emissivity of 0.9 at beginning of life (BOL).[14] Considering the 475 habitat thermal load (380 W + 25% margin), the relevant equation for sizing the radiator is as follows:

$$A_{radiator} = Q_{rad}/(e * \sigma * T^4)$$

$$= 1.15 \text{ m}^2$$

Q_{rad} = radiating power

$A_{radiator}$ = the area of the radiator required to radiate the external thermal load

T = the radiating temperature, ~300 K.

The radiator should have a greater margin to reduce the heat leak onto the coils. Increasing the thermal load to 500 W, the area becomes 1.21 m^2. This radiator may be incorporated into the assumed active thermal control system of the habitat.

14.5 Final Configuration

The final specifications for the MAARSS thermal design are listed and reviewed below:

1. Passive Thermal Control:
    a. JWST quality heat shield, e* = 0.000001
    b. Area ~ 665 m^2, minimum apothem = 13.84 m
    c. Z93 paint on structural mat, a = 0.17, e = 0.92
2. Active Thermal Control:
    a. MPFL
    b. ISS heritage, high reliability
    c. Mass = 560 kg
    d. Input power < 14 kW
    e. Radiator, A = 1.15 m^2, mass = 15 kg

The thermal control system is depicted by a block diagram (Figure 14.11). The passive thermal control will radiate the internal coil-charging load and all external thermal loads including solar, Earth and Moon infrared, and the back emissivity of the solar panels and heat shield.

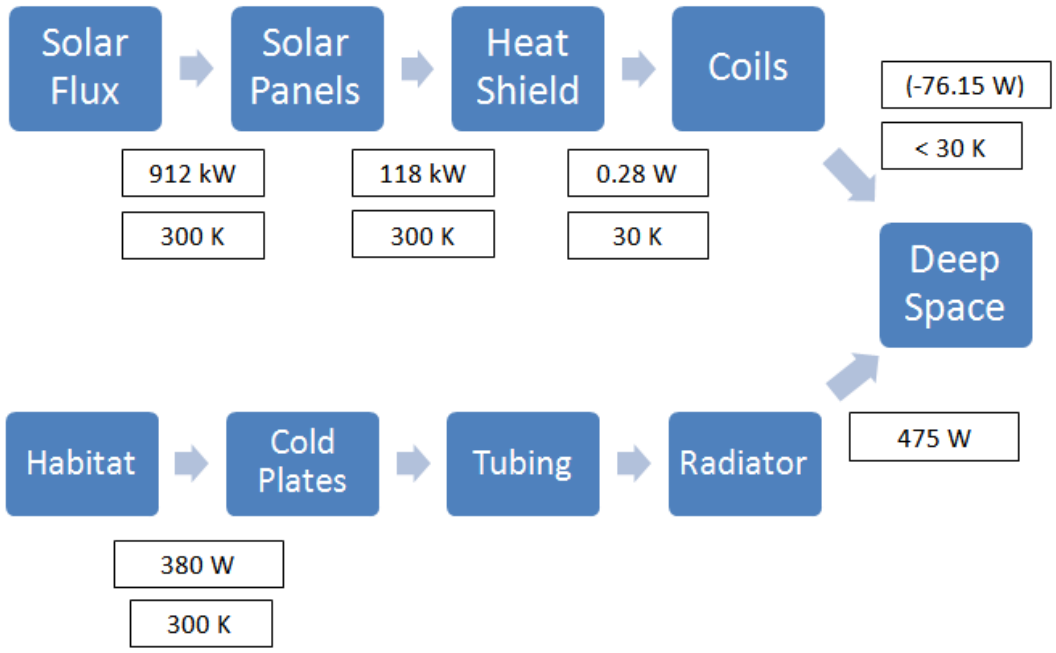

Figure 14.11. MAARSS spacecraft thermal control block diagram.

The active thermal control system will radiate all internal habitat heat away from the spacecraft. The system is modeled after the analogous onboard the ISS and Skylab, and provides a 25% cooling margin to ensure that the coils are insulated and remain below 30 K.

The MAARSS spacecraft would be the most advanced human spacecraft ever developed. The technologies behind the fabrication, launch, deployment, and radiation shielding of the HTS coils still need to be designed and developed. The thermal requirements lie outside of the traditional trade space of spacecraft thermal design and cryocooling capability.

The design process behind this spacecraft thermal control design was to use space-worthy technologies as well as those currently under development. Although heat shields have been used on many spacecraft, only the JWST sunshield compares to the MAARSS requirements in size and cooling power. As such, it is reasonable to assume that this technology will be validated and continue to improve after the JWST launch. Cryocooling technology does not seem efficient at 20 to 30 K operating temperatures. Options were considered and presented, but ultimately discounted in favor of more space-proven technologies.

There are limitations to the configuration seen in this study, most notably in the heat shield. The heat shield was designed assuming that it would be possible to keep the tail end of the spacecraft pointed at the Sun; however, this may not always be possible. Considering the likely orbital trajectory of the spacecraft's mission, (with destinations such as the Moon, Mars, or NEAs), keeping the tail end pointed at the Sun for the entirety of the mission may be impossible. Although it is severely limiting, the heat shield provides extensive cooling and should be considered for future use because its deployment would reduce the power input, and possibly the mass, required of the thermal control system on the MAARSS spacecraft.

14.6 Additional Considerations

Structure between the habitat and the compensation coil is needed to maintain the spacing between them. This structure will provide an unavoidable heat-leak path. The degree of leakage through this path depends on the details of the structure and has not been determined in this study. Since the temperature along the structure will vary from 300 K at the habitat end to about 30 K at the coil end, and the conducted heat flow is roughly proportional to the temperature difference, it may be worthwhile to implement an actively cooled structural element by cooling an intermediate point along the structure. This is standard practice for ground cryogenic equipment.

15 Trade Studies: System Analysis and Technology Work

See Appendix E for the associated code.

As part of this study, the team surveyed the major systems required for this type of solenoidal, confined magnetic field design. Basic mass calculations were developed for each system and were used to determine the resulting radiation exposure for a generic solenoid design. Using a range of magnetic field strength and thickness values allowed some of the basic characteristics of such a design to be observed. Additionally, this allowed the team to identify key technologies for future development. A brief summary of the major results is presented here, and a full discussion of these results are in the paper *Active Magnetic Radiation Shielding System Analysis and Key Technologies*.[25] The code used to conduct this analysis is contained in Appendix E.

15.1 System Trade Space Analysis

Based on the systems analysis and mass relationships derived in Washburn et al.,[25] a solenoidal active magnetic shielding design is analyzed over the primary trade space variables of magnetic field strength and magnetic field thickness.[25] The dose equivalent is determined using the methodology outlined by the Analytical-HZETRN model given by Washburn et al.[26] Figure 15.1 shows the general geometry and configuration for this analysis. First, the flux in the barrel region, the region affected by the magnetic field, is determined to be a function of magnetic field strength and thickness. Then, using the system mass estimates discussed in Washburn et al. (to be published), the shield system mass for each material type is determined as a function of the magnetic field strength and thickness. This mass is smeared over a cylinder, selected at the center of the magnetic field as shown in Figure 15.1. This provides the average thickness of the various shielding materials that the flux in the barrel region flux will pass through. The barrel region flux is then transported using HZETRN 2010, through these average thickness values.[27,28,29] The resulting flux output is then transported again through the habitat and the resulting dose equivalent is combined with the habitat endcap region dose equivalent contribution. Because the endcap region flux is unaffected by the magnetic field, the endcap dose equivalent contribution may be calculated separately. The dose equivalent is calculated at the worst-case location inside the habitat (i.e., along the axial centerline, at the edge of the habitat's endcap wall).[26]

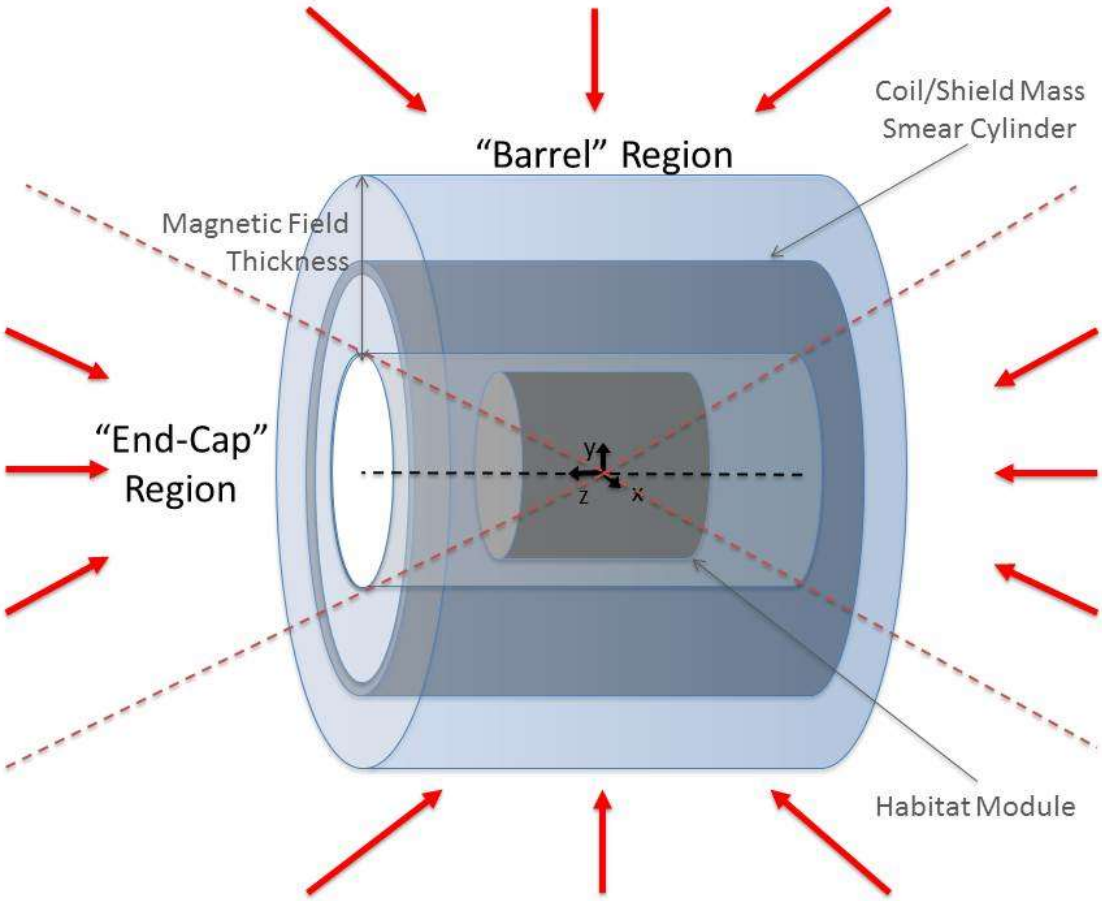

Figure 15.1. Geometry and mass locations.

The following major assumptions are made for this analysis:

1. Superconductor system – HTS:
    a. Material: YBCO tape
    b. Dimensions: 5 cm wide, 0.1 mm thick
    c. J_e: 87 kA/cm^2, assuming 29 kA/cm^2 at 77 K and self-field, with an average of 3x capability for operation at 40 K (Hazelton, 2012)[30]
2. Structural system – Mixed material:
    a. Radial structural material: Kevlar 49
    b. Axial structure material: TorayCA M55J fiber with HexPly 954-6 cyanate epoxy resin (60% fiber by volume)
    c. Coil-to-Coil structural material: TorayCA M55J fiber with HexPly 954-6 cyanate epoxy resin (60% fiber by volume)
    d. C_S: 0.5
    e. F_S: 2.0
3. Thermal system: Cryocirculator type:
    a. Additional system mass: circulator fans, heat exchangers, and piping are accounted for by adding 3x the cryocooler mass
    b. Material: Aluminum 6061

    c. The radiators mass is not included in the barrel region mass since these will likely be located farther away, near the endcaps
4. Power system – Flux pump and solar arrays:
    a. Flux pump material: YBCO tape
    b. The solar array radiators mass is not included in the barrel region mass since these will likely be located farther away, near the endcaps
5. Shield dimensions:
    a. r_i = 4 m
    b. l = 20 m
6. Habitat dimensions:
    a. r_H = 3 m
    b. l_{hab} = 10 m
    c. Cylinder wall thickness: 13.0 g/cm^2 Aluminum 6061, 1.36 g/cm^2 water
    d. Cylinder endcap thickness: 25.0 g/cm^2 Aluminum 6061, 1.36 g/cm^2 water

15.2 Mass and Dose Equivalent Results

Figure 15.2 shows the exposure analysis results for the system and habitat described. This plot also shows the total active magnetic shielding system mass, which is the sum of the superconductor, structural, thermal, and power systems masses, less radiator and solar array mass. It is assumed that the required radiators and solar arrays will be integrated into the larger thermal and power systems of the overall vehicle architecture; therefore, their mass is not included in this total. The mass is given in metric tons, and the color scale also shows this value for the number of Space Launch System (SLS) launches required to place this mass in LEO. This assumes a maximum SLS capability to LEO of 70 t per launch for the Block I model and 130 t per launch for the Block II.

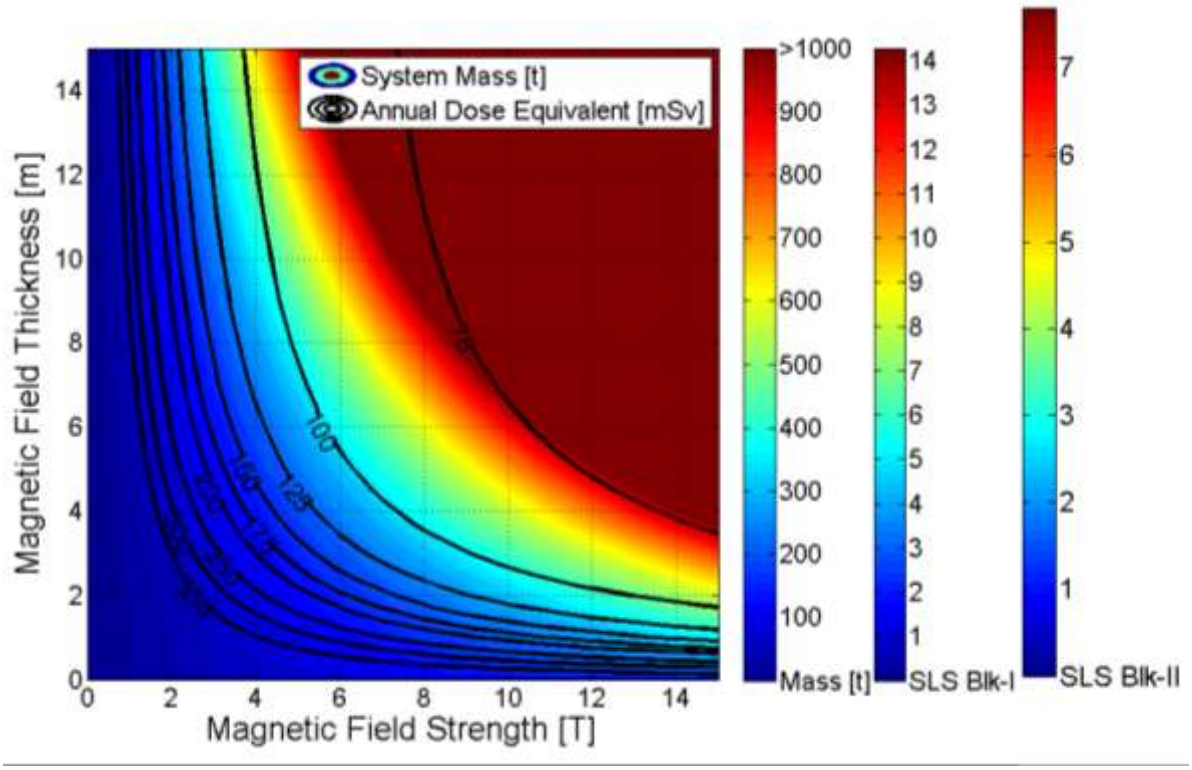

Figure 15.2. Annual dose equivalent and active shielding mass in tons.
Less radiator and solar array mass) and number of SLS Block I and II launches required.

Figure 15.2 demonstrates that a higher field strength is more effective at reducing dose equivalent than a larger field thickness (e.g., 10 T x 2 m yields ~150 mSv/yr, 2 T x 10 m yields ~200 mSv/yr). However, this does not result in the lowest system mass. Figure 15.2 shows that for this specific configuration, a low field strength, medium field thickness; or medium field strength, medium field thickness design, results in the lowest system mass, depending on the exposure value desired. For example, consider a design for a one-year mission, with a point dose equivalent value of 150 mSv as an acceptable exposure design baseline and no other restrictions other than minimizing system mass. Based on these criteria, according to Figure 15.2, the optimal selection is approximately a 4 T, 4.75 m design, resulting in a system mass of approximately 200 t. This translates into the launch capacity of approximately 3 SLS Block I or 1.75 Block II launches to place this system mass in LEO. However, this figure considers only launch mass and does not account for volumetric constraints because of fairing size. Table 15.1 shows the masses for each system for a 1 T x 10 m case, using the above parameters to provide a relative mass comparison.

Table 15.1. System Masses for a 1T x 10m Example Case

System	Mass [t]
Superconductor	34.5
Structural: Radial	6.0
Structural: Axial	6.9
Structural: Coil-to-Coil	2.0
Thermal (less radiators)	4.6
Power (less solar arrays)	0.2
Radiator	5.9
Solar Array	0.9

15.3 Structural and Superconductor Performance Improvements

The structural and superconductor systems are the large mass drivers of the overall shielding system design, and performance improvements in both of these areas have been identified as key enabling technologies to develop an active magnetic shielding design: improved strength/mass ratio, both tensile and compression, for structural materials; and improved current capacity/mass ratio for superconductor materials. Figure 15.3 identifies what levels of improvement are necessary to reduce the overall system launch mass to desirable values. This is examined by first constraining the system to meet two potential objectives: the magnetic field thickness is held at 2 m, which may be necessary to meet launch vehicle fairing requirements; and the system's shielding effectiveness must allow no more than 150 mSv/year for the crew. The above analysis is then conducted to determine the total system mass, which achieves these goals for increasing structure and superconductor performances.

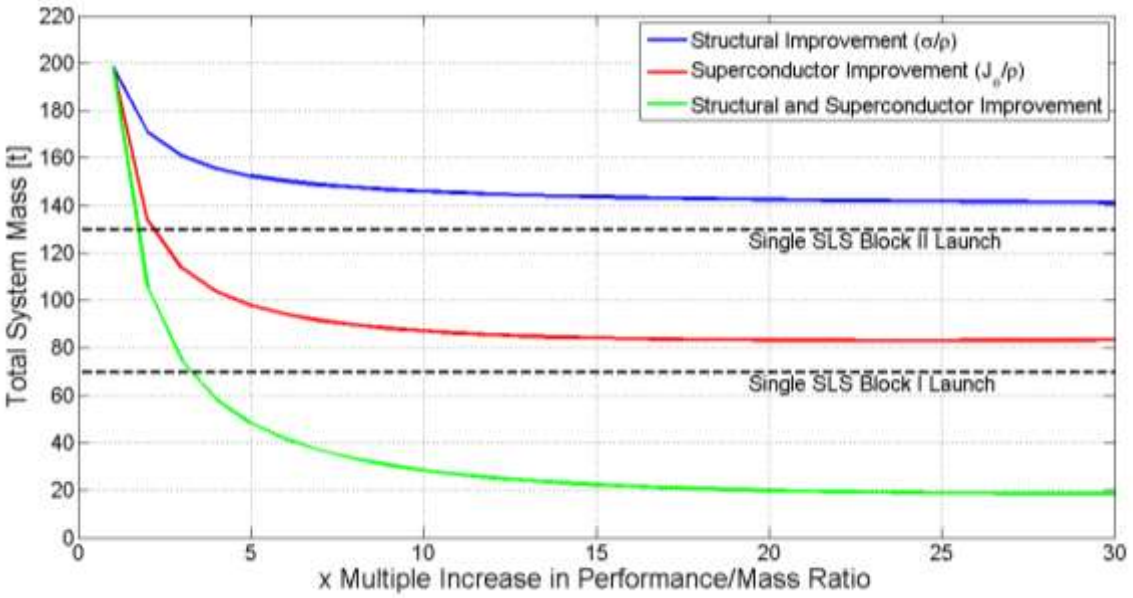

Figure 15.3. Structural and superconductor performance improvements effects on system mass for 2m field thickness and 150 mSv exposure limit design.

As structural material performance is improved, it approaches an asymptotic limit above a 15x performance improvement. Above this, system mass is primarily driven by the superconductor system. Similarly, as superconductor material performance is improved, it also approaches an asymptotic limit above a 15x performance improvement, where system mass is primarily driven by the structural system. If both of these systems are improved equally, the system mass limit is driven by the thermal and power system. As shown in Figure 15.3, performance improvements of 4x are necessary for both the structural and superconductor systems to achieve a total mass low enough to accommodate a single SLS Block I launch, and 2x for a single Block II launch.

15.4 Key Technologies

The NASA and AML teams used these systems' survey to identify the key enabling and enhancing technologies, listed below. Enabling technologies are required to facilitate the design based on providing substantial mass reductions to the overall system or low Technology Readiness Level (TRL) technologies that are essential to operate the system. Enhancing technologies are those that would significantly improve the performance of a system or reduce the design requirements of an associated system.

Enabling Technologies:

1. **Superconductor:** Improvements in the critical and engineering current density of superconductor material (metallurgical and manufacturing improvements to increase the critical current density of existing superconductor material or development of new higher performance superconductors).
2. **Structures:** Development of higher-strength, lighter-weight structural materials.
3. **Thermal:** Development of space-qualified, high-capacity cryocoolers and heat shield technology
4. **Power:** Development of high-current, transformer rectifier HTS flux pumps.

Enhancing Technologies:

1. **Superconductor:** Manufacturing improvements to increase the maximum achievable length of superconductor wires and tapes.
2. **Superconductor:** Development of improved superconductor splice technology.
3. **Superconductor:** Development of new, higher-temperature superconductors.
4. **Thermal:** Improvements in cryocooler efficiency.

16 Conclusion

Using magnetic fields generated by high temperature superconducting coils to shield from radiation during long duration missions is possible. The configuration studied here does not offer dramatic improvements over passive shielding and further development of enabling technologies such as superconductor current densities and lighter weight structural materials are needed to allow configurations that would offer significant improvements over passive shielding.

17 References

1. Committee on the Evaluation of Radiation Shielding for Space Exploration, National Research Council, *Managing Space Radiation Risk in the New Era of Space Exploration*. Dulles, VA: National Academies Press, 2008.

2. von Braun, W., "Will Mighty Magnets Protect Voyagers to Planets?" *Popular Science Monthly*, pp. 98-100, Jan. 1969.

3. Kervendal, E. et al., "Spacecraft Radiation Shielding Using Ultra Lightweight Superconducting Magnets", *44th AIAA Aerospace Science Meeting*, Reno, Nevada, 2006.

4. Battiston, R. et al., "An Active Radiation Screen Design Based on Superconducting Double-helix Solenoids," *5th IAASS Conference*, Versailles-Paris, France, 2011.

5. NIAC Grant, "Radiation Protection and Architecture Utilizing High Temperature Superconducting Magnets."

6. CoilCAD. (n.d.). Retrieved from Magnetlab: http://www.magnetlab.com/technology/design/coilcad/

7. Cook, R. et al., *Concepts of Applications of Finite Element Analysis*. Wiley, 2002

8. *CryoComp* Ver. 5.2 database. Retrieved from CryoComp Rapid Cryogenic Design: http://www.eckelsengineering.com.

9. Larsson, J., "Electromagnetics from a quasistatic perspective," *American Journal of Physics*, Vol. 75, pp. 230-239, Mar. 2007.

10. Lee, H. et al., "Superconducting Joint of 2G ReBCO Coated Conductors," *23rd International Conference on Magnet Technology*, Boston, MA, 2013.

11. Osamura, K. et al., "Internal Strain and Mechanical Properties at Low Temperatures of Surround Cu Stabilized YBCO Coated Conductor," *IEEE Transactions on Applied Superconductivity*, Vol. 20, No. 3, pp. 1532-1536, June 2010.

12. Rapp, D., "Radiation Effects and Shielding Requirements in Human Missions to the Moon and Mars," MARS, Vol. 2, pp. 46-71, 2006. doi:10.1555/mars.2006.0004.

13. Westover, S. C. et al., "Magnet Architectures and Active Radiation Shielding Study," 2012. Available: http://www.nasa.gov/pdf/718392main_Westover_2011_PhI_MAARSS.pdf.

14. Gilmore, D. G. (ed.), *Spacecraft Thermal Control Handbook, Volume 1: Fundamental Technologies*, 2nd ed., AIAA/Aerospace Press: El Segundo, CA, 2002, p. 837 .

15. "Earth's Thermal Environment," *Thermal Environments, JPL D-8160*, 2008. Available: http://www.tak2000.com/data/planets/earth.htm

16. Wertz, J. R. and Larson, W. (ed.), *Space Mission Analysis and Design*, 3rd ed., Springer New York: New York, NY, 1993, p. 988.

17. GSFC, (2014, Aug. 12), *Explore James Webb Space Telescope: The Sunshield*, Available: http://jwst.nasa.gov/sunshield.html

18. Donabedian, M. (ed.), *Spacecraft Thermal Control Handbook, Volume 2: Cryogenics*, AIAA/Aerospace Press: El Segundo, CA, 2003.

19. Bi, Y. F., "Cooling and Cryocoolers for HTS Power Applications," *Applied Superconductivity and Electromagnetics*, Vol. 4, No. 1, pp. 97–108, Nov. 2013.

20. Radebaugh, R., "Cryocoolers: the State of the Art and Recent Developments," *Journal of Physics: Condensed Matter,* Vol. 21, No. 16, 2009. doi:10.1088/0953-8984/21/16/164219.

21. Ross, R. G., and Boyle, R. F., "An Overview of NASA Space Cryocooler Programs—2006," *Cryocoolers 14*, ICC Press: Boulder, CO, 2007, pp. 1–10.

22. Ku, J., and Robinson, F., "Testing of a Neon Loop Heat Pipe for Large Area Cryocooling," *Spacecraft Thermal Control Workshop,* El Segundo, CA, 2014.

23. van Benthem, R. C. et al., "Development of a Mechanically Pumped Fluid Loop for 3 to 6 kW Payload Cooling," March 2010 Report NLR-TP-2009-459

24. Paris, A. D., Bhandari, P., and Birur, G. C., "High Temperature Mechanically Pumped Fluid Loop for Space Applications," SAE Technical Paper 2004-01-2415, p. 7, 2004. doi:10.4271/2004-01-2415.

25. Washburn, S. A., et al., "Active Magnetic Radiation Shielding System Analysis and Key Technologies," unpublished.

26. Washburn, S. A., et al., "Analytical-HZETRN Model for Rapid Assessment of Active Magnetic Radiation Shielding," *Advances in Space Research*, Vol. 53, Issue 1, pp. 8-17, Jan. 2014.

27. Wilson, J. W., et al., "HZETRN: Description of a Free-Space Ion and Nucleon Transport and Shielding Computer Program," NASA Technical Paper 3495, May 1995.

28. Slaba, T. C., Blattnig, S. R., and Badavi, F. F., "Faster and More Accurate Transport Procedures for HZETRN," *Journal of Computational Physics*, Vol. 229, Issue 24, pp. 9397-9417, Dec. 2010.

29. Slaba, T. C. et al, "Coupled Neutron Transport for HZETRN," *Radiation Measurements*, Vol. 45, Issue 2, pp. 173-182, Feb. 2010.

30. Hazelton, D. W.: 2G HTS Conductors at SuperPower. In Low Temperature High Field Superconductor Workshop, Napa : SuperPower, 2012